

AFIT/GAP/ENP/95-11

STEADY-STATE KINETICS  
OF  $\text{Br}(^2\text{P}_{1/2}) \rightarrow \text{CO}_2(101)$   
ELECTRONIC-TO-VIBRATIONAL  
ENERGY TRANSFER LASER SYSTEM  
THESIS

Stephen J. Karis  
Captain, USAF

AFIT/GAP/ENP/95-11

19960402 156

Approved for public release; distribution unlimited

**STEADY-STATE KINETICS  
OF  $\text{Br}(^2\text{P}_{1/2}) \rightarrow \text{CO}_2(101)$   
ELECTRONIC-TO-VIBRATIONAL  
ENERGY TRANSFER LASER SYSTEM**

THESIS

Presented to the Faculty of the School of Engineering  
of the Air Force Institute of Technology

Air University

In Partial Fulfillment of the  
Requirements for the Degree of  
Master of Science in Applied Physics

Stephen J. Karis, A.S., B.A.

Captain, USAF

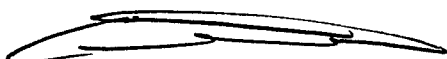
November 1995

Approved for public release; distribution unlimited

**STEADY-STATE KINETICS  
OF  $\text{Br}(^2\text{P}_{1/2}) \rightarrow \text{CO}_2(101)$   
ELECTRONIC-TO-VIBRATIONAL  
ENERGY TRANSFER LASER SYSTEM**

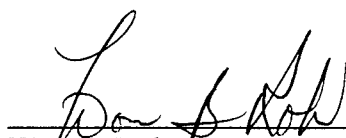
Stephen J. Karis, A.S., B.A.  
Captain, USAF

Approved:



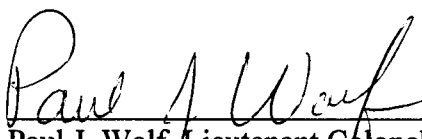
Glen P. Perram, Major, USAF  
Chairman, Advisory Committee

20 NOV 95



Won B. Roh  
Member, Advisory Committee

20 Nov 95



Paul J. Wolf, Lieutenant Colonel, USAF  
Member, Advisory Committee

20 NOV 95

## *Preface*

This research constitutes the latest installment in an ongoing project at AFIT to develop and characterize the technology of photolytically-pumped molecular lasers. In the process of conducting this work, many doors were opened. While the majority of these doors still remain open, it is nevertheless hoped that the findings reported here represent a useful contribution to the body of knowledge on bromine/carbon dioxide laser systems, and will be of some practical value to future workers. My own efforts in this pursuit were aided immeasurably by the previous work of Captains Ralph Tate, Steven Katapski, and Ray Johnson, and First Lieutenant Michael Hawks.

The impact of the many frustrations I encountered along the way was softened by the ultimate realization of the lessons in experimental physics they represented. The overall lesson of this research was perhaps the most valuable: Knowledge often arrives from unexpected directions.

I would like to sincerely thank my advisor, Major Glen Perram, for his incredible patience, willingness to repeat himself, and generosity with time he really couldn't spare. Through him I have been introduced to a new and interesting field of study, chemical physics, one which would not have captured my attention 18 months ago. I must also commend Major Perram on his magical (and embarrassing) ability to find "missing" equipment in places I had already checked twice.

Next I offer thanks to Captain Ray Johnson, Professor Won Roh, and Lieutenant Colonel Paul Wolf for their advice and assistance along the way. Their help with setting up the experimental apparatus, keeping it healthy, and interpreting its performance are much appreciated.

Of course no experiment would have been possible without the dedication of the AFIT research support team. AFIT Physics Technicians Jim Reynolds and Gregg Smith and Wright Laboratory Glassware Technician Mike Ray provided the equipment and

technical expertise necessary to create the appropriate, impressive clutter on my laboratory workbench. No serious experimental research can be conducted without lights, bells, whistles, and the machine that goes "ping."

Finally, I offer my most heartfelt thanks to my wife, Cori, and our daughters Elena and Hayley. Throughout the program they have been pillars of support and compassion, and it is to them I dedicate this document, for it represents their toil and sacrifice as much as my own. I look forward to getting to know them again.

Stephen J. Karis

## Table of Contents

Preface.....	iii
List of Figures .....	viii
List of Tables .....	x
List of Symbols.....	xi
Abstract.....	xiv
I. Introduction .....	1-1
A. Background .....	1-1
B. Current Knowledge .....	1-4
1. Br* Quenching by E→V Transfer .....	1-4
2. E→V Pumped Lasers.....	1-7
C. Problem Statement .....	1-8
D. Scope.....	1-8
E. Approach .....	1-9
F. Summary.....	1-10
II. Theory .....	2-1
A. Spectroscopic Theory.....	2-1
1. Atomic Spectroscopy .....	2-1
2. Molecular Spectroscopy.....	2-3
B. Bromine and Photolysis .....	2-7
1. Atomic Bromine.....	2-7
2. Molecular Bromine .....	2-8

3. Absorption and Photolysis .....	2-10
C. Carbon Dioxide and E→V Transfer.....	2-12
D. Gas Kinetics .....	2-13
1. Deactivation Mechanisms .....	2-13
2. Production and Quenching of Br* .....	2-16
3. Production and Quenching of CO <sub>2</sub> <sup>†</sup> .....	2-19
III. Experiment.....	3-1
A. Experimental Apparatus.....	3-1
1. Laser Cavity .....	3-1
2. Gas-Handling .....	3-3
3. Photolysis.....	3-4
4. Detection .....	3-4
5. Data Collection and Reduction .....	3-8
B. Experimental Procedures.....	3-10
1. Br <sub>2</sub> Sample Preparation.....	3-10
2. 488 nm Absorption .....	3-11
3. CO <sub>2</sub> Quenching of Br* .....	3-12
4. CO <sub>2</sub> Quenching of CO <sub>2</sub> <sup>†</sup> .....	3-12
5. Steady-State Signal Decay .....	3-13
6. Chopping Frequency Dependence .....	3-14
IV. Results and Analysis.....	4-1
A. 488 nm Absorption.....	4-1

1. Absorption Cross Section .....	4-1
2. Br <sub>2</sub> Concentration.....	4-4
B. CO <sub>2</sub> Quenching of Br* .....	4-6
C. CO <sub>2</sub> Quenching of CO <sub>2</sub> <sup>†</sup> .....	4-10
D. Steady-State Signal Decay .....	4-17
1. Time-Decay Observations.....	4-17
2. Mixing.....	4-19
3. Br <sub>2</sub> Concentration.....	4-21
4. Br* Quenching .....	4-24
5. CO <sub>2</sub> Loss .....	4-25
6. CO <sub>2</sub> <sup>†</sup> Quenching.....	4-26
E. Chopping Frequency Dependence .....	4-26
V. Conclusions and Recommendations .....	5-1
A. 488 nm Absorption.....	5-1
B. CO <sub>2</sub> Quenching of Br* .....	5-2
C. CO <sub>2</sub> Quenching of CO <sub>2</sub> <sup>†</sup> .....	5-2
D. Steady-State Signal Decay .....	5-4
E. Chopping Frequency Dependence.....	5-5
F. Other Recommendations .....	5-7
G. Summary .....	5-8
Bibliography .....	a
Vita.....	d



## *List of Figures*

Figure 1-1. Proposed experimental apparatus.....	1-10
Figure 2-1. Energy level diagram for atomic bromine.....	2-8
Figure 2-2. Potential energy diagram for molecular bromine.....	2-9
Figure 2-3. Decadic absorption coefficient for molecular bromine.....	2-11
Figure 2-4. Energy level diagram for carbon dioxide.....	2-13
Figure 3-1. Diagram of experimental apparatus .....	3-2
Figure 3-2. Plot of transmittance vs. wavelength for 2.71 $\mu\text{m}$ IR band pass filter .....	3-6
Figure 3-3. Plot of transmittance vs. wavelength for 4.32 $\mu\text{m}$ IR bandpass filter .....	3-7
Figure 4-1. Graph of normalized 488 nm transmittance vs. $\text{Br}_2$ pressure.....	4-1
Figure 4-2. Graph of $-\ln(I/I_0)$ vs. $\text{Br}_2$ pressure .....	4-3
Figure 4-3. Graph of normalized 2.7 $\mu\text{m}$ emission intensity vs. $\text{CO}_2$ pressure. ....	4-7
Figure 4-4. Graph of $I_0/I$ showing large excursions due to noise in I .....	4-7
Figure 4-5. Graph of normalized 2.7 $\mu\text{m}$ emission intensity showing best fit .....	4-9
Figure 4-6. Graph of normalized 4.3 $\mu\text{m}$ emission intensity vs. $\text{CO}_2$ pressure .....	4-11
Figure 4-7. Graph of normalized 4.3 $\mu\text{m}$ emission intensity vs. $[\text{CO}_2]/[\text{Br}_2]$ .....	4-11
Figure 4-8. Evaluation of kinetic model for $\text{CO}_2$ quenching of $\text{CO}_2^\dagger$ .....	4-13
Figure 4-9. Evaluation of revised kinetic model for $\text{CO}_2$ quenching of $\text{CO}_2^\dagger$ .....	4-16
Figure 4-10. 4.3 $\mu\text{m}$ signal vs. time showing signal decay.....	4-18
Figure 4-11. $\text{CO}_2$ pressure and 4.3 $\mu\text{m}$ signal vs. time showing mixing lag .....	4-19
Figure 4-12. 4.3 $\mu\text{m}$ signal vs. time for small $\text{CO}_2$ concentrations.....	4-20

Figure 4-13. 4.3 $\mu\text{m}$ signal vs. time for various delays before photolysis.....	4-21
Figure 4-14. Total cell pressure and Si detector signal vs. time: delay profile.....	4-23
Figure 4-15. 4.3 $\mu\text{m}$ signal and cell pressure vs. time: on-off-on profile. ....	4-24
Figure 4-16. 2.7 $\mu\text{m}$ emission intensity vs. time with and without added $\text{CO}_2$ . ....	4-25
Figure 4-17. 4.3 $\mu\text{m}$ signal vs. chopping frequency .....	4-28
Figure 4-18. Detector signal vs. chopping frequency for white light source.....	4-28

*List of Tables*

Table 4-1. Br <sub>2</sub> Absorption Cross Section at 488 nm.....	4-3
Table 4-2. Results of Collision-Free Rate Coefficient (k <sub>0</sub> ) Experiment. ....	4-9

## *List of Symbols*

$+/-$	= symmetric/antisymmetric reflection symmetry
A, B	= atomic or molecular species
[A]	= concentration of A [molec cm <sup>-3</sup> ]
A*	= electronically excited species
B <sup>†</sup>	= vibrationally excited species
Br	= ground state bromine atom, Br( <sup>2</sup> P <sub>3/2</sub> )
Br*	= electronically excited bromine atom, Br( <sup>2</sup> P <sub>1/2</sub> )
Br <sub>2</sub>	= bromine molecule
CO <sub>2</sub>	= ground state carbon dioxide molecule, CO <sub>2</sub> (000)
CO <sub>2</sub> <sup>†</sup>	= vibrationally excited carbon dioxide molecule, CO <sub>2</sub> (101)
CO <sub>2</sub> <sup>°</sup>	= vibrationally excited carbon dioxide molecule, CO <sub>2</sub> (not 101)
E→V	= electronic-to-vibrational energy transfer
E <sub>elec</sub>	= electronic energy [J, eV, cm <sup>-1</sup> ]
E <sub>rot</sub>	= rotational energy [J, eV, cm <sup>-1</sup> ]
E <sub>tot</sub>	= total energy (E <sub>elec</sub> + E <sub>vib</sub> + E <sub>rot</sub> ) [J, eV, cm <sup>-1</sup> ]
E <sub>vib</sub>	= vibrational energy [J, eV, cm <sup>-1</sup> ]
ΔE <sub>elec</sub>	= quantum of electronic energy [J, eV, cm <sup>-1</sup> ]
ΔE <sub>vib</sub>	= quantum of vibrational energy [J, eV, cm <sup>-1</sup> ]
ΔE <sub>rot</sub>	= quantum of rotational energy [J, eV, cm <sup>-1</sup> ]
g/u	= even/odd inversion symmetry
hν	= quantum of photon energy [J, eV, cm <sup>-1</sup> ]
I	= transmitted/incident laser intensity ratio, I <sub>t</sub> /I <sub>i</sub>
I <sub>0</sub>	= baseline (empty-cell) transmitted/incident laser intensity ratio, (I <sub>t</sub> /I <sub>i</sub> ) <sub>0</sub>
I <sub>2.71</sub>	= 2.71 μm side-fluorescence intensity [W cm <sup>-2</sup> ]
I <sub>2.71</sub> <sup>0</sup>	= 2.71 μm side-fluorescence intensity for [CO <sub>2</sub> ] = 0
I <sub>i</sub>	= incident pump laser intensity [W cm <sup>-2</sup> ]
I <sub>p</sub>	= internal (within medium) pump laser intensity [W cm <sup>-2</sup> ]
I <sub>t</sub>	= transmitted pump laser intensity [W cm <sup>-2</sup> ]
J	= total angular momentum quantum number
<b>J</b>	= total angular momentum vector
k <sub>0</sub>	= collision-free deactivation rate coefficient for Br* [sec <sup>-1</sup> ]
k <sub>0</sub> '	= collision-free deactivation rate coefficient for CO <sub>2</sub> <sup>†</sup> [sec <sup>-1</sup> ]

$k_{2.71}$	= radiative decay rate coefficient for $\text{Br}^*$ [ $\text{sec}^{-1}$ ]
$k_{3B}$	= three-body recombination rate coefficient for $\text{Br}_2$ [ $\text{cm}^6 \text{ molec}^{-2} \text{ sec}^{-1}$ ]
$k_{4.3}$	= radiative decay rate coefficient for $\text{CO}_2^\dagger$ [ $\text{sec}^{-1}$ ]
$k_{\text{Br}_2}$	= self-quenching rate coefficient for bromine [ $\text{cm}^3 \text{ molec}^{-1} \text{ sec}^{-1}$ ]
$k_{\text{CO}_2}$	= self-quenching rate coefficient for carbon dioxide [ $\text{cm}^3 \text{ molec}^{-1} \text{ sec}^{-1}$ ]
$k_{\text{diff}}$	= diffusion rate coefficient [ $\text{sec}^{-1}$ ]
$k_{\text{EV}}$	= quenching rate coefficient for $\text{Br}^* \rightarrow \text{CO}_2(101)$ [ $\text{cm}^3 \text{ molec}^{-1} \text{ sec}^{-1}$ ]
$k_{\text{obs}}$	= observed wall deactivation rate coefficient [ $\text{sec}^{-1}$ ]
$k_{\text{other}}$	= quenching rate coefficient for $\text{Br}^* \rightarrow \text{CO}_2(\text{not } 101)$ [ $\text{cm}^3 \text{ molec}^{-1} \text{ sec}^{-1}$ ]
$k_p$	= pump rate coefficient [ $\text{cm}^2 \text{ watt}^{-1} \text{ sec}^{-1}$ ]
$k_{\text{QB}}$	= quenching rate coefficient for $\text{CO}_2^\dagger$ by $\text{Br}_2$ [ $\text{cm}^3 \text{ molec}^{-1} \text{ sec}^{-1}$ ]
$k_{\text{rad}}$	= radiative decay rate (Einstein A) coefficient [ $\text{sec}^{-1}$ ]
$k_{\text{wall}}$	= wall deactivation rate coefficient [ $\text{sec}^{-1}$ ]
$k_{\text{wall1}}$	= wall deactivation rate coefficient for $\text{Br}^*$ [ $\text{sec}^{-1}$ ]
$k_{\text{wall2}}$	= wall deactivation rate coefficient for $\text{CO}_2^\dagger$ [ $\text{sec}^{-1}$ ]
$K$	= proportionality constant for $2.71 \mu\text{m}$ emission [ $\text{watt cm}$ ]
$K'$	= proportionality constant for $4.3 \mu\text{m}$ emission [ $\text{watt cm}$ ]
$l$	= electron orbital angular momentum quantum number (s, p, d, f...)
$l_i$	= electron orbital angular momentum vector
$L$	= total orbital angular momentum quantum number (S, P, D, F...)
$L$	= total orbital angular momentum vector
$m_j$	= quantum number characterizing projection of $J$ onto quantization axis
$m_l$	= quantum number characterizing projection of $L$ onto quantization axis
$m_s$	= quantum number characterizing projection of $S$ onto quantization axis
$M$	= any molecule, collision partner
$n$	= principal quantum number (1, 2, 3...)
$N$	= concentration [ $\text{molec cm}^{-3}$ ]
$p_{\text{Br}_2}$	= partial pressure of $\text{Br}_2$ [torr]
$p_{\text{tot}}$	= total cell pressure [torr]
$\Delta p$	= change in total cell pressure upon initiation of photolysis [torr]
$s$	= electron spin angular momentum quantum number ( $\frac{1}{2}$ )
$s_i$	= electron spin angular momentum vector
$S$	= total spin angular momentum quantum number
$S$	= total spin angular momentum vector
$V \rightarrow V$	= vibrational-to-vibrational energy transfer/relaxation

- $V_{\text{cell}}$  = total volume of reaction cell  
 $V_{\text{pump}}$  = volume of pump beam within cell (photolysis region)  
 $\varepsilon$  = decadic absorption coefficient [liters mol<sup>-1</sup> cm<sup>-1</sup>]  
 $\lambda$  = axial component of electron orbital angular momentum ( $\sigma, \pi, \delta, \phi \dots$ )  
 $\Lambda$  = axial component of total orbital angular momentum ( $\Sigma, \Pi, \Delta, \Phi \dots$ )  
 $\nu_x$  = quantum of vibrational energy, where  $x = 1, 2, 3 \dots$  represents mode  
 $(\nu_1 \nu_2 \nu_3)$  = vibrational energy state of molecule having three vibrational modes  
 $\sigma$  = absorption cross-section [cm<sup>2</sup>] ; axial component of spin angular momentum  
 $\Sigma$  = axial component of total spin angular momentum  
 $\phi$  = quantum yield [dimensionless]  
 $\Omega$  = axial component of total angular momentum

### *Abstract*

Steady-state photolysis experiments were conducted to gain information relevant to the construction of a continuous-wave electronic-to-vibrational pumped infrared laser. An Ar<sup>+</sup> laser ( $\lambda = 488$  nm) was used to produce the electronically excited state Br(<sup>2</sup>P<sub>1/2</sub>) (Br\*) via photolysis of molecular bromine. Energy was then transferred to the near-resonant vibrational state CO<sub>2</sub>(101) (CO<sub>2</sub><sup>†</sup>) via the collisional quenching of Br\* by CO<sub>2</sub>. The dependence of the 2.71  $\mu$ m Br\* and 4.3  $\mu$ m CO<sub>2</sub><sup>†</sup> emissions on CO<sub>2</sub> pressure was measured, as well as the dependence of the 4.3  $\mu$ m emission on pump laser chopping frequency. Unexpected results were obtained in both cases, indicating more detailed modeling of kinetic processes is called for. Additionally, an unexplained long-term decay in the 4.3  $\mu$ m signal was observed, which may have bearing on the construction of closed-system laser devices. Recommendations are made for further research.

# STEADY-STATE KINETICS OF $\text{Br}(^2\text{P}_{1/2}) \rightarrow \text{CO}_2(101)$ ELECTRONIC-TO-VIBRATIONAL ENERGY TRANSFER LASER SYSTEM

## *I. Introduction*

In this experiment, 488 nm laser radiation photodissociates molecular bromine to produce  $\text{Br}(^2\text{P}_{1/2})$  and  $\text{Br}(^2\text{P}_{3/2})$ . Collisional quenching of the electronically excited  $^2\text{P}_{1/2}$  state by carbon dioxide populates the  $\text{CO}_2(101)$  vibrationally excited state via near-resonant electronic-to-vibrational energy transfer. This process is monitored via the 2.71  $\mu\text{m}$   $\text{Br}(^2\text{P}_{1/2})$  and 4.3  $\mu\text{m}$   $\text{CO}_2(101)$  side-fluorescence emissions, under steady-state conditions, to gain information relevant to the construction of a continuous-wave infrared laser operating on the  $\text{CO}_2(101 \rightarrow 100)$  transition. Unexpected results are observed for the  $\text{CO}_2(101)$  emission's pressure-dependence, long-term signal stability, and photolysis laser chopping frequency dependence, indicating further experimentation, more detailed analysis of current data, and possible revision of the existing kinetic model are called for. Recommendations for further research are offered.

### *A. Background*

The United States Air Force is interested in developing compact, powerful, line-tunable infrared lasers, operating in the 3-5  $\mu\text{m}$  or 8-14  $\mu\text{m}$  atmospheric transmission windows, for airborne use in environmental remote-sensing and infrared counter-measures (IRCM) applications. Most significantly, a system producing kilowatts of output power could provide an effective defense against air-to-air and surface-to-air missiles equipped with infrared (IR) seekers. This would increase aircrew survivability, and improve tactical effectiveness against IR missile-defended targets.



Several candidate laser technologies have been considered for such applications, including chemical, semiconductor, optically-pumped, and photolytic. Currently, chemical lasers are too large for use on any but the largest aircraft, and semiconductor lasers lack the necessary power. Optically-pumped lasers, because they rely on direct excitation of specific laser energy levels, require narrow-band, stable pump sources for efficient operation, making them susceptible to shock and vibration in the airborne environment. Molecular lasers pumped by electronic-to-vibrational ( $E \rightarrow V$ ) transfer from photolytically-excited species thus have several advantages. Because photolysis (dissociation of a molecule due to absorption of a photon) can occur over a relatively wide spectral range, wavelength-stability of the pump source is not of great concern. Flexibility in the operating wavelength of the laser is attained via the appropriate choice of molecular lasing species, while line-tunability is provided by the rotational structure of the vibrational laser levels. This yields frequency agility of up to 1  $\mu\text{m}$  for the purpose of defeating infrared counter-countermeasures (IRCCM). The potential for efficiency, scalability, and closed-cycle operation are further advantages of photolytic laser systems.

Atomic bromine is attractive as an energy-transfer species because the  $\text{Br}_2$  and  $\text{IBr}$  molecules are easily photolyzed by 488 nm and 532 nm light, respectively, producing the electronically excited  $\text{Br}(4^2\text{P}_{1/2})$  atom (henceforth indicated by  $\text{Br}^*$ ). This state has an energy level of  $3685.0 \text{ cm}^{-1}$  above the ground electronic state, corresponding to a mid-wavelength infrared (MWIR) emission wavelength of 2.71  $\mu\text{m}$ .  $\text{Br}^*$  is metastable -- having a radiative lifetime of 1.12 sec -- allowing ample time for the efficient transfer of energy to other species by collisional quenching processes, which occur on a much shorter time-scale.

There are several characteristics which describe a good candidate receptor species for the energy given up by  $\text{Br}^*$ . Such a molecule should be as simple as possible (ie preferably a heteronuclear diatomic), so that its partition function allows for fewer

vibrational modes over which to distribute the transferred energy. It should have near-resonant vibrational levels to increase the efficiency of  $E \rightarrow V$  transfer. It should quench  $Br^*$  rapidly -- at least as fast as the parent molecule  $Br_2$ . It should have IR vibrational transitions within the atmospheric transmission windows. Finally,  $E \rightarrow V$  transfer should excite an average number of quanta greater than 1.5, so that an inversion can be achieved between levels higher than the ground state. Examples of receptor molecules which appear to meet many or all of these criteria include  $CO_2$ ,  $H_2O$ , and  $NO$ .

Pulsed lasers have been demonstrated based on  $E \rightarrow V$  transfer from  $Br^*$  to these and other small molecules, such as  $HCN$  and  $N_2O$ .  $NO$ , with a  $5.3 \mu m$  ( $v = 2 \rightarrow 1$ ) lasing transition, appears desirable as a lasing species for the reasons outlined above; however it has been found in practice to be an inefficient converter of  $Br^*$  energy.  $H_2O$  has the disadvantage that all of its lasing transitions fall within strong atmospheric water absorption bands.  $CO_2$  has been found to lase at  $14.1$ ,  $10.6$ , and  $4.3 \mu m$ , with the latter representing a particularly strong emission and relatively efficient transfer process.

Although several examples of pulsed  $E \rightarrow V$  lasing have been reported, there are no known examples of continuous-wave operation. Continuous-wave (CW) IR lasers may offer advantages over pulsed lasers in the Air Force applications described earlier. The higher average power of a CW output is generally more effective at disabling an IR sensor/seeker than the higher peak power of a pulsed output. Lower peak power may also reduce undesirable plasma effects at the target. Further, due to the nonlinear response of the atmosphere to transmitted power, a CW device may have better beam-propagation characteristics than its pulsed counterpart. Finally, CW operation could lead to future space-based, solar-pumped laser platforms.

Because the  $4.3 \mu m$  emission of  $CO_2(101)$  (hereafter indicated by  $CO_2^\dagger$ ) falls within an atmospheric  $CO_2$  absorption band, this species does not seem a likely candidate for practical device employment. However, because of the strength and relative

efficiency of lasing on the  $\text{CO}_2(101 \rightarrow 100)$  transition, previous success with pulsed lasers, and existing body of data on  $\text{Br}^*\text{-CO}_2$  kinetics, this system does seem a good choice for development of CW  $\text{E} \rightarrow \text{V}$  laser technology. It is for these reasons that  $\text{CO}_2$  was chosen as the  $\text{E} \rightarrow \text{V}$  receptor species in this research.

## *B. Current Knowledge*

### *1. Br\* Quenching by E → V Transfer*

The investigation of  $\text{E} \rightarrow \text{V}$  transfer from  $^2\text{P}_{1/2}$  states of halogen atoms to molecular quenching species began in 1970 with the work of Donovan and Husain.<sup>(4)</sup> These researchers reported  $\text{Br}^*$  quenching rates for several molecular species, including noble gases, diatomic molecules, and the  $\text{Br}_2$  molecule itself. They noted orders-of-magnitude differences in quenching efficiency between diatomics and noble gases, and explained expected differences between fast and slow quenching species in terms of their energy transfer mechanisms. Many of the quenching rates they reported were found to be too high and not repeatable by later investigators. For example, Donovan and Husain reported a bromine self-quenching rate of  $19.0 \times 10^{-12} \text{ cm}^3 \text{ molec}^{-1} \text{ sec}^{-1}$ , whereas later workers reported a range for this constant of  $0.47\text{-}1.2 \times 10^{-12} \text{ cm}^3 \text{ molec}^{-1} \text{ sec}^{-1}$ .<sup>(11)</sup>

In 1973, Leone and Wodarczyk were the first to directly measure  $\text{E} \rightarrow \text{V}$  transfer using pulsed laser photolysis and time-resolved detection of IR emissions.<sup>(15)</sup> Using a frequency-doubled  $\text{Nd}^{3+}\text{:YAG}$  laser and wavelength-selective filters, the researchers measured the absolute rate coefficients for transfer of energy to the ( $\nu = 1$ ) states of  $\text{HCl}$  and  $\text{HBr}$ , finding at least 50 % of  $\text{Br}^*$  quenching by  $\text{HX}$  is due to  $\text{E} \rightarrow \text{V}$  transfer. The rates for  $\text{Br}_2$  self-quenching and  $\text{HX}$  quenching without excitation of the ( $\nu = 1$ ) state were also determined.

Later, Wodarczyk and Sackett conducted similar studies on  $\text{Br}^*$  and  $\text{HF}$  with an improved apparatus, in which incident and transmitted laser intensity were monitored.<sup>(30)</sup>

In this way, the workers could continuously measure the mole fraction of  $\text{Br}_2$  in the reaction cell. They found the transfer of energy to HF extremely rapid, and attributed this to the likely availability of several near-resonant ro-vibrational transitions.

Hariri and others extended the investigation of  $\text{E} \rightarrow \text{V}$  transfer to larger molecules in 1976 and 1977. <sup>(7, 8)</sup> A flashlamp-pumped dye laser was used to photolyze  $\text{Br}_2$ , with HCN,  $\text{CO}_2$ , COS, and  $\text{CS}_2$  serving as quenching species. Measurements of time-resolved fluorescence were again employed, yielding a self-quenching rate for  $\text{Br}_2$  of  $1.2 \times 10^{-12} \text{ cm}^3 \text{ molec}^{-1} \text{ sec}^{-1}$ . This research also indicated that  $\text{CO}_2$  was more efficient than COS or  $\text{CS}_2$  by an order of magnitude at quenching  $\text{Br}^*$ , that approximately 40 % of quenching collisions led to the excitation of one  $\nu_3$  quantum per  $\text{CO}_2$  molecule, and that the  $\text{CO}_2(101)$  state was the major product channel.

In 1990, Sedlacek, Weston, and Flynn used a diode laser in high-resolution time-resolved spectroscopy to confirm by direct observation that  $\text{CO}_2(101)$  is indeed the primary  $\text{Br}^*$  quenching product. <sup>(22)</sup> Further, they found that the Fermi resonant  $\text{CO}_2(021)$  state receives negligible energy, most likely due to the sensitivity of dipole-quadrupole long range forces to  $\text{E} \rightarrow \text{V}$  energy defect. These workers reported  $87 \pm 15 \%$  of  $\text{Br}^*$  quenching collisions with  $\text{CO}_2$  excite the (101) state, and measured  $\text{E} \rightarrow \text{V}$  and  $\text{V} \rightarrow \text{V}$  rates similar to those reported previously.

The  $\text{Br}^*$  quenching rates for 28 previously-studied species were compiled and reported by Tate in his 1991 AFIT thesis work. <sup>(28)</sup> He noted that, in many cases, wide disagreement existed between different reported values for the same rate. With the objective of resolving earlier discrepancies, Tate employed an  $\text{Ar}^+$  laser and steady-state photolysis techniques to find quenching rates for several molecular species relative to the known self-quenching rate of  $\text{Br}_2$ . He then attempted to calibrate his results by measuring the quenching rate of  $\text{CO}_2$  and comparing this result to the best previously-established value. This attempt was unsuccessful, however, due to limitations in the 2.71

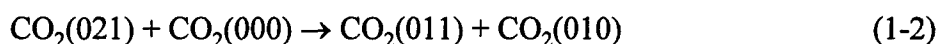
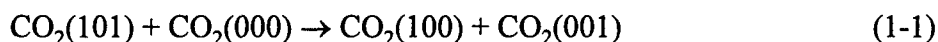
$\mu\text{m}$  bandpass filter used in the experiment. Tate was also unsuccessful in his attempt to model the  $\text{CO}_2$  quenching data, in part because he misidentified the source of the fluorescent emissions observed through the inadequate filter.

Katapski later attempted to use an excimer-pumped dye laser and time-resolved fluorescence measurements to study  $\text{CO}_2$  quenching of  $\text{Br}^*$ , but was also frustrated by a poor  $2.71 \mu\text{m}$  filter. <sup>(14)</sup> Additionally, he felt that  $\text{CO}_2$  contamination of his  $\text{Br}_2$  sample might have affected his results.

In his 1993 AFIT dissertation, Johnson identified the source of Tate's problem by pointing out that Tate had in fact observed the stronger  $4.3 \mu\text{m}$   $\text{CO}_2^+$  emission, rather than the intended  $2.71 \mu\text{m}$   $\text{Br}^*$  emission, due to the out-of-band transmission characteristics of the filter he used. <sup>(11)</sup> Thus, Tate had recorded data for the quenching of  $\text{CO}_2^+$  rather than  $\text{Br}^*$ . Johnson did not attempt to correct Tate's model for steady-state emission intensity versus  $\text{CO}_2$  pressure, but did, with an improved  $2.71 \mu\text{m}$  filter, continue Tate's efforts to obtain consistent  $\text{Br}^*$  quenching data for a variety of atomic and molecular species. Starting with pulsed excitation, Johnson measured the absolute rates for  $\text{Br}_2$  and  $\text{CO}_2$  quenching of  $\text{Br}^*$ , in order to establish a baseline. Next, he employed Tate's steady-state approach to measure the quenching rates of  $\text{CO}_2$  and 22 additional species relative to the  $\text{Br}_2$  baseline. The rates obtained for  $\text{CO}_2$  via the two different methods were in good agreement with one-another and with previously-reported values, implying accurate data had been obtained for all species tested. Johnson reported a  $\text{Br}_2$  self-quenching rate of  $1.24 \times 10^{-12} \text{ cm}^3 \text{ molec}^{-1} \text{ sec}^{-1}$  and a  $\text{CO}_2$  quenching rate of  $1.48$  (pulsed) /  $1.32$  (steady-state)  $\times 10^{-11} \text{ cm}^3 \text{ molec}^{-1} \text{ sec}^{-1}$ , which agreed to within experimental error. He also measured the collision-free deactivation rate for his apparatus, and studied the effects of diffusion, wall recombination, and three-body recombination on the atomic bromine concentration in the cell.

## 2. $E \rightarrow V$ Pumped Lasers

Progress in applying the method of  $E \rightarrow V$  transfer to construction of a laser began in 1975 with the work of Peterson, Wittig, and Leone.<sup>(20)</sup> Using flash photolysis of  $\text{Br}_2$ , stimulated emission was observed from  $\text{CO}_2$ ,  $\text{N}_2\text{O}$ ,  $\text{HCN}$ , and  $\text{C}_2\text{H}_2$ . These workers went on in 1976 to demonstrate a pulsed  $\text{CO}_2$  laser, pumped via flash photolysis of  $\text{Br}_2$ , and operating at 4.3, 10.6, and 14.1  $\mu\text{m}$ .<sup>(21)</sup> Observations of 4.3 and 14.1  $\mu\text{m}$  emissions indicated the (101) and (021) states of  $\text{CO}_2$  receive the most transferred energy. The 4.3  $\mu\text{m}$  emission, representing  $2304 \text{ cm}^{-1}$  of energy, was assigned to the P-branch of either the (101 $\rightarrow$ 100) or the (021 $\rightarrow$ 020) band. This transition was found to be very strong, resulting in lasing at 4.3  $\mu\text{m}$  even when  $\text{CO}_2$  was present only as an impurity in a  $\text{Br}_2$ -COS system. Lasing on this transition was found to cut off at  $\text{CO}_2$  pressures above 0.15 torr, attributed to rapid  $V \rightarrow V$  relaxation of the upper laser level by one of the known processes



It was felt that the recombination of Br atoms to form  $\text{Br}_2$  and the chemical inertness of  $\text{CO}_2$  would make operation of a sealed-off laser system feasible. However, a slow degradation of 4.3 and 14.1  $\mu\text{m}$  output was observed for dilute  $\text{CO}_2$  mixtures during continued use of a single fill. This was believed to be caused by leakage and outgassing of contaminants such as  $\text{O}_2$  and  $\text{H}_2\text{O}$ , which are rapid quenchers of  $\text{Br}^*$ , into the system.

In 1991, Pastel and others demonstrated pulsed  $\text{Br}^*$ ,  $\text{CO}_2$ , and  $\text{HCN}$  lasers using a doubled Nd:YAG laser operating at 532 nm to photolyze IBr.<sup>(18)</sup> Lasing was observed at 4.3  $\mu\text{m}$  for  $\text{CO}_2$  pressures of 0.25-1.0 torr and IBr pressures of 1-5 torr. Again, quenching of the upper laser level by ground state  $\text{CO}_2$  was implicated in the failure to lase at higher  $\text{CO}_2$  pressures. The researchers noted that, given the  $E \rightarrow V$  rate from  $\text{Br}^*$  to  $\text{CO}_2^\dagger$ , only

8 % of the available Br\* energy is transferred to CO<sub>2</sub> at 0.7 torr with a 400 ns pulse; thus, future pulsed designs should use Q-switching to extract maximum power.

Johnson's 1993 AFIT work also included pulsed laser demonstrations using the doubled-Nd:YAG laser technique originated by Pastel et al. Johnson recreated the Br\* and CO<sub>2</sub><sup>†</sup> results of these workers, then examined the ( $v = 2 \rightarrow 1$ ) lasing transition of NO. NO was found to be a poor candidate for a Br\*-M molecular laser, achieving an overall conversion efficiency of only 0.012 % compared to the 0.16 % attained by CO<sub>2</sub>. Johnson noted that the strength of the CO<sub>2</sub>(101 $\rightarrow$ 100) transition makes it a good candidate for follow-on research into the possibility of continuous-wave operation.

Subsequent attempts by Perram and Johnson to explain Johnson's pulsed laser data indicated possible shortcomings in the kinetic model applied. <sup>(19)</sup> In particular, the pulse shapes of the CO<sub>2</sub> laser at various CO<sub>2</sub> pressures were not satisfactorily accounted for by currently understood kinetic processes.

### *C. Problem Statement*

Difficulties in modeling the results of previous pulsed and steady-state E $\rightarrow$ V experiments indicate the need for further study and possible revisions to accepted kinetic models. Detailed knowledge of relevant kinetic processes is crucial to the design of both pulsed and CW laser devices. Studies of E $\rightarrow$ V laser systems under steady-state conditions are needed to gain insight into the special performance characteristics of CW devices.

### *D. Scope*

The primary goal of this research is to gain a better understanding of the steady-state kinetics of Br<sub>2</sub>-CO<sub>2</sub> photolytic laser systems. Measurements of Br \* and CO<sub>2</sub><sup>†</sup> side-fluorescence will be performed under near-steady-state conditions to learn more about CW device characteristics and identify favorable conditions for lasing. A simple model

for the dependence of  $\text{CO}_2^+$  emissions on  $\text{CO}_2$  pressure will be developed and tested against experimental data.

A secondary goal for this work will be to demonstrate a working CW device based on the  $4.3\text{ }\mu\text{m}$   $\text{CO}_2(101\rightarrow100)$  lasing transition.

#### *E. Approach*

An apparatus similar to those used in previous pulsed-laser work will be assembled, keeping in mind the dual objectives of monitoring steady-state side-fluorescence and demonstrating a CW laser device. The proposed apparatus is depicted in Figure 1-1. Using the same apparatus for all experiments allows accurate assessment of device performance, and automatically accounts for any device-specific behavior.

A CW  $\text{Ar}^+$  laser operating at 488 nm will be used to photolyze  $\text{Br}_2$  in a mixture with  $\text{CO}_2$ .  $\text{E}\rightarrow\text{V}$  transfer from  $\text{Br}^*$  to  $\text{CO}_2$  will result in the excitation of  $\text{CO}_2^+$ . Steady-state emissions of  $\text{Br}^*$  and  $\text{CO}_2^+$  will be observed as functions of total cell pressure,  $\text{CO}_2$  concentration, and pump laser chopping frequency. From this data, both universal and system-specific kinetic parameters will be determined, and compared to those found in previous research. A model for the expected functional relationship between  $\text{CO}_2^+$  concentration/emissive intensity and  $\text{CO}_2$  pressure will be developed and its predictions compared to experimental data. The completeness and accuracy of this model will be assessed, and changes proposed as necessary.

Once the kinetics of the system have been satisfactorily characterized, if time permits, an attempt will be made to demonstrate a CW IR laser pumped by the steady-state photolysis of  $\text{Br}_2$ . The cavity will be aligned using the HeNe laser and pellicle beam splitter, after which the beam splitter will be removed. The  $\text{Ar}^+$  pump laser will be aligned so as to cross the lasing axis, creating a gain region within the laser cavity. Favorable lasing conditions (eg gas mixture, chop-rate), as determined in the first part of



the experiment, will be established, and detectors will be positioned to record both stimulated and spontaneous emission. If lasing is achieved, the performance of the laser will be optimized, and its relationship to the same variables tested in the first part of the experiment will be assessed.

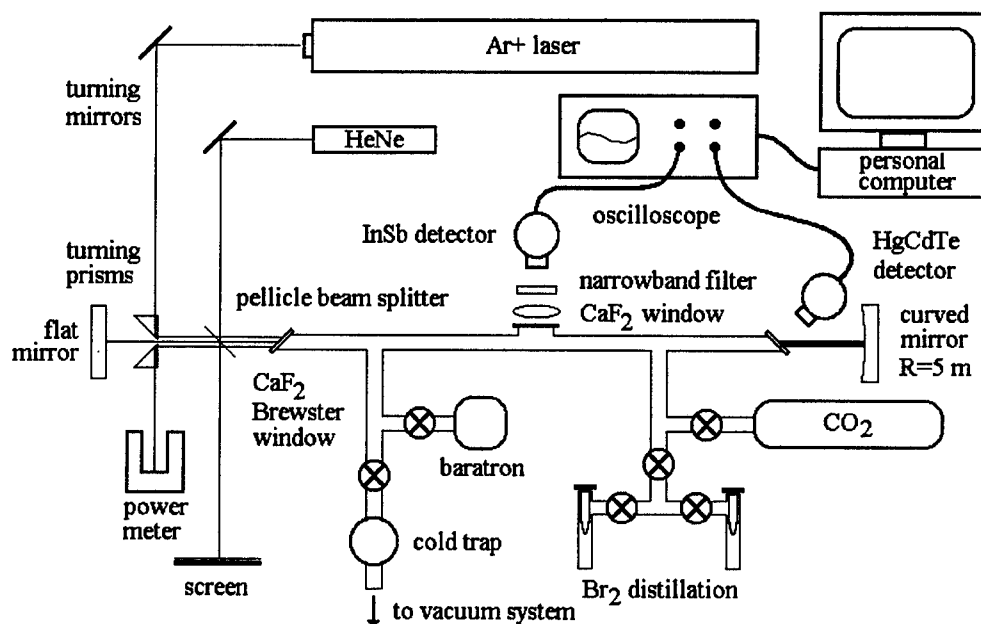


Figure 1-1. Proposed Experimental Apparatus

#### F. Summary

This completes the introductory material for this thesis. Chapter II will explain the theory of  $E \rightarrow V$  transfer kinetics, and will introduce the proposed model for  $\text{CO}_2^+$  pressure-dependence. Chapter III will describe in detail the experimental apparatus and procedures employed in this research. Chapter IV will present the results of each experiment and the analysis of its data. Chapter V will list the conclusions reached, and offer recommendations for continued investigation.

## II. Theory

The goal of this thesis research is to gain a better understanding of the steady-state kinetics of a  $\text{Br}_2\text{-CO}_2$  system under photolysis, essential to the development of a continuous-wave IR laser exploiting the  $\text{E} \rightarrow \text{V}$  transfer of energy from the excited Br atom to the  $\text{CO}_2$  molecule. This chapter examines the background theory necessary to developing such an understanding. The topics covered include spectroscopic notation, characteristics of bromine and carbon dioxide, absorption, photolysis, and gas kinetics, concluding with a proposed model for the quenching of vibrationally excited  $\text{CO}_2$  by ground-state  $\text{CO}_2$ .

### A. Spectroscopic Theory

#### 1. Atomic Spectroscopy

Free atoms (ie those not bound in a solid) possess energy in two forms, translational and electronic. The electronic energy state of the atom depends on the configuration of all of its electrons, which fill a series of energy levels known as shells and subshells in order, according to the Aufbau principle, as follows

$$1s^2 2s^2 2p^6 3s^2 3p^6 4s^2 3d^{10} 4p^6 5s^2 4d^{10} 5p^6 6s^2 \dots$$

The levels are represented by terms of the form  $nl^x$ , where  $n$  is the principal quantum number representing a shell,  $l$  is the orbital angular momentum quantum number representing a subshell or *orbital*, and  $x$  is the number of electrons in the filled subshell. In this case,  $l$  values of 0, 1, 2, 3... are denoted by the letters s, p, d, f... By convention, the filled subshells are understood and dropped from the notation when reporting the configuration of an atom, leaving only the description of the outer, unfilled orbital. For example,  $3p^3$  gives the ground configuration of phosphorus, with 15 electrons total, three of which are in the unfilled 3p orbital. <sup>(25)</sup>

An electron's energy depends on its principle and angular momentum quantum numbers  $n$ ,  $l$ ,  $m_l$ ,  $s$ , and  $m_s$ . Here  $l$  represents orbital angular momentum, as above, and  $s$  represents spin angular momentum, where  $n$ ,  $l$ , and  $s$  are always positive, and  $s = 1/2$ . The numbers  $m_l$  and  $m_s$  can be positive or negative, and represent the orientation of the angular momentum vectors they are associated with. The energy of a multielectron atom depends on the total angular momentum obtained by summing the orbital and spin contributions of all of the individual electrons. However, according to the Pauli exclusion principle, full subshells must have equal numbers of electrons with negative and positive  $m$  values, thereby canceling any contribution to the total angular momentum. Thus, as above, only the outer unfilled shell need be considered in the summation. By the same principle, a subshell which is missing one electron is equivalent to that containing only one electron. <sup>(2)</sup>

The Russel-Saunders (or **LS**) coupling scheme defines the total angular momentum vector **J** as

$$\mathbf{J} = \mathbf{L} + \mathbf{S} \quad (2-1)$$

where

$$\mathbf{L} = \sum_i \mathbf{l}_i \quad (2-2)$$

$$\mathbf{S} = \sum_i \mathbf{s}_i \quad (2-3)$$

and

$\mathbf{l}_i$  = electron orbital angular momentum vector

$\mathbf{s}_i$  = electron spin angular momentum vector

Two new quantum numbers  $J$  and  $m_j$  accompany **J**, with allowed values given by <sup>(1)</sup>

$$|L - S| \leq J \leq L + S \quad (2-4)$$

$$-J \leq m_j \leq +J \quad (2-5)$$

where

$L$  = total orbital angular momentum quantum number

$S$  = total spin angular momentum quantum number

The quantum state of the atom may now be labeled by the term symbol

$$N^{2S+1}L_J$$

where  $N$  represents the orbit number,  $2S+1$  is the multiplicity of the state,  $L = 0, 1, 2, 3, \dots$  is represented by the capital letters S, P, D, F..., and  $J$  retains its numeric value. For example, the ground state of the sodium atom, with electronic configuration  $3s^1$ , has the term symbol  $3^2S_{1/2}$ , read as "three doublet S one-half." <sup>(29, 26)</sup> The energies of electronic states are ordered according to the term symbols and Hund's rules. The primary ordering is determined by the multiplicity, where higher multiplicity indicates lower energy. Next, for states with the same multiplicity, higher values of  $L$  indicate lower energy. Finally, for outer subshells less than half full, a larger  $J$  implies higher energy; for subshells more than half full, a larger  $J$  implies lower energy. The energy differences between these states define the spectroscopic *fine structure*. Energy shifts which can occur due to the magnetic quantum number  $m_j$  (Zeeman splitting) or coupling between  $J$  and the nuclear spin  $I$  (*hyperfine structure*) are not a factor in this work. <sup>(1)</sup>

## 2. Molecular Spectroscopy

When two or more atoms join as a molecule, a new state is formed in which wave functions now describe the orbits of electrons with respect to the molecule as a whole. Several models exist which closely approximate the observed characteristics of molecular formation. One model, molecular orbital theory, is analogous to the atomic orbital theory discussed earlier. The energy levels and orbital configurations of electrons in the

molecule are defined by quantum numbers, and are occupied according to the same basic principles as in the atomic case. In the *linear combinations of atomic orbitals* (LCAO) model, applied to diatomic molecules, atomic orbital wave functions are added or subtracted to produce new molecular orbital wave functions. When two s-orbitals are combined, the result is a bound state, wherein the electronic charge is concentrated in the region between the nuclei, and a higher-energy unbound state, wherein the electronic charge is concentrated outside this region. For example, adding two 1s wave functions yields the orbitals  $1\sigma_g$  and  $1\sigma_u^*$ , where s is the original atomic orbital type,  $\sigma$  is the molecular orbital type, \* indicates the *antibonding* state, and g/u refers to even/odd inversion symmetry. Two p orbitals can combine *end-to-end* or *side-to-side* to form  $\sigma$  or  $\pi$  orbitals, respectively. In the case of  $\sigma$  orbitals, the antibonding state has odd symmetry, whereas in  $\pi$  orbitals the antibonding state has even symmetry. Analogous to s, p, d, f atomic orbitals, the  $\sigma$ ,  $\pi$ ,  $\delta$ ,  $\phi$  molecular orbitals are formed and filled as in this example of molecular nitrogen ( $N_2$ )

$$(1\sigma_g)^2(1\sigma_u)^2(2\sigma_g)^2(2\sigma_u)^2(2p\sigma_g)^2(2p\pi_u)^4$$

Considering the bonding/antibonding counterparts  $1\sigma_{g/u}$  and  $2\sigma_{g/u}$  to cancel one-another, three electron pairs remain in bonding orbitals, and the molecule is said to have a triple bond. <sup>(2)</sup>

As in an atom, the energy of an electron in a molecule depends on its principal quantum number  $n = 1, 2, 3...$  and its orbital angular momentum  $l = 0, 1, 2, 3...$ , represented as before by the letters s, p, d, f.... The total orbital angular momentum  $L$  of a molecule may be found by summing the contributions from individual electrons. However, in a diatomic molecule, the angular momentum component along the internuclear axis is more important than  $l$  alone. Thus, the axial component  $\lambda$  of orbital angular momentum is defined by  $\lambda \equiv |l_z|$ ,  $l_z = 0, \pm 1, \pm 2, \pm 3...$ , and  $\lambda = 0, 1, 2, 3...$  is

represented by the molecular orbital symbols  $\sigma, \pi, \delta, \phi, \dots$ . Now the total *axial* angular momentum is defined as

$$\Lambda = \left| \sum_i \lambda_i \right| \quad (2-6)$$

where  $\Lambda = 0, 1, 2, 3, \dots$ , represented by  $\Sigma, \Pi, \Delta, \Phi, \dots$ . The absolute value bars indicate that the orientation of  $\lambda_i$  must be preserved in the summation. The total spin angular momentum  $S$  may also be computed by summing contributions from each electron, and this approach is often used in lieu of summing axial components, as spin-axial coupling is weak. If needed, the axial spin components are identified by  $\sigma_i$ , and the total axial spin is defined as

$$\Sigma = \left| \sum_i \sigma_i \right| \quad (2-7)$$

Now the axial component of the total angular momentum is given by

$$\Omega = |\Lambda + \Sigma| \quad (2-8)$$

where  $\Lambda$  and  $\Sigma$  may have the same or opposite directions along the axis. The term symbol

$$^{2\Sigma+1}\Lambda_{\Omega}$$

representing molecular electronic states may now be introduced, where  $2\Sigma+1$  is the multiplicity, read as *singlet*, *doublet*, etc, and  $\Lambda, \Omega$  are as defined above. It is common to replace  $\Omega$  by *u* or *g*, for the inversion symmetry of the orbital, as this is usually more

informative. When it is desired to include both axial angular momentum and symmetry in the notation, the following form is used

$$^{2\Sigma+1}\Lambda(\Omega_{g/u}^{+/-})$$

where  $\Omega$  and  $u/g$  are as before and  $+/-$  refers to reflection symmetry. <sup>(2)</sup>

As with Hund's rules for atomic states, Hund's coupling cases may be applied to identify and order molecular electronic states. These are limiting cases, and no molecule is perfectly described by any one case. Depending on specifics such as the atoms modeled and internuclear distances, different cases may best apply. For example, case (a), which assumes weak spin-orbit coupling, leads to the states described above. Case (c), which assumes strong spin-orbit coupling, leads to a different set of states described by Mulliken's homonuclear diatomic coupling rules. <sup>(16)</sup> The details of these cases and their correlation to one-another are beyond the scope of this discussion. <sup>(11)</sup>

In addition to its translational and electronic energy, a free molecule can also carry energy in vibrational and rotational form. According to the Born-Oppenheimer approximation

$$E_{\text{tot}} = E_{\text{elect}} + E_{\text{vib}} + E_{\text{rot}} \quad (2-9)$$

these different energy forms are independent from one-another. An approximation to the relative orders of magnitude represented by quanta of each form of energy is given by

$$\Delta E_{\text{elect}} : \Delta E_{\text{vib}} : \Delta E_{\text{rot}} \approx 1 : 10^{-3} : 10^{-6}$$

Thus, a given electronic state can incorporate multiple vibrational substates (typically dozens), which in turn can incorporate multiple rotational states (typically hundreds). Transitions between electronic states always involve a dipole change, and thus always

yield electromagnetic emission/absorption spectra. However, only molecular vibration which causes a change in dipole, or rotation of a molecule having a permanent dipole, can produce such spectra. Whether or not vibrational and rotational transitions can be directly observed, they can always be indirectly observed as *coarse* and *fine structure*, respectively, superimposed on the electronic (or vibrational) spectrum of the molecule. Typically, electronic spectra fall within the ultraviolet-visible region, pure vibrational spectra (those involving only changes of vibrational state) fall within the infrared region, and pure rotational spectra fall within the microwave-radio frequency region. <sup>(2)</sup>

Molecular vibration occurs in one or more *modes*, which describe various bends and stretches of the molecular bonds. The more atoms in a molecule, the more degrees of freedom, and thus vibrational modes, available. For example, the diatomic  $N_2$  molecule has only one mode of vibration, the stretch represented by the quantum number  $v$ , whereas the triatomic  $H_2O$  molecule has three modes of vibration, the symmetric stretch, the bend, and the antisymmetric stretch, represented by the quantum numbers  $v_1$ ,  $v_2$ , and  $v_3$ . Thus, the vibrational state of a molecule having four non-degenerate modes would be indicated by the notation  $(v_1 v_2 v_3 v_4)$ . Molecules resist some forms of distortion more than others, leading to an energy-ordering of the associated quanta, although this ordering does not in general correspond to the numbering of the modes. For example, the  $H_2O$  vibrational quanta are  $v_2$ ,  $v_1$ ,  $v_3$  in order of increasing energy. <sup>(10)</sup>

## B. Bromine and Photolysis

### 1. Atomic Bromine

Bromine (Br) is a group VIIA element and a member of the halogen family, which includes fluorine, chlorine, and iodine. It has atomic number 35, an atomic weight of 79.92, and has two stable isotopes  $^{79}Br$  and  $^{81}Br$  which occur in nearly equal abundance. Its electronic configuration is  $4p^5$ , meaning it is one electron short of a full



valence. <sup>(25)</sup> This gives rise to the term symbol  $4^2P_{3/2}$ , representing the electronic ground state. The electronically excited state  $4^2P_{1/2}$  arises due to spin-orbit splitting, where the term with the lower J value has the higher energy according to Hund's rules. The energy separation between these states is 0.456 eV, equivalent to  $3685\text{ cm}^{-1}$  or a  $2.71\text{ }\mu\text{m}$  transition wavelength, as depicted in Figure 2-1. <sup>(3)</sup> The strongly forbidden electric dipole transition  $^2P_{1/2} \rightarrow ^2P_{3/2}$  makes  $^2P_{1/2}$  a metastable state, with an Einstein A coefficient of  $0.898\text{ s}^{-1}$ , or a radiative lifetime of 1.12 sec. Thus, the fluorescence due to this transition is expected to be very weak. <sup>(11)</sup>

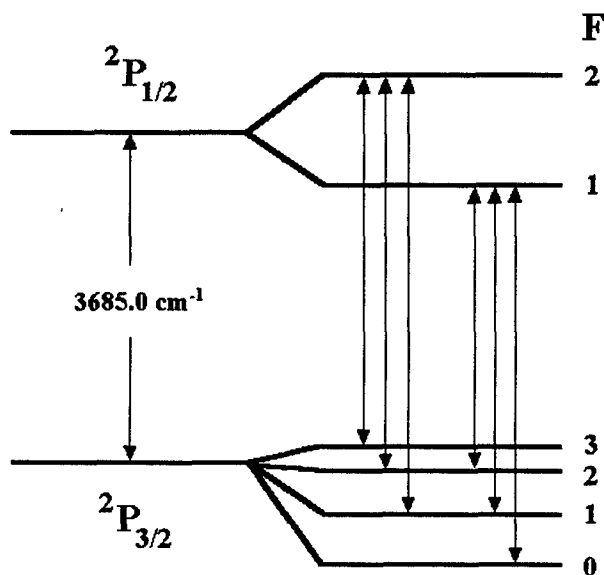


Figure 2-1. Energy level diagram for atomic bromine, showing fine and hyperfine structure. The arrows indicate allowed transitions. <sup>(28)</sup>

## 2. Molecular Bromine

Elemental bromine naturally forms a diatomic molecule,  $\text{Br}_2$ . In this form bromine is a liquid at room temperature, melting at 264 K, and boiling at 332 K. When the two  $4p^5$  orbitals of atomic bromine come together to form  $\text{Br}_2$ , the resulting molecule

has the ground-state electronic configuration  $(4p\sigma_g)^2(4p\pi_u)^4(4p\pi_g)^4(4p\sigma_u)^0$  or (2440), with term symbol  $^1\Sigma_g^+$ . Electrons can be excited into higher-energy configurations, such as (2431) or (2341), giving rise to term symbols  $^1,^3\Pi_u$  and  $^1,^3\Pi_g$  according to Hund's case (a). Here, weak spin-orbit coupling splits triplet-pi states depending on the value of  $\Omega$ , yielding  $^3\Pi(0,1,2)$ . Further, the  $\Omega = 0$  state is split by reflection symmetry into  $0^+$  and  $0^-$ .<sup>(11)</sup> Figure 2-2 is a diagram depicting the interaction potential between the two bromine atoms making up the  $\text{Br}_2$  molecule. The ordinate is energy in eV and the abscissa is internuclear distance in Å. The ground state, as well as bound and unbound excited states relevant to this work are shown, where the dashed line represents an unbound state. Vibrational and rotational levels are omitted for clarity. If sufficient energy is absorbed by the ground or triplet ( $1_u$ ) states, the molecule will dissociate to two ground state bromine atoms. The same outcome will result if the molecule is excited directly to the singlet ( $1_u$ ) state. However, of particular interest in this research, if the  $\text{Br}_2$  molecule can be promoted to the triplet ( $0_u^+$ ) state, additional energy will result in dissociation to one ground state and one excited bromine atom.

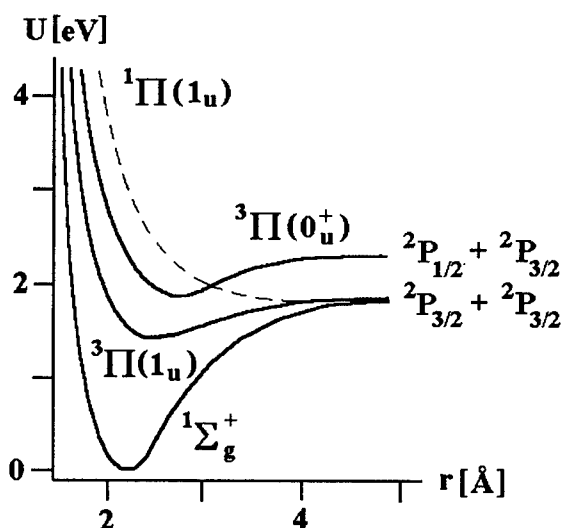


Figure 2-2. Potential energy diagram for molecular bromine. Solid lines represent bound states; dashed line represents an unbound state.<sup>(17)</sup>

### 3. Absorption and Photolysis

As pointed out earlier, molecules can absorb photons via changes in electronic, vibrational, and or rotational state. When monochromatic light passes through a substance capable of absorbing photons at that wavelength, it is attenuated according to Beer's Law

$$I = I_0 e^{-\sigma N l} \quad (2-10)$$

where

$I$  = transmitted intensity [ $\text{W cm}^{-2}$ ]

$I_0$  = incident intensity [ $\text{W cm}^{-2}$ ]

$N$  = concentration [ $\text{molec cm}^{-3}$ ]

$l$  = path length for absorption [ $\text{cm}$ ]

and

$\sigma$  = absorption cross section [ $\text{cm}^2$ ] <sup>(24)</sup>

Figure 2-3 is a graph of molecular bromine's room-temperature absorption cross section for abscissa values in the range 2000-6000 Å. The ordinate shows the *decadic* absorption coefficient  $\epsilon$  given in liters  $\text{mol}^{-1} \text{cm}^{-1}$ , base 10, which can be converted to an absorption cross section using

$$\sigma [\text{cm}^2] = \epsilon \left[ \frac{l}{\text{mol-cm}} \right] \times \frac{1000 \ln 10}{6.02 \times 10^{23}} \approx 3.82 \times 10^{-21} \epsilon \quad (2-11)$$

The graph shows a continuum from 2000-5110 Å and a banded structure from 5110-6000 Å, with peak absorption occurring at approximately 4200 Å. <sup>(17)</sup> The discrete (banded) structure appears due to resonant transitions between ground state and  $^3\Pi(0_u^+)$

vibration levels. <sup>(17)</sup> The absorption coefficient for Br<sub>2</sub> at 4880 Å has been measured as  $94.9 \pm 0.6 \text{ liter mol}^{-1} \text{ cm}^{-1}$  <sup>(23)</sup>, corresponding to an absorption cross-section of  $3.63 \pm 0.02 \times 10^{-19} \text{ cm}^2$ .

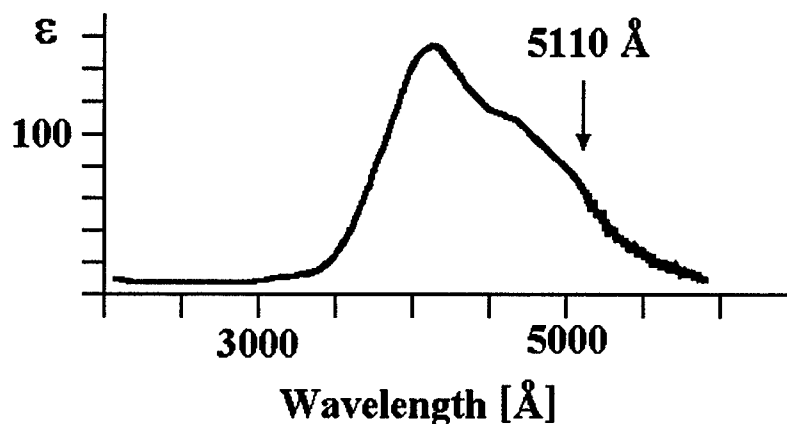


Figure 2-3. Decadic absorption coefficient vs. wavelength for molecular bromine, showing discrete structure above 5110 Å. <sup>(17)</sup>

Earlier discussion showed that a change in electronic state may lead to a molecule's dissociation if a repulsive state is accessed, or if sufficient vibrational energy exists before or is added after the transition. When this dissociation results from the absorption of an incident photon, the process is known as *photolysis*. Generally, changes in vibrational/rotational states alone (due to absorption of infrared or microwave radiation) do not lead directly to molecular dissociation. The range of photon wavelengths over which single-step photolysis is known to occur is about 110 nm (ultraviolet) to 1.3 μm (near-infrared). <sup>(11)</sup> For the bromine molecule, absorption of photons in the 4300-5106 Å range leads to excitation of the  $^3\Pi(0_u^+)$  state, followed by dissociation into one  $^2P_{3/2}$  (ground state) and one  $^2P_{1/2}$  (electronically excited) bromine atom <sup>(17)</sup>, as shown in Figure 2-2. Wavelengths shorter than 4300 Å lead to the unbound  $^1\Pi(1_u)$  state, which dissociates into two ground state bromine atoms <sup>(17)</sup>, while

wavelengths longer than 6300 Å will lead to dissociation only from high vibrational/rotational levels within the Br<sub>2</sub> ground state. <sup>(11)</sup>

As illustrated by the absorption graph above, the probability of a given transition occurring varies with the wavelength of the incident photon. Even at a given wavelength, an absorbed photon does not always access the desired state. The fraction of desired photolysis products actually produced, out of the maximum possible (ie every absorption is productive), is known as the *quantum yield*  $\phi$ . In this work we are interested in the photolysis of Br<sub>2</sub> to produce Br(<sup>2</sup>P<sub>1/2</sub>). The quantum yield for this product has been measured as 0.84 out of a possible 1 per incident photon at 488 nm. <sup>(9)</sup>

### C. Carbon Dioxide and E→V Transfer

The carbon dioxide (CO<sub>2</sub>) molecule is a linear, triatomic molecule joined by double bonds in the chemical configuration O = C = O. It has four modes of vibration, including the symmetric stretch, the in-plane bend, the out-of-plane bend, and the antisymmetric stretch. Since the bends are degenerate, only three quantum numbers are needed to specify the vibrational state of CO<sub>2</sub>, yielding descriptors of the form CO<sub>2</sub>(100), or simply (100) if the CO<sub>2</sub> is understood. <sup>(10)</sup> Figure 2-4 is a simplified energy-level diagram for CO<sub>2</sub> showing the vibrational states and transitions relevant to this work, with the scale calibrated in wave numbers. The Br(<sup>2</sup>P<sub>1/2</sub> → <sup>2</sup>P<sub>3/2</sub>) transition is included in the graph for comparison, the significance of which is discussed below. <sup>(21)</sup>

CO<sub>2</sub> is of interest in this study because, as Figure 2-4 illustrates, its (101) and (021) vibrational states are at nearly the same energy level with respect to the CO<sub>2</sub>(000) ground state as Br(<sup>2</sup>P<sub>1/2</sub>) is with respect to Br(<sup>2</sup>P<sub>3/2</sub>). This condition, described as *near-resonance*, makes possible (and efficient) the transfer of energy from excited atomic bromine to ground-state CO<sub>2</sub> via a collisional process known as *electronic-to-vibrational* (E→V) transfer. This *quenching* process (described in detail in the next section) results



stimulated emission, wherein a photon is released having energy equal to the difference in states. The experiments performed in this work involve only the spontaneous process, which is described in equation form by



where  $A^*$  represents the excited species,  $A$  represents the ground state,  $h\nu$  represents the energy of the emitted photon, and  $k_{\text{rad}}$  is the Einstein A coefficient for spontaneous emission. The units for  $k_{\text{rad}}$  are  $\text{sec}^{-1}$ , indicating that the rate of radiative loss of  $A^*$  depends only on the concentration of  $A^*$ .

Non radiative transitions are the result of *quenching* collisions with other bodies or the walls of the container. Some or all of the excited state's energy may be lost in a single collision, meaning several transitions may occur before the ground state is reached. Collisions with other bodies may result in the transfer of translational, rotational, vibrational, or vibronic energy. <sup>(28)</sup> Taking advantage of a known quenching mechanism, for example an  $E \rightarrow V$  process as in the case of  $\text{Br}(^2P_{1/2})$  and  $\text{CO}_2$ , may allow access to a desired excited state which cannot be directly accessed by other means. A simplified view of such a process is given by



where  $A^*$  is the original electronically excited species,  $B$  is the quenching species,  $A$  is the ground state of  $A^*$ ,  $B^\dagger$  is the desired vibrationally excited state, and  $k_{AB}$  is the rate coefficient for  $B$  quenching  $A^*$ . The units for  $k_{AB}$  are  $\text{cm}^3 \text{ molec}^{-1} \text{ sec}^{-1}$ , indicating the rate of loss of  $A^*$  depends on the concentrations of both  $A^*$  and  $B$ . In the simplified view above, no accounting is given for other mechanisms by which  $B$  may quench  $A^*$ . In fact, many different vibrational levels may be accessible, each having its own associated rate

coefficient <sup>(28)</sup>, so that what is observed is actually a summation of the individual coefficients. In most cases it is not possible to measure these coefficients separately, due to rapid V→V transfer between vibrational states <sup>(20)</sup>, but when isolation of a desired quenching mechanism is possible, it may be reported explicitly, with a second rate assigned to *all other* processes. When more than one quenching species is present, each quenches the excited state at its own rate. Deactivation of the excited species by its *parent* or a lower energy state is known as *self-quenching*. Free-body collisional deactivation is generally much faster than wall or radiative deactivation, and, like the latter, is unaffected by the size and shape of the container.

Collisions with the wall may result in deactivation according to the greatly simplified formula



where  $k_{wall}$  is the rate coefficient for wall deactivation in units of  $\text{sec}^{-1}$ . These units indicate that, like radiative relaxation, wall deactivation depends only upon the concentration of  $A^*$  (to a first approximation). However, unlike the other quenching mechanisms discussed, wall quenching *does* depend on the dimensions of the container, and will vary with the experimental setup. Further, a more detailed model of wall deactivation reveals a pressure dependence, in that radial diffusion rates, which decrease with pressure, can limit wall deactivation. Thus, the total *observed* wall/diffusion rate coefficient is

$$\frac{1}{k_{obs}} = \frac{1}{k_{wall}} + \frac{1}{k_{diff}(p_{tot})} \quad (2-15)$$



where  $k_{\text{wall}} \propto r^{-1}$ , and  $k_{\text{diff}} \propto r^{-2}$ .<sup>(11)</sup> When total pressure is low or does not vary significantly,  $k_{\text{obs}}$  and  $k_{\text{rad}}$  may be combined to form the *collision-free* rate coefficient  $k_0$ .

## 2. Production and Quenching of $\text{Br}^*$

The theory of the preceding sections is now applied to the case of a  $\text{Br}_2/\text{CO}_2$  mixture under steady-state photolysis. The primary reactions which govern the production and quenching of  $\text{Br}(^2\text{P}_{1/2})$  (henceforth referred to as  $\text{Br}^*$ ) are identified below, and from these an equation is constructed which describes the instantaneous time rate of change in  $\text{Br}^*$  concentration  $[\text{Br}^*]$ . Solving this rate equation under steady-state conditions leads to an expression for  $[\text{Br}^*]$  as a function of several variables including  $[\text{Br}_2]$  and  $[\text{CO}_2]$ . Rearranging this result leads to an equation representing an experimental method for determining  $k_0$ .

The following equations describe the life-cycle of  $\text{Br}^*$  from photolysis to recombination, where it is assumed, as in previous work, that reverse reactions and other reactions not included have an insignificant effect on the system.<sup>(11, 28)</sup> Equation (2-16) represents the photolysis of  $\text{Br}_2$  via absorption of a photon of 488 nm light. Equations (2-17) and (2-18) show the collisional  $\text{Br}^*$  quenching mechanisms: self-quenching by  $\text{Br}_2$ , and total (ie *all-channel*) quenching by  $\text{CO}_2$ . Equations (2-19), (2-20), and (2-21) characterize the collision-free  $\text{Br}^*$  quenching processes: radiative decay, wall deactivation, and 3-body collisions involving another Br atom resulting in recombination of  $\text{Br}_2$ .





where

$$k_p = \left( \frac{\phi \sigma}{h\nu} \right)_{488 nm} \quad (2-22)$$

and

$k_p$  = pump rate coefficient [ $\text{cm}^2 \text{ watt}^{-1} \text{ sec}^{-1}$ ]

$\phi$  = quantum yield of  $Br^*$  for photolysis at 488 nm [dimensionless]

$\sigma$  = absorption cross-section for  $Br_2$  at 488 nm [ $\text{cm}^2$ ]

$k_{Br_2}$  = self-quenching rate coefficient for bromine [ $\text{cm}^3 \text{ molec}^{-1} \text{ sec}^{-1}$ ]

$k_{CO_2}$  = all-channel quenching rate coefficient for  $Br^*$  by  $CO_2$  [ $\text{cm}^3 \text{ molec}^{-1} \text{ sec}^{-1}$ ]

$CO_2^\diamond$  = any excited state of  $CO_2$

$k_{2.71}$  = radiative decay rate coefficient for  $Br^*$  [ $\text{sec}^{-1}$ ]

$k_{wall1}$  = wall deactivation rate coefficient for  $Br^*$  [ $\text{sec}^{-1}$ ]

$k_{3B}$  = three-body recombination rate coefficient for  $Br_2$  [ $\text{cm}^6 \text{ molec}^{-2} \text{ sec}^{-1}$ ]

$M$  = any collision partner

The rate equation describing the above processes can be written

$$\begin{aligned} \frac{d[Br^*]}{dt} &= k_p I_p [Br_2] - k_{Br_2} [Br^*][Br_2] - k_{CO_2} [Br^*][CO_2] \\ &\quad - k_{3B} [Br^*][Br][M] - (k_{wall1} + k_{2.71})[Br^*] = 0 \quad (\text{steady-state}) \end{aligned} \quad (2-23)$$

where

$[A]$  = concentration of A [atoms  $\text{cm}^{-3}$ ] or [molec  $\text{cm}^{-3}$ ] as applicable

$I_p$  = pump laser intensity [ $\text{watt cm}^{-2}$ ]

At the total pressures employed in this research (< 10 torr), diffusion in this system has been found to be rapid, allowing the diffusion term in Equation (2-15) to be dropped. <sup>(11)</sup> Thus,  $k_{\text{obs}} \approx k_{\text{wall}}$  ( $k_{\text{obs}}$  is said to be *wall-limited*), and  $k_{\text{wall}}$  may be combined with  $k_{2.71}$  to form the collision-free rate coefficient  $k_0$ . The three-body recombination rate is small, and may also be disregarded in this analysis. <sup>(11)</sup> Equation (2-23) may now be solved for steady-state  $\text{Br}^*$  concentration, with the preceding simplifications adopted, to yield

$$[\text{Br}^*] = \frac{k_p I_p [\text{Br}_2]}{k_{\text{Br}_2} [\text{Br}_2] + k_{\text{CO}_2} [\text{CO}_2] + k_0} \quad (2-24)$$

When information about the rate coefficients in the denominator of Equation (2-24) is desired, measurements of steady-state emissive intensity may be employed. The measured intensity of 2.71  $\mu\text{m}$  side-fluorescence is related to the  $\text{Br}^*$  concentration by a linear proportionality constant  $K$ , the value of which depends on the  $\text{Br}^*$  spontaneous emission rate and the multiple radiometric details of the detector system. The difficulty in assigning an exact value to  $K$  is apparent when the number of contributing factors is considered. However, a standard method exists whereby *relative* emissive intensities may be used to find the relative magnitudes of the coefficients. <sup>(28)</sup> If  $k_{\text{Br}_2}$  is known absolutely, the other coefficients can be determined absolutely by first finding  $k_0$  with no  $\text{CO}_2$  present, then finding  $k_{\text{CO}_2}$  with  $\text{CO}_2$  added. The following is a description of the application of this method to the determination of  $k_0$  when  $k_{\text{Br}_2}$  and  $k_{\text{CO}_2}$  are known.

Taking the ratio of the emissive intensity with  $[\text{CO}_2] = 0$  to that with  $[\text{CO}_2] \neq 0$

$$\frac{I_{2.71}^0}{I_{2.71}} = \frac{K[\text{Br}^*]_{\text{CO}_2=0}}{K[\text{Br}^*]_{\text{CO}_2 \neq 0}} = \frac{k_{\text{CO}_2} [\text{CO}_2]}{k_{\text{Br}_2} [\text{Br}_2] + k_0} + 1 \quad (2-25)$$

where

$I_{2.71}$  = intensity of 2.71  $\mu\text{m}$  Br\* side-fluorescence [watt  $\text{cm}^{-2}$ ]

$I_{2.71}^0$  = intensity of 2.71  $\mu\text{m}$  Br\* side-fluorescence with  $[\text{CO}_2] = 0$  [watt  $\text{cm}^{-2}$ ]

K = proportionality constant [watt cm]

Equation (2.25) has the form of a linear function

$$y = mx + b$$

where

$$x = [\text{CO}_2]$$

$$y = \frac{I_{2.71}^0}{I_{2.71}}$$

$$m = \frac{k_{\text{CO}_2}}{k_{\text{Br}_2} [\text{Br}_2] + k_0} \quad (2-26)$$

$$b = 1$$

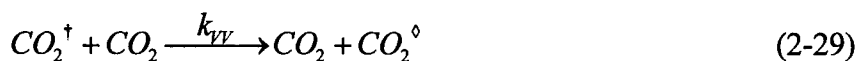
Data for Br\* side-fluorescence intensity vs.  $\text{CO}_2$  pressure may now be collected, each data point divided into the starting (zero  $\text{CO}_2$ ) intensity, and the quotients plotted to form a linear graph. Equation (2-26) can then be applied, using the slope of the graph and the known values of  $k_{\text{Br}_2}$  and  $k_{\text{CO}_2}$  to find  $k_0$  for the apparatus.

### 3. Production and Quenching of $\text{CO}_2^\dagger$

A sequence of steps similar to that followed in the previous section may be used to develop a mathematical description of the production and quenching processes for  $\text{CO}_2(101)$  (henceforth referred to as  $\text{CO}_2^\dagger$ ). Combining this and the previous results for Br\* leads to a proposed simple model for  $\text{CO}_2^\dagger$  emission intensity vs.  $\text{CO}_2$  pressure.

The following equations describe the life-cycle of  $\text{CO}_2^\dagger$  from E $\rightarrow$ V excitation to radiative decay, where it is assumed as in the Br\* case that all significant processes have

been included, an assumption which will be tested by experiment. Equations (2-27) and (2-28) together model the total quenching of  $Br^*$  by  $CO_2$ , in the first case via the  $CO_2(101)$  production channel, and in the second case via all other channels. Equations (2-29) and (2-30) describe the collisional quenching of  $CO_2^\dagger$  by ground-state  $CO_2$  and molecular bromine. Equations (2-31) and (2-32) represent the collision-free wall and radiative deactivation processes.



where

$k_{EV}$  = quenching rate coefficient for  $Br^*$  into  $CO_2(101)$  [ $cm^3 \text{ molec}^{-1} \text{ sec}^{-1}$ ]

$k_{other}$  = quenching rate coefficient for  $Br^*$  into  $CO_2(\text{not } 101)$  [ $cm^3 \text{ molec}^{-1} \text{ sec}^{-1}$ ]

$k_{VV}$  = total  $V \rightarrow V$  relaxation rate for  $CO_2^\dagger$  [ $cm^3 \text{ molec}^{-1} \text{ sec}^{-1}$ ]

$k_{QB}$  = quenching rate coefficient for  $CO_2^\dagger$  by  $Br_2$  [ $cm^3 \text{ molec}^{-1} \text{ sec}^{-1}$ ]

$k_{wall2}$  = wall deactivation rate coefficient for  $CO_2^\dagger$  [ $\text{sec}^{-1}$ ]

$k_{4.3}$  = radiative decay rate coefficient for  $CO_2^\dagger$  [ $\text{sec}^{-1}$ ]

Note that  $k_{EV}$  and  $k_{other}$  together form the all-channel rate coefficient  $k_{CO_2}$ . Since we are primarily interested in the production of  $CO_2(101)$ , this quenching channel has

been separated from all others. The rate equation for production and loss of  $\text{CO}_2^\dagger$  which follows from the above is

$$\begin{aligned} \frac{d[\text{CO}_2^\dagger]}{dt} &= k_{EV}[\text{Br}^*][\text{CO}_2] - k_{VV}[\text{CO}_2^\dagger][\text{CO}_2] - k_{QB}[\text{CO}_2^\dagger][\text{Br}_2] \\ &\quad - (k_{\text{wall}2} + k_{4.3})[\text{CO}_2^\dagger] = 0 \quad (\text{steady-state}) \end{aligned} \quad (2-33)$$

As before, wall-limited operation is assumed, and the collision-free rate coefficients are combined into a single coefficient  $k_0' = k_{\text{wall}2} + k_{4.3}$ . Solving Equation (2-33) for steady-state  $\text{CO}_2^\dagger$  concentration yields

$$[\text{CO}_2^\dagger] = \frac{k_{EV}[\text{Br}^*][\text{CO}_2]}{k_{VV}[\text{CO}_2] + k_{QB}[\text{Br}_2] + k_0'} \quad (2-34)$$

Substituting Equation (2-24) for steady-state  $\text{Br}^*$  concentration into Equation (2-34) gives

$$[\text{CO}_2^\dagger] = \left\{ \frac{k_{EV}[\text{CO}_2]}{k_{VV}[\text{CO}_2] + k_{QB}[\text{Br}_2] + k_0'} \right\} \left\{ \frac{k_P I_P[\text{Br}_2]}{k_{\text{CO}_2}[\text{CO}_2] + k_{\text{Br}_2}[\text{Br}_2] + k_0} \right\} \quad (2-35)$$

which has the form

$$y = \frac{A x}{(B x + 1)(C x + 1)} \quad (2-36)$$

where

$$x = [\text{CO}_2]$$

$$y = [\text{CO}_2^\dagger]$$

$$B = \frac{k_{VV}}{k_{QB}[Br_2] + k_0}$$

$$C = \frac{k_{CO_2}}{k_{Br_2}[Br_2] + k_0}$$

As in the case of the Br\* emission, the measured intensity of the 4.3  $\mu\text{m}$  CO<sub>2</sub><sup>†</sup> emission is related to [CO<sub>2</sub><sup>†</sup>] by an unknown constant K'. Unfortunately, the same procedure used to eliminate K cannot be used here to eliminate K' because the emission intensity at [CO<sub>2</sub>] = 0 is zero! Moreover, this or any similar technique involving an inversion of the [CO<sub>2</sub><sup>†</sup>] vs. [CO<sub>2</sub>] function <sup>(28)</sup> would not lead to a simplified linear form. An evaluation of this model must therefore rely on a straightforward fit of Equation (2-36) to the experimental data. An overall assessment of this functional form should be possible despite our ignorance of K' and some of the rate coefficients (see Chapter IV). If a satisfactory fit is obtained, wherein the constants A, B, and C assume reasonable values based on known and estimated rate coefficients, it can be assumed that equations (2-27) - (2-32) represent an adequate description of the significant kinetic processes in the Br\*-CO<sub>2</sub><sup>†</sup> system. However, if no reasonable adjustment of coefficients and scaling factors leads to an acceptable fit, then it must be concluded that the model is incomplete.

A description of the analytical tools to be applied to the experimental data having been provided, it is hoped that the model for CO<sub>2</sub><sup>†</sup> quenching proves sufficiently detailed to explain observations or, if not, points the way to a more complete model. The experimental procedures followed in evaluating this model are described in the next chapter.

### *III. Experiment*

One of the objectives of this research was to demonstrate a working, CW E→V laser prototype. For this reason, the configuration chosen for the apparatus was very similar to that recently used by Johnson in demonstrating pulsed-photolysis Br\* and E→V lasers, rather than the simple reaction-cell arrangements used by Johnson and others in studying Br\* steady-state kinetics. <sup>(11)</sup> Prior to any attempt at lasing, the kinetics of the system were to be studied via side-fluorescence measurements, to help determine the conditions most favorable for lasing. The interesting and unexpected results obtained in this phase of the experiment led to further investigation, ultimately leaving insufficient time to proceed to the lasing phase. Although the apparatus was not originally intended (nor optimized) solely for side-fluorescence studies, it was felt that the kinetics data obtained using this system would most accurately reflect that of a practical laser device.

#### *A. Experimental Apparatus*

This section describes the experimental setup used in this research. Figure 3-1 shows the layout of the main components in schematic form. Detailed descriptions of the laser cavity, gas-handling, photolysis, detection, and data-collection subsystems follow.

##### *1. Laser Cavity*

The laser cavity consists of the gas cell/gain medium, Brewster windows, and two end-mirrors. The gas cell is constructed from 90 cm of straight 1/2" OD glass tubing, connected to the gas-handling system and the Brewster windows via Cajon Ultra-Torr T-fittings. A 1" CaF<sub>2</sub> window is mounted in the center of the cell to permit observation of the 2.7 and 4.3 μm IR side-fluorescence. The ends of the cell are capped by 2" lengths of 1/2" OD tube with 1" CaF<sub>2</sub> windows affixed at Brewster's angle (for 4.3 μm radiation) of



54.6 deg from normal. The Brewster windows are angled downward to minimize hazardous reflection and maximize transmission of the vertically-polarized pump laser.

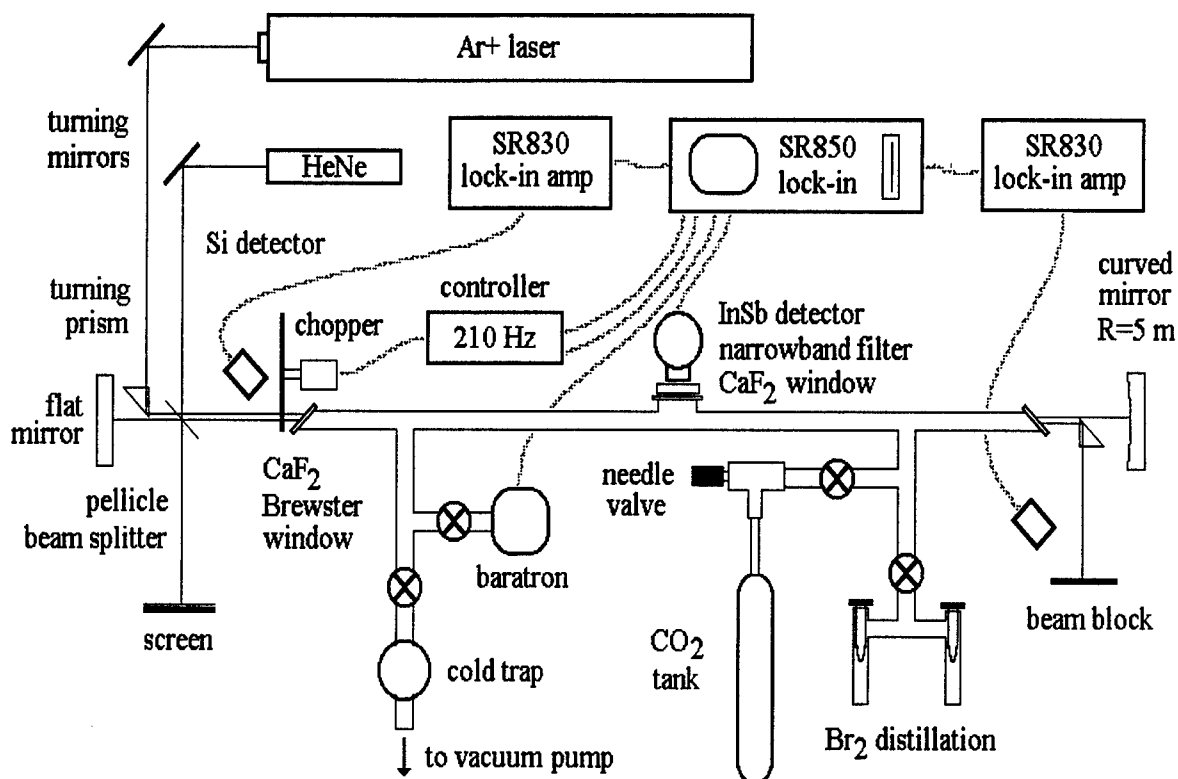


Figure 3-1. Diagram of experimental apparatus showing layout of major components and control/data connections.

All CaF<sub>2</sub> windows are all Ealing model 36-1741, and are attached using 3M Torr-Seal compound. The cavity reflectors are CVI Laser Corp. gold-coated mirrors, with  $R > 0.99$ ; one is flat the other has a 5 m radius of curvature. The mirrors are placed 1.5 m apart, well within the stability limit of the cavity. Mirror alignment is accomplished by introducing the beam of an Oriel 5 mW HeNe laser into the cavity via a pellicle beam splitter, which is removed after alignment is completed. The mirrors are adjusted until the reflected spots all overlap, and a scintillating interference pattern is observed on the Brewster windows and mirrors. As no output coupler is used, 4.3  $\mu\text{m}$  laser radiation is measured via scatter off of the Brewster windows.

## 2. Gas-Handling

The gas-handling subsystem consists of the Br<sub>2</sub> distillation section, the CO<sub>2</sub> tank, and the vacuum assembly. The molecular bromine sample (Spectrum 99.5%) is stored in and purified using the distillation apparatus. This is composed of two 1/2" OD glass test tubes connected to one-another via Kontes Teflon-stoppered glass valves and a Cajon T, which is in turn connected to the rest of the system via a Teflon valve. This arrangement allows for purification of the sample via the procedure described in Section B, and limited metering of bromine gas into the reaction cell. Normally, an excess of bromine is introduced into the cell, which is then evacuated to the desired pressure before introducing CO<sub>2</sub>. Due to adsorption of Br<sub>2</sub> by the cell walls, a significant amount of time (about one hour) is required to *season* the cell before bromine pressure will stabilize.<sup>(8)</sup> For this reason, the cell is normally left filled with approximately 1.0 torr Br<sub>2</sub> in between lab sessions.

The carbon dioxide sample (Matheson 99.995 %) is stored in a 300 psi lecture bottle. The gas is routed to the system via a 10 psi regulator, ball valve, 1/4" Teflon hose with Swagelok fittings, Nupro needle valve, and finally, a Teflon/glass valve. The Teflon hose is pressurized by opening then closing the ball valve, leaving a reservoir of CO<sub>2</sub> in the hose which is usually adequate for multiple data runs. The CO<sub>2</sub> is precisely metered into the cell by the needle valve, which can provide flow rates from less than 1/10 to hundreds of mtorr/sec. The Teflon valve is used to provide positive cutoff to the CO<sub>2</sub> flow, which leaks through the needle valve at approximately 5 mtorr/min.

The cell is evacuated through a cold trap by a mechanical vacuum pump. A Teflon valve prior to the cold trap closes off the system from the pump during experiments. The cold trap, immersed in liquid nitrogen to freeze out contaminants before they enter the pump and/or the room air, is removed from the system and taken to a vapor hood to thaw after use. With the pump alone, the system can be evacuated to

about 10 mtorr; with the cold trap in place, vacuum improves to 6 mtorr, due to the effect of cryo-pumping. This degree of vacuum is adequate for the experiment, so no additional evacuation method is required. After pumping for several hours to minimize the effects of outgassing, the system leak rate is about 1 mtorr/min, again acceptable for this experiment.

### *3. Photolysis*

The  $\text{Br}_2$  is photolyzed by the beam of a Spectra-Physics Model 164 Argon-Ion ( $\text{Ar}^+$ ) laser operating continuously at 1.5 W, and tuned to the 488 nm line. The beam is introduced into the reaction cell using a high-power turning mirror and two Newport Model 10BR08 Bk7 prisms. The prisms are adjusted so that the beam passes through the cavity at a slight angle to the lasing axis; a single pass is used rather than the originally proposed double pass so that maximum overlap with the axis is achieved while avoiding the cavity mirrors. Routing the pump beam out of the cavity allows monitoring both incident and transmitted power. Using a Coherent Model 210 power meter to measure losses with the cell empty leads to power transmission coefficients of about 0.61 for each prism / window pair. Thus, the estimated pump intensity inside the cell is  $100 \pm 10$  W/cm<sup>2</sup>.

The  $\text{Ar}^+$  laser beam is chopped by a Stanford Research Systems model SR540 chopper, at a nominal rate of 210 Hz for most experiments, so that side-fluorescence and lasing signals can be sensitively detected using lock-in amplification. The chopper controller provides a square-wave synchronizing output and a DC external control input.

### *4. Detection*

The detection systems described here are used to continuously monitor cell pressure, incident and transmitted laser power, and side-fluorescence emissions. Data from all sensors is collected by a central recording device described in the following section.

Total cell pressure is measured by an MKS model 690A 11TRA heated capacitive manometer head (Baratron), with a range of 0-10 torr. The Baratron is controlled by an MKS model 270C-4 signal conditioner, which provides a DC output proportional to the measured pressure. A glass/Teflon valve is used to isolate the Baratron head from the system when large pressure transients are expected. This helps avoid damage and/or loss of calibration.

Ar<sup>+</sup> pump laser power is tracked by two Hamamatsu model S2281 silicon photodiodes attached to Oriel fiber optic cables. In each case, signal is attenuated by a neutral density filter so that the detector operates in a linear response range. One detector is positioned so that it measures light scattered off of the chopper wheel, in order to track incident laser power. The other detector is positioned to measure light scattered off of a graphite beam-block placed after the exit prism, in order to measure transmitted laser power. The detectors produce an uncalibrated DC output proportional to the power of the detected radiation.

Infrared side-fluorescence is measured by a Judson model J10D-M204-R02M-60 photovoltaic InSb detector and model PA-9-50 preamplifier combination. The detector is mounted in a vacuum dewar and cooled by liquid nitrogen to 77 K. A sapphire window in the dewar transmits IR radiation to the detector element, which has an active area diameter of 2 mm, is sensitive in a 1-5  $\mu\text{m}$  range, and produces a current proportional to incident irradiance. The preamp provides two stages of amplification, the first with a gain of  $10^5$  V/A, and the second with a gain of 10 V/V; each of which has a user-accessible AC voltage output. A plastic cover mounted over the detector window is modified to hold a small bandpass filter in place. Two Optical Coating Laboratories interference filters are used: one with a specified 2.71  $\mu\text{m}$  peak and 0.03  $\mu\text{m}$  FWHM, for Br\* emissions, and the other with a specified 4.32  $\mu\text{m}$  peak and 0.28  $\mu\text{m}$  FWHM, for

CO<sub>2</sub><sup>†</sup> emissions. The transmittance profiles for these filters were verified using a Bomem Michelson Interferometer Fourier Spectrometer, and are depicted in Figures 3-2 and 3-3.

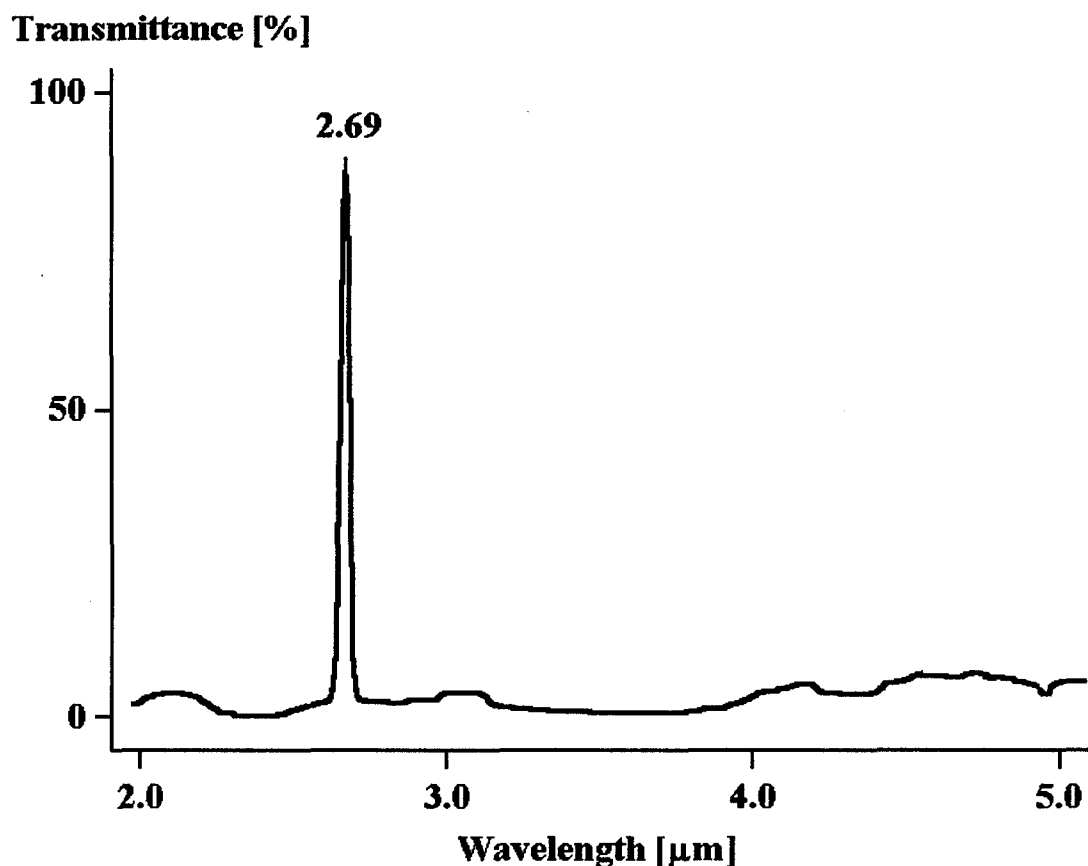


Figure 3-2. Plot of percent transmitted intensity vs. wavelength in  $\mu\text{m}$  for 2.71  $\mu\text{m}$  IR narrow bandpass filter. Note FWHM of 0.03  $\mu\text{m}$  and lack of transmission in region of 4.3  $\mu\text{m}$  CO<sub>2</sub><sup>†</sup> emission. Depicted 0.02  $\mu\text{m}$  shift in peak transmittance is due to spectrometer calibration error.

The detector assembly is mounted on a translation stage, which is adjusted to place the plastic window cover in direct contact with the CaF<sub>2</sub> observation window on the reaction cell, so that the detector element is as close as possible to the IR source. This arrangement proved quite suitable for the detection of the strong CO<sub>2</sub><sup>†</sup> emission, producing signals in the 1-5 mV range with large SNR; thus, no collecting/focusing

lenses were necessary. This setup was also adequate to detect the much weaker  $\text{Br}^*$  emission, but SNR was poor due to the relatively very low signal amplitude of 5-10  $\mu\text{V}$ . Some improvement might be expected in this case with the use of lenses -- Tate reported signal strengths of 15-20  $\mu\text{V}$ , albeit with a wider-bandpass filter. <sup>(28)</sup>

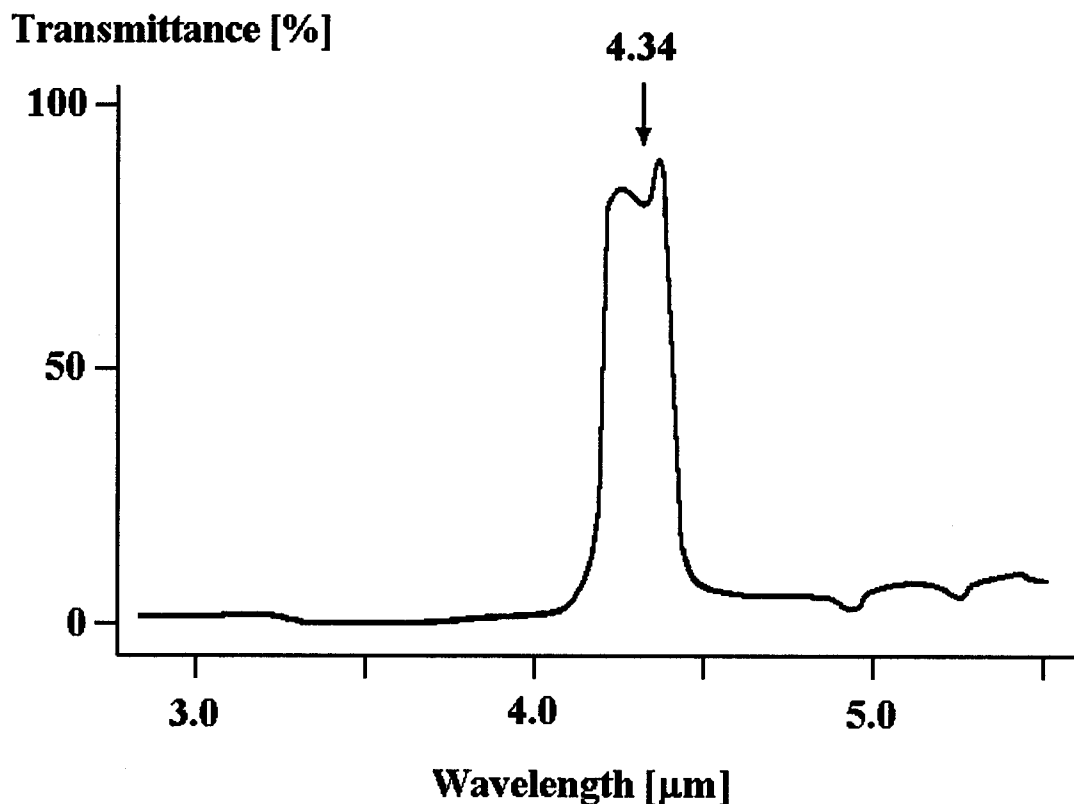


Figure 3-3. Plot of percent transmitted intensity vs. wavelength in  $\mu\text{m}$  for 4.32  $\mu\text{m}$  IR bandpass filter. Note 0.28  $\mu\text{m}$  FWHM, depression right-of-center. Depicted shift in center of passband (to 4.30  $\mu\text{m}$ ) is due to spectrometer calibration error.

Before the InSb detector became available, it was necessary to use another type of IR detector in the side-fluorescence experiments. A Kolmar model KV103-0.1-A-2-2SMA(.2) photoconductive HgCdTe (MCT) detector and model KA100-A1(AC)

matched preamplifier were used, producing an AC voltage output proportional to signal irradiance. Like the InSb detector, the detector element is enclosed in a vacuum dewar and cooled by liquid nitrogen, with an external filter fitted over the detector window. However, this element is designed to operate in the 6-12  $\mu\text{m}$  region, with peak responsivity at 10.6  $\mu\text{m}$ , and is optimized for response time rather than sensitivity, with an active region of only 0.2 mm square. Thus, typical 4.3  $\mu\text{m}$  signal amplitudes were far lower -- on the order of tenths of a  $\mu\text{V}$  -- than those achieved with the InSb system, resulting in much lower SNRs for the data collected with the HgCdTe system.

### *5. Data Collection and Reduction*

All data is collected and stored by a Stanford Research Systems model SR850 digital signal processing lock-in amplifier. In addition to the basic function of phase-sensitive detection (PSD) and amplification of a modulated input signal, this unit provides four auxiliary analog inputs, four auxiliary analog outputs, a CRT graphic display, a trace memory, mathematical functions, and a built-in 3.5" floppy disk drive. The system is capable of monitoring up to seven external devices, controlling up to four external devices, and recording, analyzing, and saving data from up to four sources.

The output from the detector preamp is connected directly to input A of the SR850, the PSD input, which is set to AC coupling, floating ground, both line filters activated. The low pass filter is set to four stages (24 dB/octave), and the time constant is set to either 300 msec or 1 sec, depending on the sample rate used. Sample rate varies from 1/8 Hz to 16 Hz as needed, but is typically 1/4 Hz for a 15 minute run. The sensitivity setting depends on the detector; 1  $\mu\text{V}$  is used for the HgCdTe and 5 mV is used for the InSb. The chopper synch output is connected to the external synch input of the SR850, which is set for external reference, positive-edge triggering. The external control input of the chopper controller is connected to the OUT1 auxiliary output of the SR850. This gives the lock-in amp remote control of the chop frequency, allowing a

synchronized sweep of frequency vs. time. Pins 1 and 8 of the Baratron signal conditioner's remote interface connector provide a DC cell-pressure signal to the AUX1 input of the SR850. The Hamamatsu Si detectors are each connected to a separate SRS model SR830 DSP lock-in amp, which is similar to the SR850, but lacks the display and recording capabilities. These amplifiers are necessary to convert the modulated Ar<sup>+</sup> laser power signals back to DC so that they can be recorded by the SR850. The channel 1 output of each SR830 is connected to an auxiliary input on the SR850; AUX2 records the incident Ar<sup>+</sup> laser power signal, and AUX3 records the transmitted Ar<sup>+</sup> laser power signal.

During a timed data run, the SR850 samples data at the preset rate, and stores it in memory as a *trace*. There are four user-defined traces, each of which can be programmed to store raw data from the various inputs, or processed data, such as the results of simple real-time computations. Normally, amplified detector, cell pressure, incident laser power, and transmitted-to-incident power ratio ( $I_t/I_i = \text{AUX3}/\text{AUX2}$ ) signals are recorded. For some experiments, chop frequency is recorded in place of incident laser power. The  $I_t/I_i$  ratio is used in place of  $I_i$  alone to compensate for any drift in the laser's output. Due to the lack of calibration of the power signals, this ratio is proportional to but not identical to the overall transmittance of the cell. However, the actual transmittance of the cell's *contents* can be determined by normalizing  $I_t/I_i$  to the empty-cell value  $(I_t/I_i)_0$ . Stored traces are saved to disk in both ASCII format, and as SR850-specific trace files. ASCII data files are transferred to a personal computer, and imported by Microsoft Excel. <sup>(5)</sup> This software and Jandel Scientific's TableCurve 2D <sup>(27)</sup> are used to format, analyze, and present the data.



## *B. Experimental Procedures*

This section explains in detail the experiments which were performed in this research. It begins with a description of the bromine sample purification process. While most other routine procedures (ie those which are considered part of the set-up, and yield no experimental data) are explained in the apparatus section, the exact process used to prepare the  $\text{Br}_2$  is considered important, as it may have some bearing on the experimental results. The next two experiments, measurement of the absorption coefficient of  $\text{Br}_2$  and the collision-free quenching coefficient  $k_0$  were intended both as *confidence-builders*, and to obtain needed background data for analysis of subsequent experiments. The final three experiments, quenching, long-term steady-state behavior, and response to chopping frequency of  $\text{CO}_2^+$  fluorescence, all have bearing on the construction of a CW E $\rightarrow$ V laser device. As mentioned in the introduction to this chapter, this line of investigation was pursued in lieu of an attempt at lasing, due to time limitations, and because preliminary results indicated that a better understanding of the fundamentals should be achieved before proceeding.

### *1. $\text{Br}_2$ Sample Preparation*

The most likely contaminants present in any significant concentration in the  $\text{Br}_2$  sample are the atmospheric constituents nitrogen, oxygen, carbon dioxide, and water. The first three have freezing points well below that of molecular bromine, while the last has a freezing point well above bromine's, in addition to a lower vapor pressure. It is thus possible to remove these contaminants by a repeated freeze/thaw and evacuation process.

The sample is first loaded into one arm of the distillation apparatus, in enough quantity to last throughout the research (several milliliters). The sample is frozen by immersing the arm in liquid nitrogen, after which it is exposed to the vacuum of the reaction cell and allowed to warm. As the sample thaws, the unwanted gases boil off, increasing the pressure in the cell. As the bromine warms further, its vapor pressure

causes a sharp increase in the cell pressure, at which point the distillation section is closed off from the vacuum. Now the empty arm is immersed in liquid nitrogen, creating a cryo-pump that condenses bromine vapor into that arm, while refreezing the bromine in the first arm. The first arm is closed off, allowing the sample to thaw, then reopened, allowing more bromine vapor to condense into the second arm. This process is repeated until the majority of the original sample has been distilled into the second arm. Now the second arm is closed off, and the first arm opened to the cell, so that the remaining sample, including any water contamination, is drawn off to vacuum. This entire distillation process is repeated several times to ensure complete purification of the sample. <sup>(19)</sup>

## *2. 488 nm Absorption*

The absorption experiment was intended to serve two purposes. The first was to measure the absorption coefficient of  $\text{Br}_2$ , as a confidence-check of the system and the theory, and to provide information for later analysis. The second purpose was to calibrate the Si detectors and lock-in amps for direct measurement of  $\text{Br}_2$  pressure in the cell.

In all experiments, the  $\text{Ar}^+$  laser beam was blocked between the chopper and first Brewster window while setting up for each data run. This procedure ensures positive control of the start of photolysis, while still allowing the incident laser power to be monitored for stability. The cell was completely evacuated, then filled with 5.0 torr of bromine and allowed to stabilize in pressure. Next, the laser was unblocked, and the data run started. The vacuum valve was opened slightly and adjusted for a gradual evacuation of the molecular bromine, timed so that complete evacuation occurred near the end of the 15 minute run. During the run,  $I_t/I_i$  and total cell pressure were recorded at 4 sec intervals. Two data runs were recorded to assess consistency.

### 3. *CO<sub>2</sub> Quenching of Br\**

In previous AFIT work, Tate attempted to measure the quenching of Br\* by CO<sub>2</sub> via a method similar to that described here. <sup>(28)</sup> Johnson later showed that the interference filter Tate used failed to properly isolate the 2.71  $\mu\text{m}$  Br\* emission, resulting in flawed data. <sup>(11)</sup> Johnson went on to use both pulsed and steady-state photolysis studies to measure  $k_{\text{Br}_2}$  and  $k_{\text{CO}_2}$ , and determine  $k_0$  for his apparatus. This experiment employs steady-state photolysis to observe CO<sub>2</sub> quenching of Br\*, not for the purpose of measuring  $k_{\text{CO}_2}$ , which has been well established previously, but to determine  $k_0$  for this system, which is used in subsequent analysis.

For this and all other side-fluorescence experiments performed, the cavity mirrors were blocked to eliminate the possibility of stimulated emission affecting results. The InSb detector was used with the 2.71  $\mu\text{m}$  filter installed. The cell was evacuated, then filled to 1.00 torr, and allowed to stabilize. Data was collected for 30 sec with the laser blocked, allowing baselines for pressure and detector noise/background signal to be established. Next, the laser was unblocked, and a baseline Br\* signal was recorded for 30 seconds. At 60 sec, CO<sub>2</sub> flow was initiated at a rate of about 4 mtorr/sec. Total cell pressure and InSb detector signal were sampled at 1/4 Hz for 10 minutes, during which CO<sub>2</sub> pressure reached 2.2 torr. A second run was accomplished, this time increasing the CO<sub>2</sub> flow rate after the first 500 mtorr, yielding a final CO<sub>2</sub> pressure of 7.7 torr.

### 4. *CO<sub>2</sub> Quenching of CO<sub>2</sub><sup>†</sup>*

As pointed out by Johnson, Tate's Br\*-CO<sub>2</sub> quenching experiment was flawed in that the filter used also allowed the transmission of 4.3  $\mu\text{m}$  CO<sub>2</sub><sup>†</sup> emissions. What was actually seen included the effects of CO<sub>2</sub><sup>†</sup> quenching by CO<sub>2</sub>, which is why Tate was unable to model the data. <sup>(28)</sup> In light of this realization, it was desired to revisit Tate's experiment (with a better filter) to see if the results could be recreated, and if so, whether an improved model could be found to explain them.

The 4.3  $\mu\text{m}$  filter was installed on the HgCdTe detector, allowing isolation of the  $\text{CO}_2^+$  signal. The laser was blocked and the cell evacuated, then filled to the desired bromine pressure and allowed to stabilize.  $\text{Br}_2$  pressures of 500, 750, 1000, 1250, and 1500 mtorr were tested. 10 minute runs were conducted as described above, during which  $\text{CO}_2$  was added to the cell at a rate of 1-2 mtorr/sec, achieving final  $\text{CO}_2$  pressures of 750-1000 mtorr. More runs were conducted, this time increasing the  $\text{CO}_2$  flow after 250 mtorr, so that final pressures of 2.5-3.0 torr were reached. When the InSb detector became available, additional runs at 1000 mtorr  $\text{Br}_2$  were conducted for comparison, and to provide cleaner data for analysis.

### 5. Steady-State Signal Decay

Pressure-domain plots of  $\text{CO}_2^+$ - $\text{CO}_2$  quenching data indicated something unexplained was occurring. Since  $\text{CO}_2^+$  data had originally been recorded in the time-domain, it was desired to find out whether some underlying temporal phenomenon might be distorting results. A series of experiments was performed, beginning with a look at the long-term behavior of the side-fluorescence under static conditions. This, too, yielded an unexpected result -- a decay in the signal over time. Subsequent experiments constituted a sort of *detective game*, wherein several possible mechanisms for the decay were explored. The following is a description of procedures only; the rationale and results are held until the next chapter.

For most of the experiments in this series, a standard fill of 1000 mtorr of  $\text{Br}_2$  and 100 mtorr of  $\text{CO}_2$  was used to enable direct comparison of results. Exceptions to this rule are specified. The majority of tests were conducted with the InSb detector in place, so data was of high quality. Data recorded for each run included IR detector signal, total cell pressure, incident  $\text{Ar}^+$  laser power, and the transmitted-to-incident power ratio. Each run started with blocking the laser, and evacuating the cell for several minutes until below 10 mtorr. 5-10 torr of bromine was introduced into the cell from the distillation section, then

then the valve tightly closed. The cell was immediately pumped down to about 200 mtorr above the desired pressure, then allowed to stabilize for several minutes. This always resulted in a reduction in total pressure as bromine adsorbed to the walls to replace that lost during evacuation. Once stabilized, the bromine pressure was adjusted down to the desired value by opening the vacuum valve slightly. Following the above procedure yielded pressure stability (without photolysis) of better than 1 mtorr/min, on average. Next, CO<sub>2</sub> was introduced into the cell (if required) in the desired quantity, and the positive-shutoff valve tightly closed. Before photolysis and data collection were begun, a five minute gas-mixing period was allowed. This step eliminated the signal delays and transients upon initiation of photolysis that were initially observed in these experiments, and led to very consistent results.

After the above procedures were accomplished, data collection was initiated following several different profiles. The laser was unblocked either immediately, after a specified delay, or according to an on-off-on-off pattern. Several examples of each profile were recorded with the 4.3  $\mu\text{m}$  filter in place. The first profile was also followed with the 2.7  $\mu\text{m}$  filter in place, with and without CO<sub>2</sub> added to the bromine. Different mixtures of Br<sub>2</sub> and CO<sub>2</sub> were tried. One series looked at a constant Br<sub>2</sub> pressure of 1000 mtorr with very small amounts of CO<sub>2</sub> added (0, 1, 5, and 10 mtorr); another series looked at a variety of mix ratios, with all combinations of Br<sub>2</sub> at 500/1000/2000 mtorr and CO<sub>2</sub> at 50/100/200 mtorr examined. Data runs ranged from 10 to 60 minutes long, with sampling rates of from 1/2 Hz to 1/16 Hz, where slower rates were used for longer runs to keep the number of data points manageable.

#### *6. Chopping Frequency Dependence*

In order to employ phase-sensitive detection techniques, the detector signal must be modulated at a known frequency. Additionally, many detector/preamplifier sets are AC-coupled (such as the HgCdTe system), and likewise require a modulated signal. In

this experiment, there are two ways the chopper can be used to provide the necessary signal modulation.

The first way is to insert the chopper wheel between the  $\text{CaF}_2$  window and the detector, so that only the side-fluorescence signal is chopped. This has the advantage of allowing continuous photolytic pumping of the reaction cell, as in a CW laser device, yielding the most realistic view of the applicable kinetics. A disadvantage of such an arrangement is that it places the chopper directly in front of the detector window, creating a wide field of view for the chopped signal. This greatly increases the IR background, leading to a reduced signal-to-noise ratio and greater sensitivity to changes in ambient conditions. This effect can be minimized somewhat by the use of shielding, but in the case of this apparatus, a greater difficulty exists. Because the detector window must be placed directly against the  $\text{CaF}_2$  window (in the absence of a lens system), there is no room to insert the chopper wheel between them.

The second way the chopper can be used to provide the necessary signal modulation is to insert it in the path of the pump laser beam. This method, used here of a necessity, was also employed by previous AFIT workers in steady-state experiments. <sup>(11, 28)</sup> Besides the advantage of minimizing background noise by creating an *inherently* modulated side-fluorescence signal, this approach also allows great flexibility in the positioning of the chopper (anywhere along the pump beam). However, the disadvantage is that the intermittent photolysis no longer exactly models a CW system. It had been assumed that this detail posed no great problems, in that the kinetic processes under investigation occur on such short time scales that a chop rate on the order of hundreds of hertz should be equivalent to continuous pumping, albeit with a 50% reduction in average power. It was desired to test this assumption, in order to assess the applicability of experimental data collected with a modulated pump beam to the construction of a CW laser device.

Five-minute data runs were conducted, with a 1/4 Hz sample rate and 300 ms time constant, wherein the SR850 lock-in amp was programmed to provide a linear voltage sweep at OUT1, thus varying the chopper frequency from 20 Hz - 3000 Hz during the course of a scan. The short scan time was chosen both to save wear on the chopper motor, which should spend limited time operating above 2000 Hz, and to minimize the effects of steady-state signal decay. To further compensate for signal decay, scans were conducted with both increasing and decreasing chopper frequency. The cell was prepared with a standard 1000/100 mtorr Br<sub>2</sub>/CO<sub>2</sub> fill, the laser unblocked, and the run started. Detector signal and external reference (chop) frequency were recorded. Both IR detectors were used, and each detector was tested under illumination by a constant white-light source (with chopper and filters in place) to ensure flat response characteristics for the detector/preamp/lock-in amp combination across the desired frequency range.

#### IV. Results and Analysis

##### A. 488 nm Absorption

The absorption procedure was intended to provide an experimental value for the absorption cross section  $\sigma_{488}$ , to be used in later analysis, and to calibrate the system for direct measurement of  $\text{Br}_2$  concentration in the cell. While good results were obtained relative to the first objective, the second objective proved harder to meet.

##### 1. Absorption Cross Section

The ratio of transmitted-to-incident laser power ( $I_t/I_i$ ) was recorded for bromine pressures up to 5.0 torr. Two data runs were accomplished, yielding graphs of the exponential form shown in Figure 4-1 below, where  $I_t/I_i$  figures have been normalized to the starting (empty-cell) value  $(I_t/I_i)_0$ .

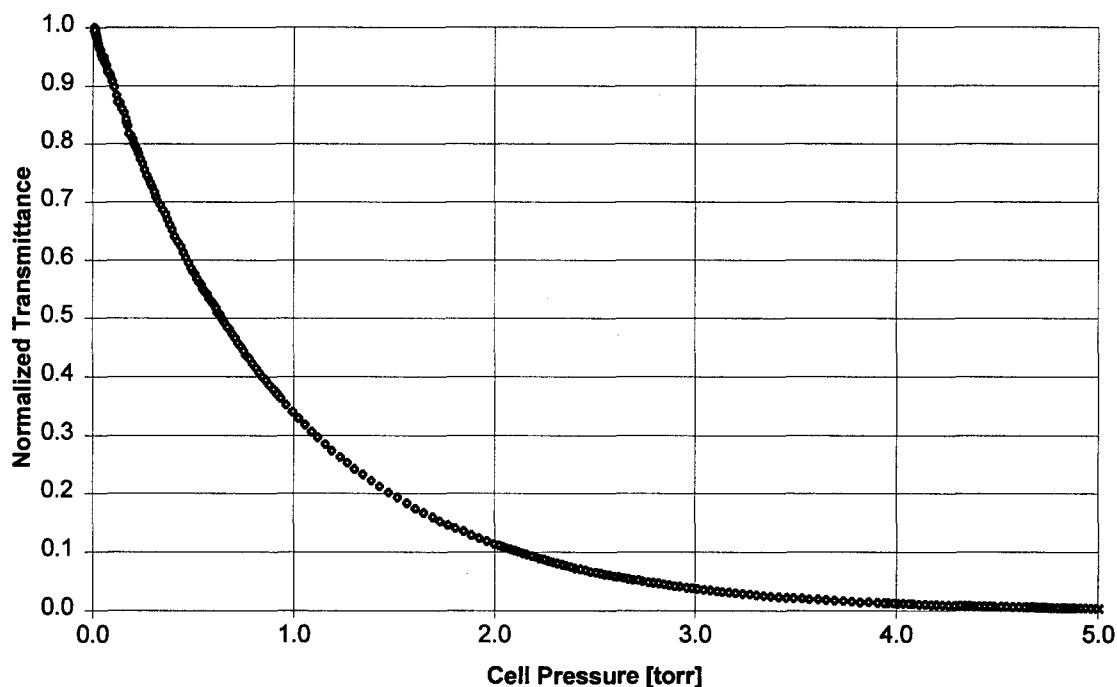


Figure 4-1. Graph of normalized transmittance  $(I_t/I_i)/(I_t/I_i)_0$  vs.  $\text{Br}_2$  pressure for 488 nm radiation.



Taking the natural logarithm of both sides of Equation (2-10) yields

$$\lambda \nu \left( \frac{I}{I_0} \right) = -\sigma N l \quad (4-1)$$

This is a function of the linear form

$$y = mx + b$$

where

$$y = \ln(I/I_0) \text{ [dimensionless]}$$

$$m = -\sigma l \text{ [cm}^2\text{]} \quad \text{[cm}^2\text{]}$$

$$x = N \text{ [molec cm}^{-3}\text{]}$$

and

$$I = I_t / I_i$$

$$I_0 = (I_t / I_i)_0$$

The proportionality constant between concentration  $N$  and pressure  $p$  is  $3.33 \times 10^{16} \text{ molec cm}^{-1} \text{ torr}^{-1}$  at 290 K. Factoring this constant into  $m$  allows  $-\ln(I/I_0)$  to be plotted versus pressure, as shown in Figure 4-2. The absorption cross section may now be calculated from the slope  $m'$  of this linear fit using

$$\sigma = -\frac{m'}{(3.33 \times 10^{16}) l} \quad (4-2)$$

Substituting a path length of 90 cm and the slopes resulting from the two data runs, Equation (4-2) yields the values for  $\sigma$  listed in Table 4-1 below. Also reported are the average of these values and a comparison value interpolated from a table compiled by Seery and Britton.<sup>(23)</sup> The measured value of  $\sigma_{488}$  agrees with the accepted value to

within experimental error. For the sake of consistency, the experimentally determined value will be used in subsequent calculations.

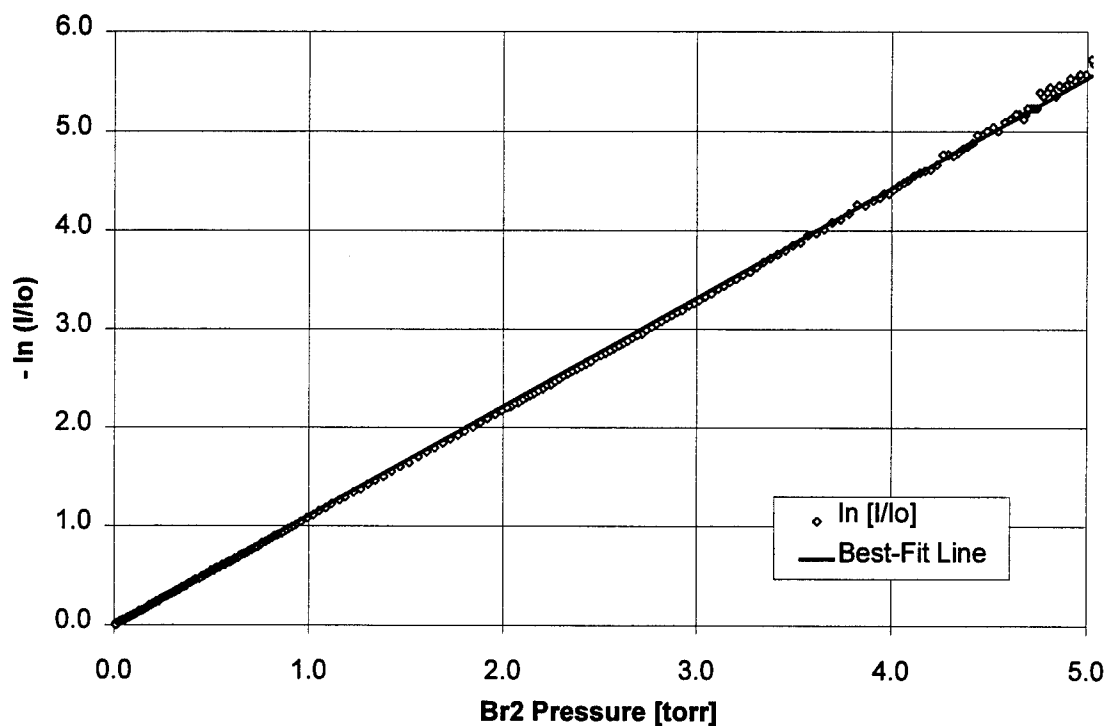


Figure 4-2. Graph of  $-\ln(I/I_0)$  vs.  $\text{Br}_2$  pressure for 488 nm radiation.

Table 4-1.  $\text{Br}_2$  Absorption Cross Section at 488 nm

Data Run	Experimental Value ( $10^{-19} \text{ cm}^2$ )	Previous Value ( $10^{-19} \text{ cm}^2$ )
1	3.69	
2	3.50	
average	$3.60 \pm 0.10$	3.63

## 2. $\text{Br}_2$ Concentration

If the cell is known to contain only pure molecular bromine, the  $\text{Br}_2$  concentration  $[\text{Br}_2]$  can be determined easily from the total cell pressure ( $p_{\text{tot}}$ ), and any change in  $p_{\text{tot}}$  indicates a change in  $[\text{Br}_2]$ . Since the resolution of the pressure-measuring equipment used in this experiment is 1 mtorr, with a noise level of  $\pm 2$  mtorr in the output signal, an absolute detection limit of 2 mtorr exists for changes in cell pressure. This corresponds to detecting a 0.2 % change in  $[\text{Br}_2]$  at the standard 1000 mtorr bromine pressure used in most of the experiments. However, if other gaseous constituents exist in the cell (such as  $\text{CO}_2$ , contaminants, or reaction products), a change in cell pressure does not necessarily indicate a change in  $[\text{Br}_2]$ . Likewise, constant cell pressure does not necessarily indicate constant  $[\text{Br}_2]$ , since a change in the partial pressure of  $\text{Br}_2$  ( $p_{\text{Br}_2}$ ) could be masked by an equal-magnitude change in the partial pressure of another species (or the appearance of a new one), such that  $p_{\text{tot}}$  remains constant. Thus, a direct method for monitoring  $[\text{Br}_2]$  is desired.

One such method, which has the advantage of requiring no additional equipment beyond the cell pressure sensor, involves measuring the pressure change  $\Delta p$  which occurs in the cell upon initiation of photolysis. Under photolysis, the atomic bromine concentration increases until equilibrium between dissociation and recombination processes is achieved. Since two Br atoms replace each  $\text{Br}_2$  molecule dissociated, the fractional pressure increase ( $\Delta p/p_{\text{Br}_2}$ ) corresponds to the fraction of the total  $\text{Br}_2$  in the cell photolyzed, which in turn corresponds (approximately) to the ratio of the volume of the pump laser beam to the total cell volume ( $V_{\text{pump}}/V_{\text{cell}}$ ). If the fixed ratio  $\Delta p/p_{\text{Br}_2}$  is determined, either by estimating  $V_{\text{pump}}/V_{\text{cell}}$  or (better) by taking several calibration measurements at known bromine pressures, a linear plot of  $p_{\text{Br}_2}$  vs.  $\Delta p$  may be constructed, and  $\Delta p$  measurements may be used to monitor  $p_{\text{Br}_2}$ .

The disadvantage of the above method is that poor precision is obtained when  $V_{\text{pump}}/V_{\text{cell}}$  (and thus  $\Delta p/p_{\text{Br}_2}$ ) is small, as is the case for the apparatus used in this work. Assuming  $\Delta p/p_{\text{Br}_2} \approx 2\%$ , an estimate consistent with current observations and with the findings of both Tate and Johnson using similar equipment <sup>(11, 28)</sup>, the known resolution limit of 2 mtorr for  $\Delta p$  measurements leads to a resolution limit of 100 mtorr for  $p_{\text{Br}_2}$ ! This represents a 10 % change in  $[\text{Br}_2]$  at the standard 1000 mtorr bromine pressure, or fifty times the resolution limit available in the earlier case of a cell containing only pure bromine. The low precision offered by the  $\Delta p$  method in the present case requires that a different method be sought for directly monitoring  $[\text{Br}_2]$ .

Another direct method for determining  $\text{Br}_2$  concentration, which has the advantage of being unaffected by the relative volumes of the cavity and pump beam, is to use absorption measurements. The disadvantage of this approach is that additional equipment is required in the experimental setup (as described in Chapter III). Using Equation (2-10), it can be shown that a 2 % change in  $[\text{Br}_2]$  leads to an approximate 2 % change in transmittance of 488 nm light, for a path length of 90 cm and bromine pressure near 1000 mtorr. Since changes in transmittance of less than 1 % are detectable, corresponding to a  $p_{\text{Br}_2}$  resolution limit of less than 10 mtorr, recording the trace of  $I_t/I_i$  during each experiment was expected to yield a much more sensitive record of  $\text{Br}_2$  concentration than the pressure-change method described above.

Unfortunately, this technique could not be successfully employed. Early data runs showed a steady increase in the measured transmittance of the cell during photolysis, indicating a loss of  $\text{Br}_2$  which might account for the loss of steady-state signal described later in this chapter. However, it was found that the increase in measured transmittance over time *always* occurred, with or without active photolysis, and even with the cell evacuated. Since available time did not allow for a thorough diagnosis of this suspected equipment problem, and its effect was significant enough ( $\approx 5\%$  per hour) to obscure any

genuine small increase in transmittance, further attempts to precisely monitor bromine concentration via this method were abandoned. Nevertheless, an upper limit was set for  $\text{Br}_2$  loss, as no greater change in transmittance than 10 % per hour was ever observed.

#### *B. $\text{CO}_2$ Quenching of $\text{Br}^*$*

The  $\text{Br}^*$  quenching experiment was performed to determine the collision-free rate coefficient  $k_0$  for the apparatus, both as a confidence-building test of theoretical expectations, and to provide information needed in later analysis. Nothing unexpected was observed, and a satisfactory value for  $k_0$  was found.

Two data runs were conducted as described in Chapter III, wherein the  $2.71 \mu\text{m}$   $\text{Br}^*$  emission was monitored as  $\text{CO}_2$  was added to the system. Equation (2-24) predicts that  $\text{Br}^*$  emission intensity should fall off essentially as the inverse of  $\text{CO}_2$  pressure, approaching zero as  $[\text{CO}_2]$  continues to increase. Further, the long lifetime of  $\text{Br}^*$  means that a very low emission intensity is to be expected. Both of the preceding effects were observed, as the example in Figure 4-3 shows.

This graph, reflecting a typical result, clearly shows a decay toward zero as more  $\text{CO}_2$  is added. The fact that the  $2.71 \mu\text{m}$  emission is exceedingly weak is evidenced by the very poor signal-to-noise ratio achieved; in fact, the trend toward zero is lost in the noise beyond about 5.0 torr of  $\text{CO}_2$ .

An attempt was made to analyze this data by the method outlined in Chapter II, beginning with fitting a line to a graph of  $I_0/I$ , per Equation (2-25). However, due to the excessive noise in the signal, very large excursions in  $I_0/I$  occur, particularly where data points appear on or near the  $x$ -axis, making a satisfactory and meaningful linear fit very difficult (see Figure 4-4).

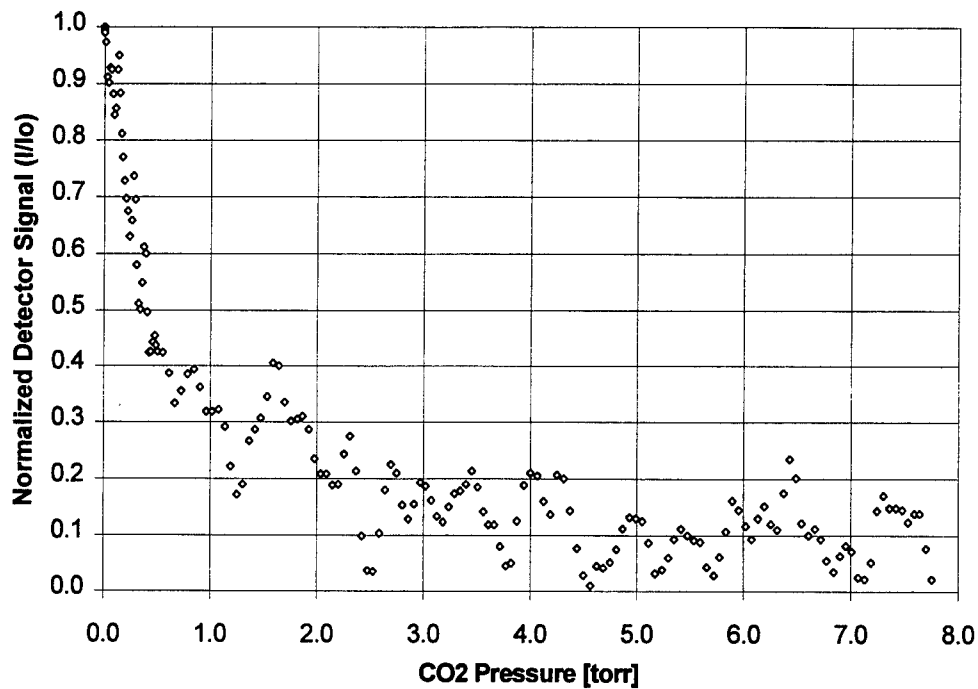


Figure 4-3. Graph of normalized 2.7  $\mu\text{m}$  emission data vs.  $\text{CO}_2$  pressure.

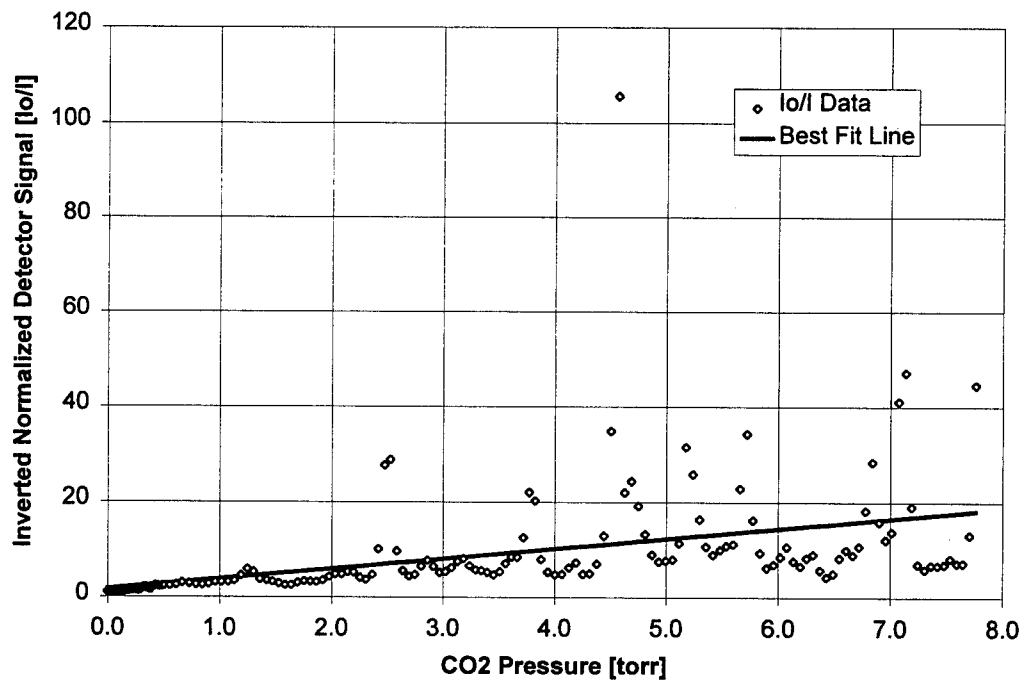


Figure 4-4. Graph of  $I_0/I$  vs.  $\text{CO}_2$  pressure showing large excursions due to excessive noise in the 2.7  $\mu\text{m}$  emission. Best fit line (Equation (2-25)) is depicted, with  $r^2 = 0.21$  using Gaussian errors.

Because the linear fit yielded poor results, an alternative to this standard approach to analyzing the data was selected. Equation (2-25) was inverted, yielding

$$\frac{I_{2.71}}{I_{2.71}^0} = \frac{k_{Br_2}[Br_2] + k_0}{k_{CO_2}[CO_2] + k_{Br_2}[Br_2] + k_0} \quad (4-3)$$

having the form

$$y = \frac{1}{Ax + 1} \quad (4-4)$$

where

$$x = [CO_2]$$

$$y = \frac{I_{2.71}}{I_{2.71}^0}$$

$$A = \frac{k_{CO_2}}{k_{Br_2}[Br_2] + k_0} \quad (4-5)$$

The data of Figure 4-3 were normalized per the left side of Equation (4-3), then Equation (4-4) was fit to the resulting graph using TableCurve2D. The result of this fit, representing a significant improvement over the previous linear fit, is depicted in Figure 4-5. Since  $k_{CO_2}$ ,  $k_{Br_2}$ , and  $[Br_2]$  were known,  $k_0$  could be determined from the best-fit value for A. Applying Equation (4-5), with the best-fit value  $A = 1.97 \pm 0.15$  and the known values <sup>(11)</sup>  $k_{CO_2} = 13.16 \pm 0.245 \times 10^{-12} \text{ cm}^3 \text{ mol}^{-1} \text{ sec}^{-1}$ ,  $k_{Br_2} = 1.24 \pm 0.08 \times 10^{-12} \text{ cm}^3 \text{ mol}^{-1} \text{ sec}^{-1}$ , and  $[Br_2] = 1.00 \text{ torr}$ , yields the value for the collision-free rate coefficient  $k_0 = 1.82 \pm 0.18 \times 10^5 \text{ sec}^{-1}$ . This process was repeated for the first data set, yielding a different value for  $k_0$ . The results of both data runs are presented in Table 4-2.

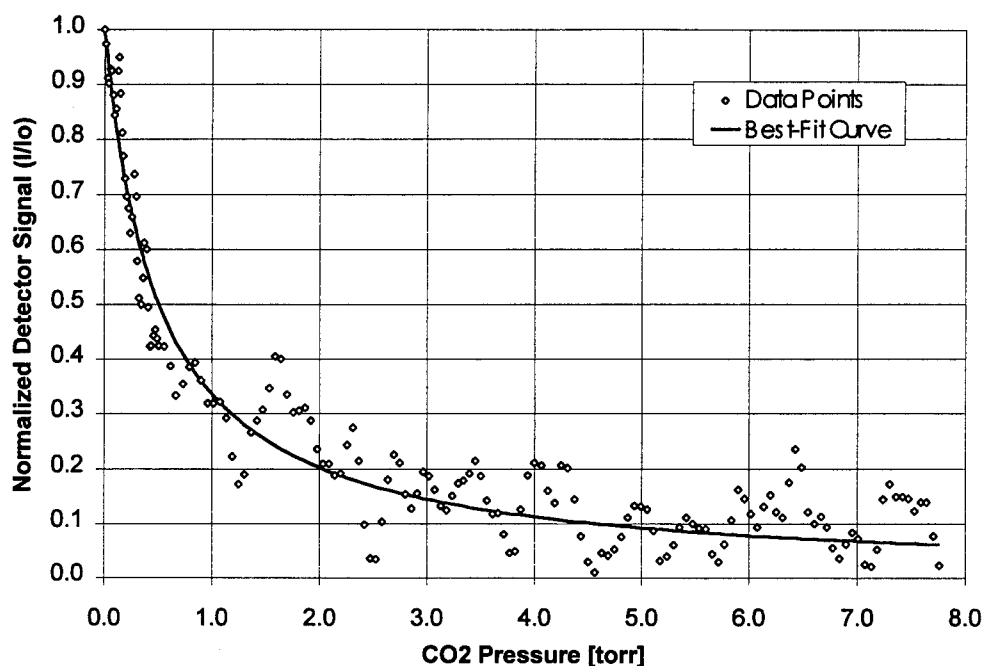


Figure 4-5. Graph of normalized 2.7  $\mu\text{m}$  emission data vs.  $\text{CO}_2$  pressure and best fit of Equation (4-4), with  $r^2 = 0.94$  (cf.  $r^2 = 0.21$  in Figure 4-4).

Table 4-2. Results of Collision-Free Rate Coefficient ( $k_0$ ) Experiment

Data Run	Fit Parameter A	Experimental Value of $k_0$ ( $10^5 \text{ sec}^{-1}$ )
1	$1.97 \pm 0.15$	$1.82 \pm 0.18$
2	$2.28 \pm 0.20$	$1.52 \pm 0.17$
Average		$1.66 \pm 0.23$

The value determined for  $k_0$  was approximately 14 times larger than that found by Johnson for his apparatus <sup>(11)</sup>, but this is not unreasonable considering the different construction of the two systems. Johnson's reaction cell had an inner radius of 3.3 cm, whereas the cell used in this experiment has an inner radius of only 0.48 cm. This difference alone suggests a factor of 7 increase in the wall deactivation rate, according to



Equation (2-15). There are undoubtedly other contributing factors not addressed in the simplified model of Chapter II, such as the greater internal surface area of the current apparatus, but precise identification of these factors is beyond the scope of this work. It is sufficient to note that differences in  $k_0$  are expected between different physical systems, and that a reasonable  $k_0$  has been measured for this apparatus.

### C. $\text{CO}_2$ Quenching of $\text{CO}_2^\dagger$

The  $\text{CO}_2^\dagger$  quenching experiment was intended to recreate Tate's inadvertent observation of steady-state  $\text{CO}_2^\dagger$  quenching, and to test the suitability of the mathematical model proposed in Chapter II toward describing the results. While Tate's results were duplicated, a need was found for further revision of the theoretical kinetic model.

Multiple data runs were conducted following the procedure outlined in Chapter III, wherein the  $4.3\ \mu\text{m}$   $\text{CO}_2^\dagger$  emission was monitored, for several different  $\text{Br}_2$  pressures, as  $\text{CO}_2$  was added to the system. In all cases the shape of the resulting signal-versus-pressure curves very closely matched that reported by Tate. <sup>(28)</sup> A sharp rise in fluorescent intensity was seen as  $\text{CO}_2$  pressure increased to about 100 mtorr, followed by a peak and subsequent decay toward an apparent non-zero limiting value. A displacement of the peak and a slower decay rate were observed as higher bromine pressures were tested. This smoothing effect is apparent in Figure 4-6, which shows the results of two data runs conducted at bromine pressures of 500 and 1000 mtorr.

It was suspected that the smoothing trend depicted in Figure 4-6 resulted from an overall decrease in the  $[\text{CO}_2]/[\text{Br}_2]$  ratio as  $\text{Br}_2$  pressure was increased. To test this assumption, the data for each run were plotted against the  $[\text{CO}_2]/[\text{Br}_2]$  ratio and compared. In all cases this modification resulted in a very close agreement between the shapes of the curves, as illustrated in Figure 4-7. It is thus evident (and not surprising)

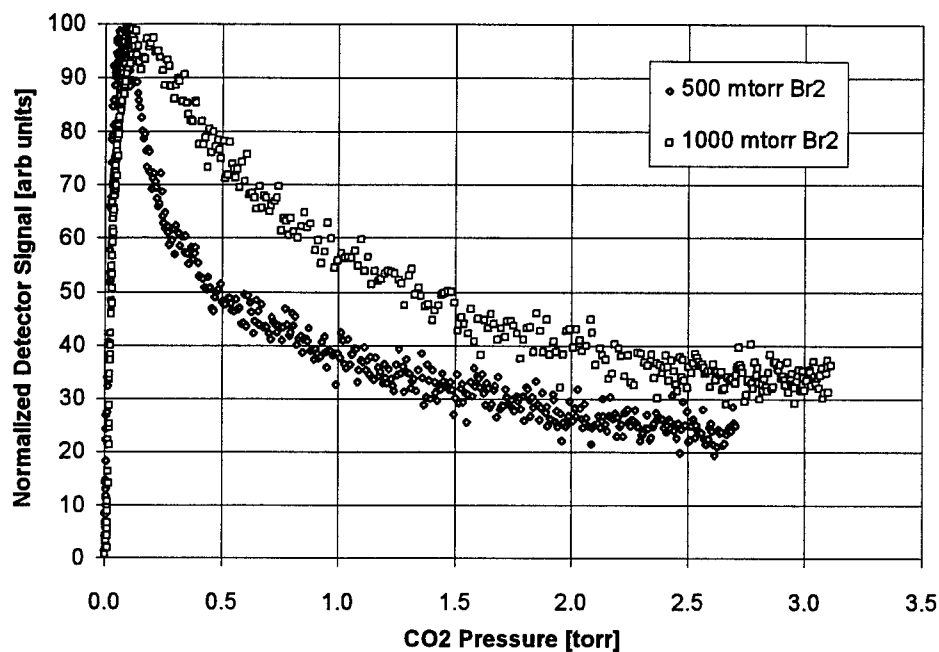


Figure 4-6. Graph of normalized 4.3  $\mu\text{m}$  emission intensity vs. CO<sub>2</sub> pressure for Br<sub>2</sub> pressures of 500 and 1000 mtorr. The HgCdTe detector signal has been normalized to the maximum value for each data series to facilitate comparison of curve shapes. Note the decay toward a non-zero limit.

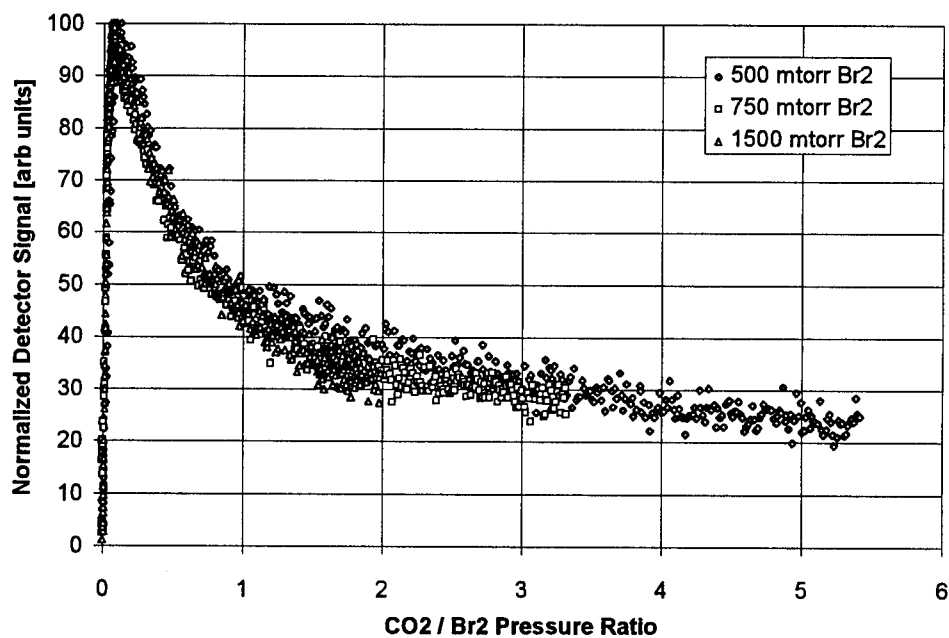


Figure 4-7. Graph of normalized 4.3  $\mu\text{m}$  emission intensity vs. CO<sub>2</sub>/Br<sub>2</sub> pressure ratio for Br<sub>2</sub> pressures of 500, 750, and 1500 mtorr.

that the  $[\text{CO}_2]/[\text{Br}_2]$  ratio determines the degree of  $\text{CO}_2^\dagger$  quenching, rather than the  $\text{CO}_2$  pressure alone. Since this modification amounts only to a rescaling of the pressure-axis, the functional form of the model proposed in Equation (2-35) is not changed, and a fit of Equation (2-36) to the data should still be possible.

In order to isolate the unknowns and simplify the evaluation of the fit results, it is desired to fit Equation (2-35) directly to the experimental data, rather than the generic form of Equation (2-36). This poses no problem, as the curve-fitting software allows complex user-defined functions, incorporating fixed constants and multiple fit parameters. Equation (2-35) includes two rate coefficients for which no established values exist:  $k_{\text{QB}}$  and  $k_0'$ . In addition, the unknown proportionality constant  $K'$  relates the measured emission intensity to the concentration  $[\text{CO}_2^\dagger]$ . These three unknown factors constitute the fit parameters for the model. If a good fit to the data is obtained, wherein the fit parameters assume reasonable values, the form of the model is validated. Before such an assessment can be made, however, expected ranges for the fit parameters  $k_{\text{QB}}$ ,  $k_0'$ , and  $K'$  must be identified.

The rate coefficient for  $\text{Br}_2$  quenching of  $[\text{CO}_2^\dagger]$  is not well-established. However, based on a table of collisional quenching rate coefficients compiled by Tate <sup>(28)</sup>, an expected range of  $1 \times 10^{-16} \leq k_{\text{QB}} \leq 3 \times 10^{-10} \text{ cm}^3 \text{ molec}^{-1} \text{ sec}^{-1}$  (approaching the gas-kinetic limit) seems reasonable. The collision-free deactivation rate of  $[\text{CO}_2^\dagger]$  is known to be much slower than the  $\text{V} \rightarrow \text{V}$  transfer rate ( $k_{\text{VV}}[\text{CO}_2]_{1.0 \text{ torr}} = 4.33 \times 10^6 \text{ sec}^{-1}$  <sup>(6)</sup>), leading to an estimated expected range of  $1 \times 10^2 \leq k_0' \leq 1 \times 10^6 \text{ sec}^{-1}$ . Although an accurate estimate of  $K'$  is not attempted, this scale factor contributes little to the shape of the function, and thus does not impact the overall assessment of the model.

The previously reported values for  $k_{\text{Br}_2}$ ,  $k_{\text{CO}_2}$ , and  $k_0$  are now substituted into Equation (2-35), along with the known values  $k_{\text{EV}} = 5.6 \pm 2.8 \times 10^{-12} \text{ cm}^3 \text{ molec}^{-1} \text{ sec}^{-1}$  <sup>(20)</sup>,  $k_{\text{VV}} = 1.3 \times 10^{-10} \text{ cm}^3 \text{ molec}^{-1} \text{ sec}^{-1}$  <sup>(6)</sup>,  $k_p = 0.697 \text{ cm}^2 \text{ J}^{-1}$  (Equation (2-22)),

and  $I_p = 57 \text{ W cm}^{-2}$  (the laser intensity at the center of the cell for 1.0 torr  $\text{Br}_2$ ), where  $k_p$  and  $I_p$  have been calculated using the measured value of  $\sigma_{488}$ . TableCurve2D is employed to fit this function to an experimental data set, as shown in Figure 4-8, and assign values to the fit parameters.

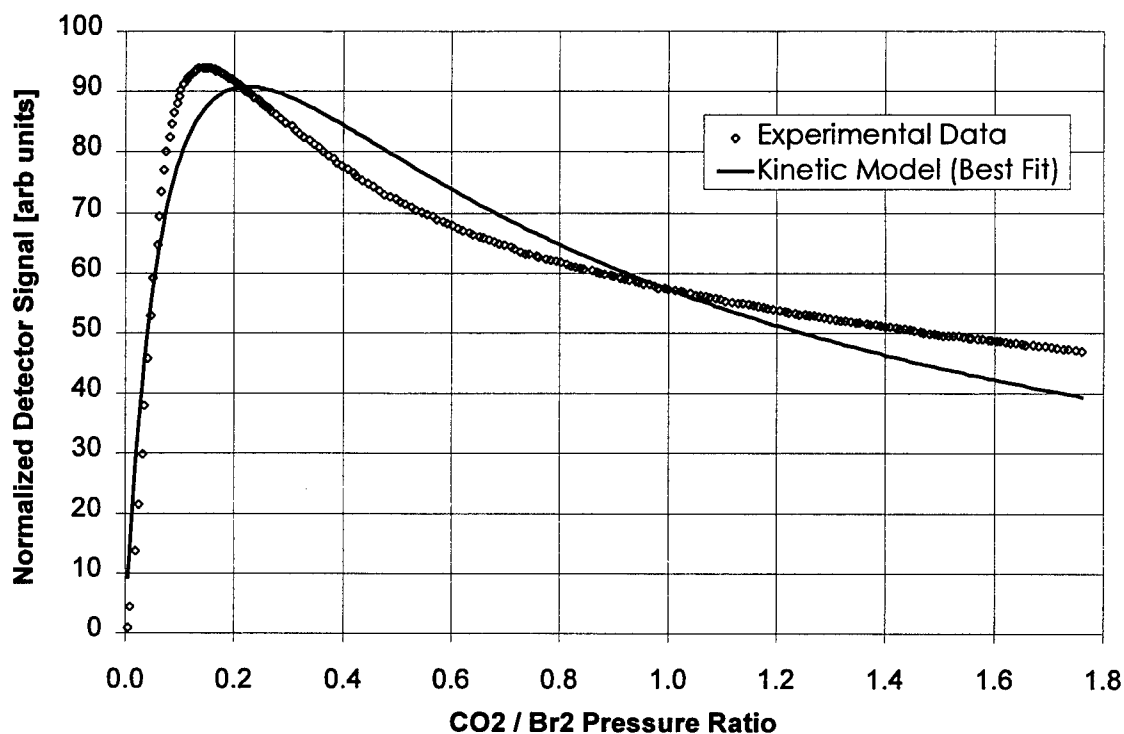


Figure 4-8. Evaluation of kinetic model for  $\text{CO}_2$  quenching of  $\text{CO}_2^+$  at 1000 mtorr  $\text{Br}_2$ . Note the greatly improved SNR attained with the InSb detector.

A qualitative view of Figure 4-8 clearly indicates a discrepancy between the proposed kinetic model and the actual system. Notable differences between the depicted curves are apparent in the shape of the peak and the limiting value as  $\text{CO}_2$  pressure increases. The measured fluorescence rises more quickly and peaks more sharply than predicted by the model. Further, as seen in Figures 4-6, 4-7, and 4-8, the fluorescence

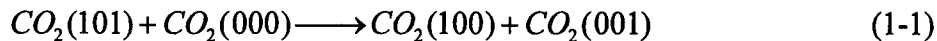
approaches a non-zero limiting value with increasing CO<sub>2</sub> pressure, rather than decaying to zero as the model dictates.

The quantitative view also indicates a problem with the model. The numerical values obtained for the fit parameters are  $K' \approx 2.05 \times 10^{-11}$ ,  $k_{QB} \approx 6.14 \times 10^{-11}$ , and  $k_0' \approx 2100$ . While the latter two fall within the expected ranges established earlier, there is substantial uncertainty in these values. TableCurve2D reports an  $r^2$  coefficient of only 0.90, with standard errors of  $9.98 \times 10^{-6}$  for  $k_{QB}$  and  $3.32 \times 10^{11}$  for  $k_0'$  -- obviously there can be little confidence in the reported nominal values!

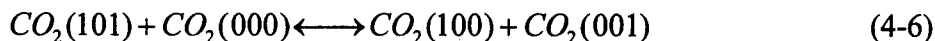
Clearly a revision in the mathematical model is called for. The most obvious problem with the current form is its prediction that CO<sub>2</sub><sup>†</sup> concentration decays to zero as CO<sub>2</sub> is increased, when it is observed that 4.3 μm fluorescence -- and thus [CO<sub>2</sub><sup>†</sup>] -- in fact approaches some non-zero value. However, the model as presently formulated reflects the best current understanding of the significant kinetic processes, as outlined in Equations (2-27) to (2-32). According to this theory, the only significant production channel for CO<sub>2</sub><sup>†</sup> is via E→V transfer from Br\*. Initially, added CO<sub>2</sub> leads to the production of CO<sub>2</sub><sup>†</sup> as Br\* is quenched. When CO<sub>2</sub> concentration is increased beyond a certain level, rapid V→V self-quenching of CO<sub>2</sub><sup>†</sup> becomes dominant, and the steady-state CO<sub>2</sub><sup>†</sup> concentration is reduced. Here a primarily *downward* cascade through lower vibrational energy states is postulated for CO<sub>2</sub>, ultimately resulting in total depletion of CO<sub>2</sub><sup>†</sup> at high CO<sub>2</sub> concentrations. What is lacking in this theory is a mechanism by which the CO<sub>2</sub>(101) state can be populated by some means other than the E→V channel, as is apparently observed in the experiment. The nature of this mechanism must be understood before a mathematical model can be applied.

It has been suggested that if lower vibrational states are sufficiently populated, as is likely the case under continuous V→V quenching of CO<sub>2</sub><sup>†</sup>, it may be possible for a

reverse process to occur wherein these states interact to repopulate the  $\text{CO}_2(101)$  state. <sup>(19)</sup> For example, the reaction



is a known quenching channel for  $\text{CO}_2^\dagger$ . <sup>(6)</sup> Perhaps this can be rewritten



implying a  $V \rightarrow V$  equilibrium exists. The introduction of a reverse reaction, with associated rate-coefficient  $k_{\text{rev}}$ , leads to an additional term in the rate equation (2-33)

$$\frac{d[\text{CO}_2^\dagger]}{dt} = k_{EV} [\text{Br}^*][\text{CO}_2] - k_{VV} [\text{CO}_2^\dagger][\text{CO}_2] - k_0' [\text{CO}_2^\dagger] + k_{\text{rev}} [100][001] \quad (4-7)$$

where  $k_0'$  now includes  $k_{\text{QB}}[\text{Br}_2]$ .

If Equation (1-1) describes the only production channel for (100) and (001), the above modification changes only the effective value of  $k_{VV}$ , leading to no revision in the functional form of Equation (2-36). However, if other production channels for these states are allowed (a reasonable assumption), the form of Equation (2-36) is modified as follows

$$[\text{CO}_2^\dagger] = \frac{A[\text{CO}_2]}{(B[\text{CO}_2] + 1)(C[\text{CO}_2] + 1)} + \frac{D[100][001]}{C[\text{CO}_2] + 1} \quad (4-8)$$

Although the first term in this equation decays toward zero as before, the presence of the second term makes possible the decay of  $[\text{CO}_2^\dagger]$  toward some non-zero value. The behavior of this term in the limit of large  $\text{CO}_2$  concentrations depends on the functional relationship between  $[\text{CO}_2]$  and  $[100]$ ,  $[001]$ , which may involve several intermediate

reactions. While no attempt is made in this work to identify this relationship exactly, for illustrative purposes the simple relation  $[100][001] \propto [\text{CO}_2]$  is assumed. This yields the functional form

$$y = \frac{Ax}{(Bx+1)(Cx+1)} + \frac{Dx}{Cx+1} \quad (4-9)$$

where decay to a constant non-zero value now occurs as  $x$  (representing  $[\text{CO}_2]$  as before) increases. This revised form is fit to the data of Figure 4-8, resulting in the improved fit shown in Figure 4-9.

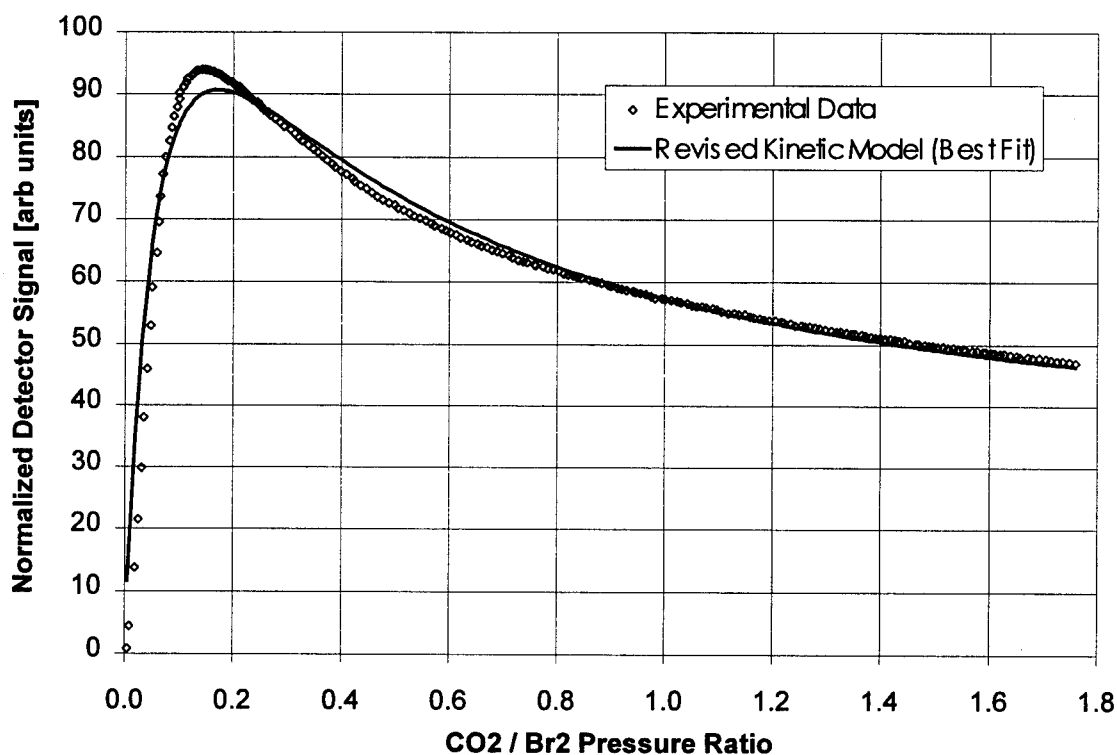


Figure 4-9. Evaluation of revised kinetic model for  $\text{CO}_2$  quenching of  $\text{CO}_2^+$ . Note the improvement over the previous fit, with  $r^2 = 0.96$  in this case, cf.  $r^2 = 0.90$  in the case of Figure 4-8.

Equation (4-9) still represents an imperfect description of  $\text{CO}_2^\dagger$  quenching kinetics, but a clear improvement over Equation (2-36) has been made, suggesting progress in the right direction. It must be emphasized that the revised model of Equations (4-6) to (4-9) is largely speculative, and certainly simplistic. The exact details of the proposed  $\text{V} \rightarrow \text{V} \text{CO}_2^\dagger$  production mechanism, or any other conceivable mechanism, are not addressed.

#### *D. Steady-State Signal Decay*

When the originally proposed kinetic model failed to accurately predict the outcome of the  $\text{CO}_2^\dagger$  quenching experiment, the possibility was considered that some underlying time-dependent reaction was skewing the experimental results. Although quenching data is reported via a graph in the pressure-domain, it is collected in the pressure-time domain, as a continuous slow leak of  $\text{CO}_2$  is employed rather than a series of discrete fixed-pressure measurements. It was thus desired to observe the time-evolution of  $\text{CO}_2^\dagger$  emissions at fixed cell pressures, to see if some long-term change occurs which might affect the shape of the  $[\text{CO}_2^\dagger]$  vs.  $[\text{CO}_2]$  curve.

##### *1. Time-Decay Observations*

In all cases, a time-decay in the steady-state fluorescence, like that depicted in Figure 4-10, was observed, resulting in an average reduction in emission intensity of approximately 10 % after the first ten minutes. This effect was judged not to have a significant impact on the shape of the  $\text{CO}_2^\dagger$  quenching graphs, particularly where higher flow rates are employed, since the initial sharp peaks are recorded in the space of 1-2 minutes, and the total suppression of the signal due to quenching ranges from 50-75 % at the end of a run. Further, adjusting the quenching data for time-decay only *worsens* the agreement with the original theoretical prediction; thus offering no salvation for that model.



Although not significant to the quenching rate studies, the steady-state decay effect could have considerable impact on the construction of a CW laser device if it implies that a continuous decline in output power would be experienced in a similarly closed system. For this reason, an attempt was made to isolate the mechanism responsible for this phenomenon. Several different explanations were proposed, and experiments were devised to test each hypothesis, the details of which are presented below.

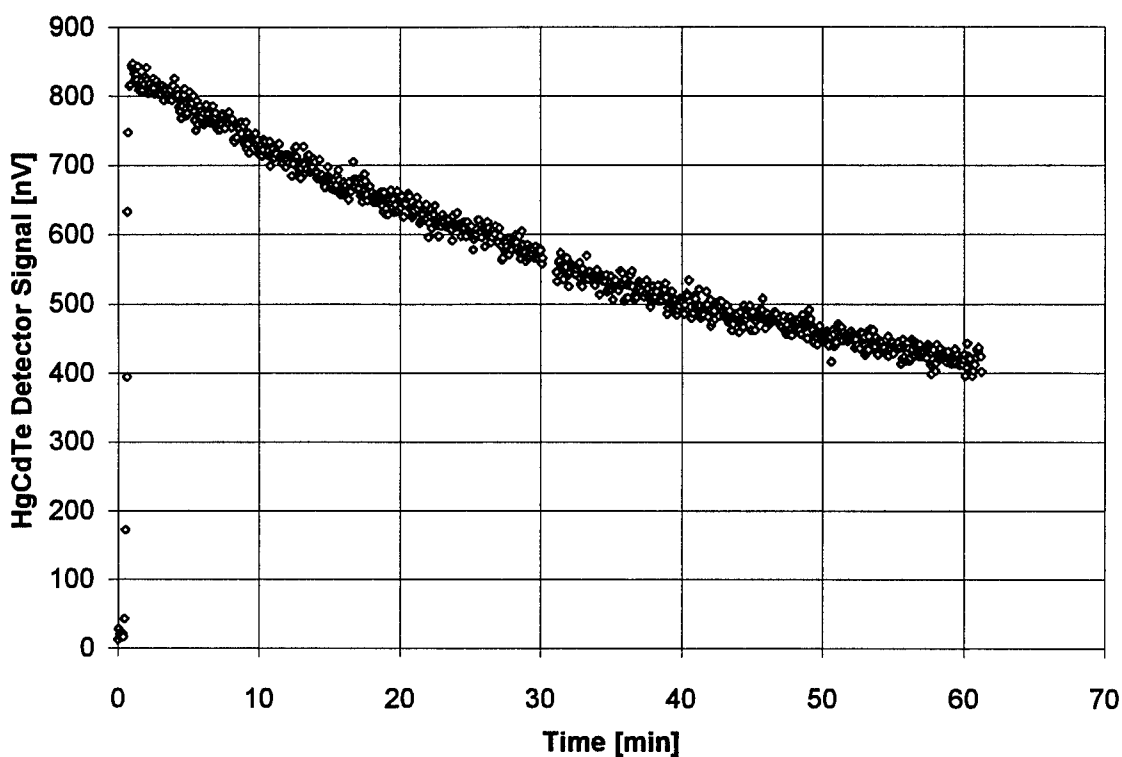


Figure 4-10. Graph of 4.3  $\mu\text{m}$  emission intensity vs. time for a 1000 mtorr  $\text{Br}_2$  and 100 mtorr  $\text{CO}_2$  mixture. Sharp rise in intensity corresponds to unblocking of the photolysis laser. Gap in data is due to 1-min pause in data collection, while photolysis continued.

## 2. Mixing

The first possibility considered was that mixing of the two gaseous constituents was slow, and that signal decreased as mixing became more thorough. Since the cell was

always first filled with bromine, then  $\text{CO}_2$  introduced from one end, it was thought that slow diffusive mixing along the length of the cell might explain the long time-scale of the decay. Some support was given to this notion by the observed lag of 10-20 seconds between the introduction of  $\text{CO}_2$  and the observed rise in  $\text{CO}_2^\dagger$  emissions, as shown in Figure 4-11.

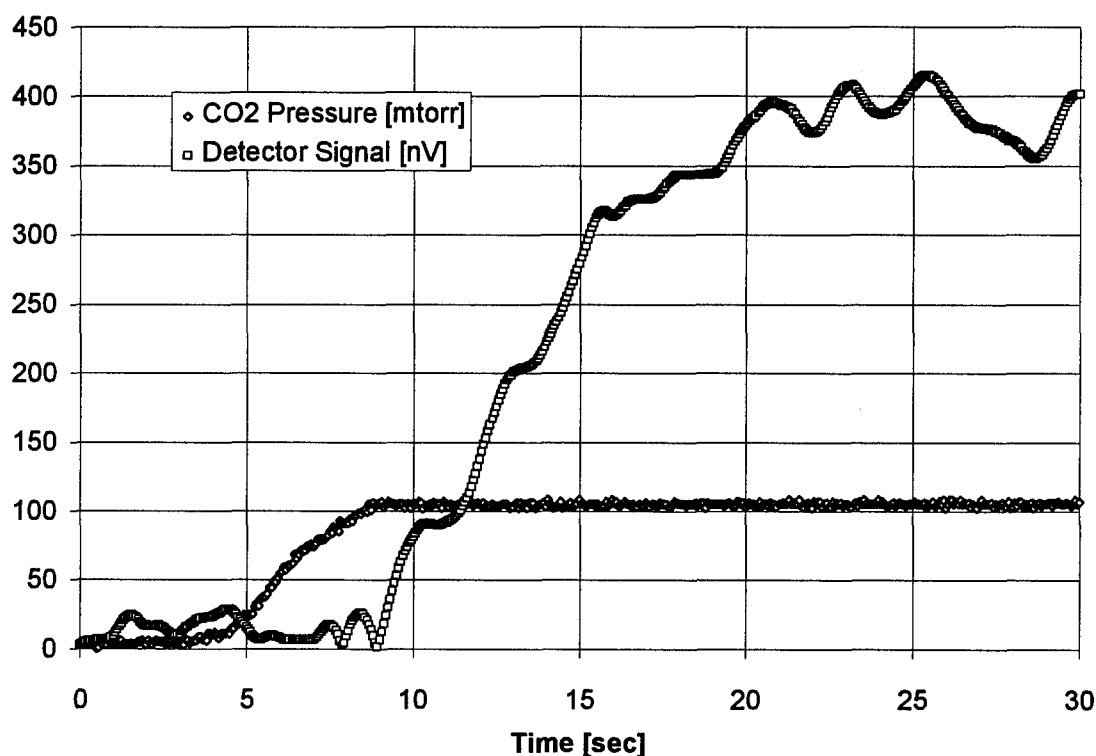


Figure 4-11.  $\text{CO}_2$  pressure and  $4.3 \mu\text{m}$  signal vs. time for mix with 1000 mtorr  $\text{Br}_2$ . Note 10 sec delay between pressure and signal rise, 15 sec between pressure and signal peak.

Clearly there is some diffusive delay before  $\text{CO}_2$  reaches the region of the  $\text{CaF}_2$  viewing window. However, the majority of evidence indicates mixing is complete within less than five minutes, and is not a factor in the long-term signal decay. To begin with, for mixing to reduce the signal intensity, it must be assumed that some very low  $\text{CO}_2$  concentration is optimum, and that any increase in  $\text{CO}_2$  concentration, as with more

less than five minutes, and is not a factor in the long-term signal decay. To begin with, for mixing to reduce the signal intensity, it must be assumed that some very low  $\text{CO}_2$  concentration is optimum, and that any increase in  $\text{CO}_2$  concentration, as with more thorough mixing, leads to reduced fluorescence. This assumption was tested by adding small amounts of  $\text{CO}_2$  to a fixed 1000 mtorr of  $\text{Br}_2$ . As in all the fixed-pressure experiments, five minutes were allowed for the gases to mix before the start of photolysis, as explained in Chapter III. Figure 4-12 shows that higher concentrations of  $\text{CO}_2$  yielded stronger emissions -- clearly each mixture was of less-than-optimum  $\text{CO}_2$  concentration -- yet signal decay was still observed. Only in the case of zero added  $\text{CO}_2$  did the signal rise, and this is attributed to outgassing of  $\text{CO}_2$  from the cell walls.

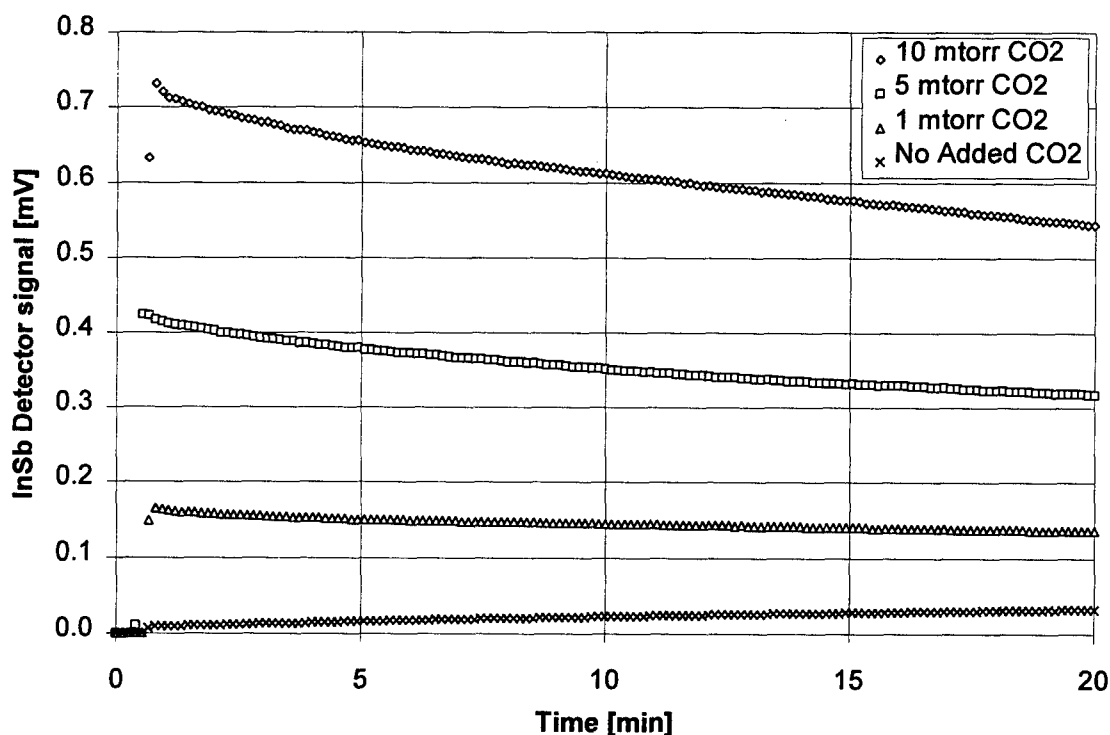


Figure 4-12.  $4.3 \mu\text{m}$  signal vs. time for 1000 mtorr  $\text{Br}_2$  and small concentrations of  $\text{CO}_2$ .

the same rate under photolysis, as illustrated by Figure 4-13. If mixing were responsible for the decay, lower starting intensities would be expected after longer delays. Many data runs of this type were conducted, all of which were consistent with the results reported here.

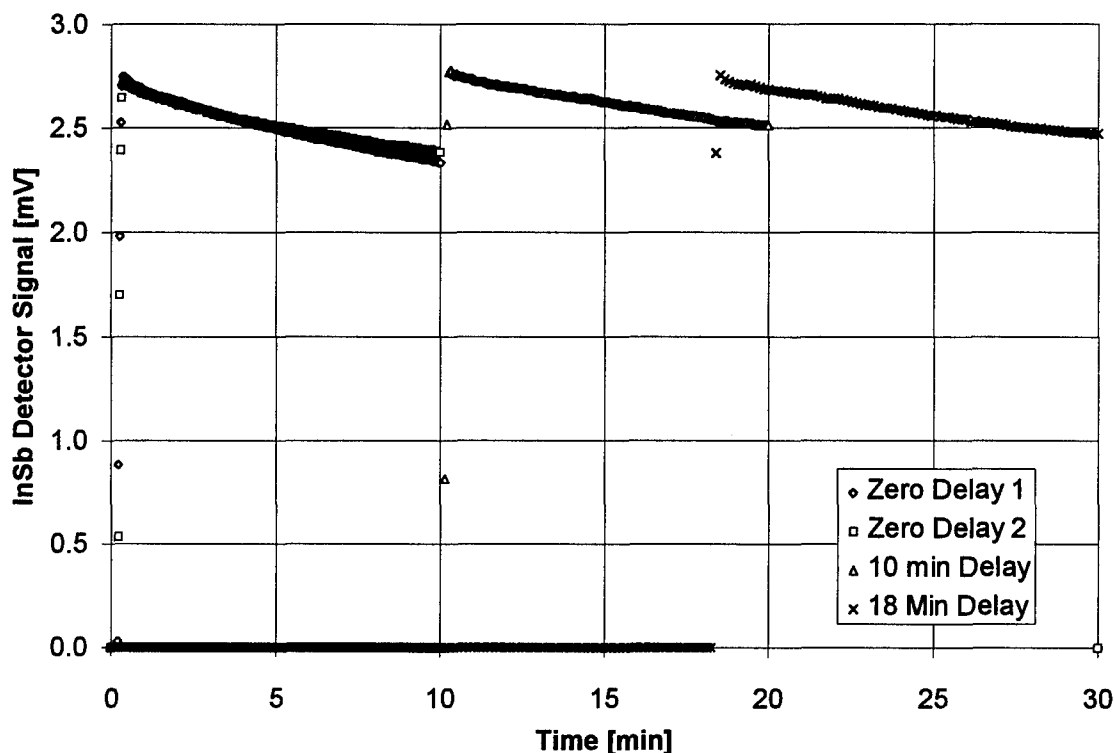


Figure 4-13. 4.3  $\mu\text{m}$  signal vs. time for various delays before initiation of photolysis. Two runs with zero delay are shown to demonstrate consistency. Note that no decay occurs in the absence of photolysis.

### 3. $\text{Br}_2$ Concentration

Now the possibility of changes in molecular bromine concentration is addressed. A change in  $[\text{Br}_2]$  due to leakage, adsorption, slow recombination, chemical reaction, or some other effect could lead to reduced  $\text{Br}^*$  production, and thus reduced  $\text{CO}_2^\dagger$  emissions. But any change large enough to produce the 50 % decrease in signal seen in Figure 4-10 would certainly be detected as a change in total cell pressure or 488 nm transmittance.

some other effect could lead to reduced  $\text{Br}^*$  production, and thus reduced  $\text{CO}_2^+$  emissions. But any change large enough to produce the 50 % decrease in signal seen in Figure 4-10 would certainly be detected as a change in total cell pressure or 488 nm transmittance. Figure 4-14 shows typical pressure and transmitted intensity traces from a delayed-photolysis run as described above. In this case, photolysis was initiated at 19 minutes, at which point the transmitted signal trace begins. Note that the system pressure is quite stable, varying by no more than the noise level of  $\pm 3$  mtorr before the laser is unblocked, indicating no significant leakage, adsorption, or outgassing occurs. With the laser unblocked, the pressure slowly increases to a stable equilibrium about 15 mtorr above the starting pressure, indicating only a 1.5 % average loss of  $\text{Br}_2$  throughout the cell due to photolysis. The transmitted intensity likewise increases by no more than a few percent, and some of this increase is due to a systemic drift, as explained earlier. It is thus apparent that no large change in  $\text{Br}_2$  concentration occurs.

Although no large excursions in  $\text{Br}_2$  pressure were observed, the role of recombination in the decay process was still in question. While establishment of an initial equilibrium between photolysis and diffusion/recombination processes is effectively instantaneous on the time-scale of Figure 4-14, the subsequent rise in pressure depicted indicates a gradual shift in the equilibrium point toward some long-term limiting value. This secondary equilibrium process may be due to a slow decrease in the wall recombination rate, possibly related to the displacement of some fraction of the adsorbed  $\text{Br}_2$  molecules by Br atoms. In addition to the pressure rise, the association of some other long-term effect with recombination dynamics seems feasible.

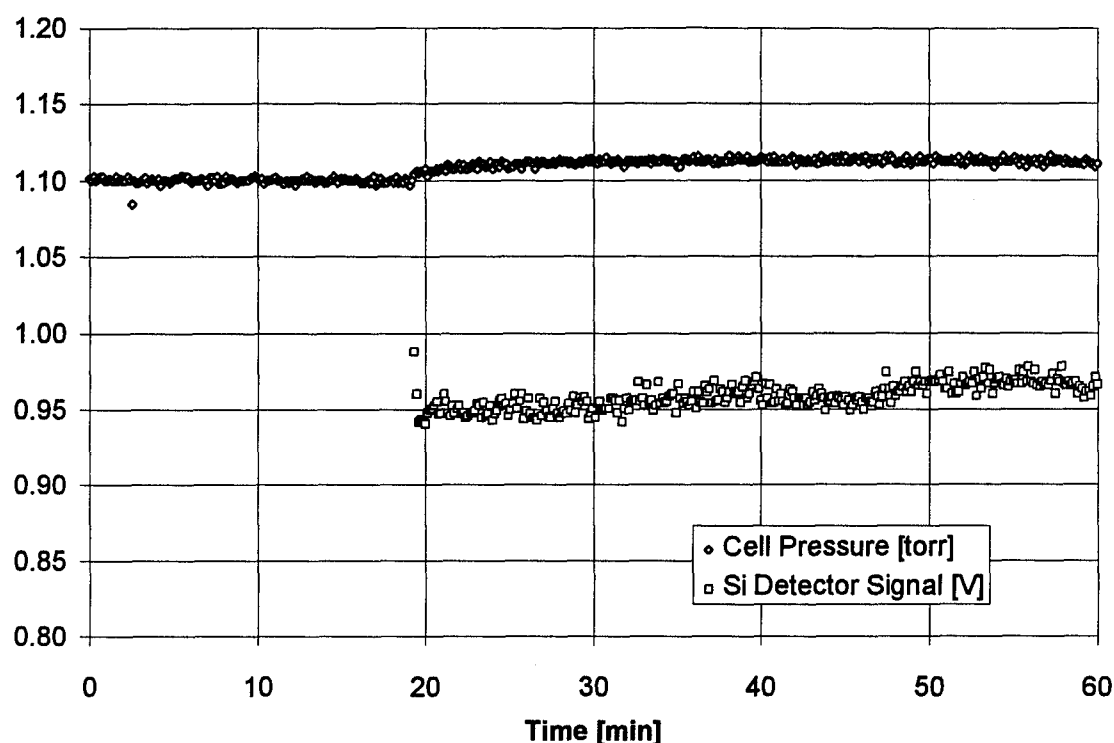


Figure 4-14. Total cell pressure and Si detector signal vs. time. Note that transmitted intensity is reported, rather than the  $I_t/I_i$  ratio. Modulation in the transmitted intensity is due to laser power fluctuation.

If signal decay were related to photolysis or recombination in some way (other than simply the steady depletion of  $\text{Br}_2$ , which has apparently been ruled out), it could conceivably be halted or reversed by the cessation of photolysis. This idea was tested by blocking and unblocking the laser during the course of several data runs, with the typical outcome presented below in Figure 4-15. This data shows that signal decay occurs only during periods of photolysis, consistent with the results of Figure 4-13 above. Significantly, no recovery of signal intensity is seen after a twenty-minute break; however, Figure 4-15 also shows that cell pressure eventually returns to its original level in the absence of photolysis, as recombination continues. These findings indicate that recombination, while apparently a slow process, is not a factor in the decay of the  $4.3\text{ }\mu\text{m}$  emission.

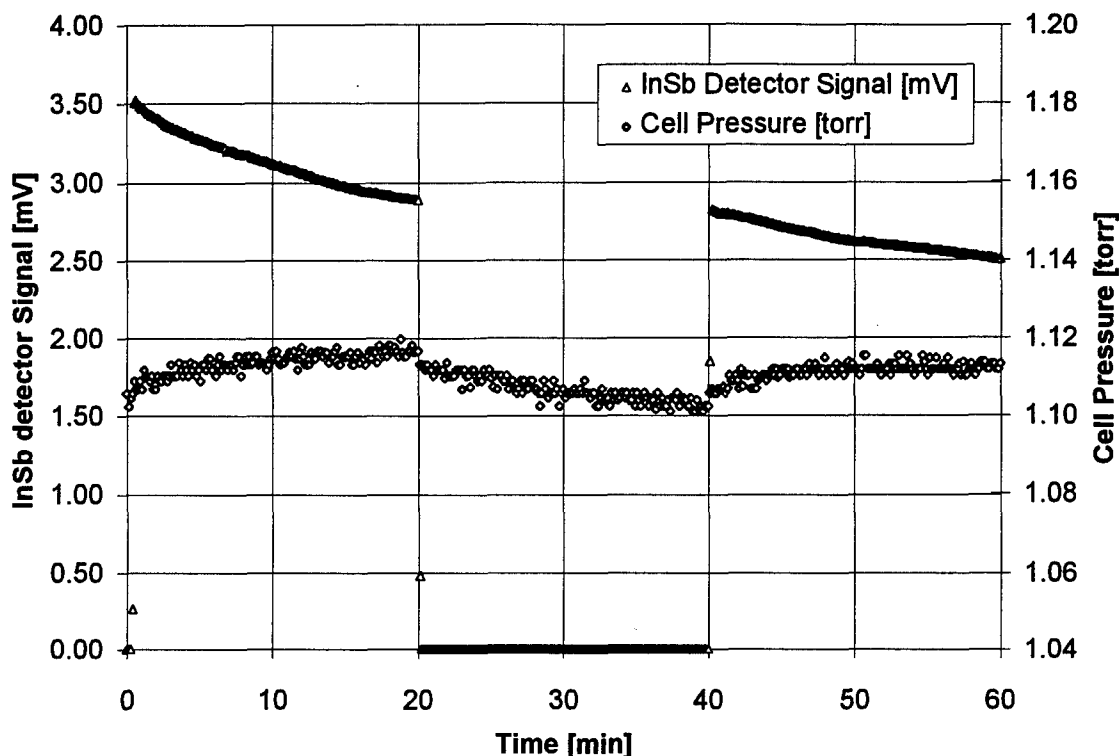


Figure 4-15. 4.3  $\mu\text{m}$  signal and cell pressure vs. time. Note that cell pressure returns to its starting value in the absence of photolysis, whereas emission intensity is not restored.

#### 4. $\text{Br}^*$ Quenching

The next possible decay mechanism examined was quenching of  $\text{Br}^*$ . The preceding experiments showed that signal decay is related in some way to photolysis. If photolysis leads to the irreversible production of some species which quenches  $\text{Br}^*$ , a steady decay in both  $\text{Br}^*$  and  $\text{CO}_2^+$  emissions would result. This unknown quenching species could come from a reaction or combination of reactions involving  $\text{Br}_2$ ,  $\text{Br}$ ,  $\text{CO}_2$ , or some contaminant in the system, but its production could not lead to a significant net change in system pressure, as none was detected. To test for quenching of  $\text{Br}^*$ , the 2.71  $\mu\text{m}$  emission was monitored for both 1000 mtorr of pure  $\text{Br}_2$  and a standard 1000/100  $\text{Br}_2/\text{CO}_2$  mix. While the  $\text{Br}^*$  emission was reduced with the addition of  $\text{CO}_2$  as expected,

no time-decay in the emission intensity was observed in either case, eliminating  $\text{Br}^*$  quenching as a decay mechanism. Results of these trials are shown in Figure 4-16.

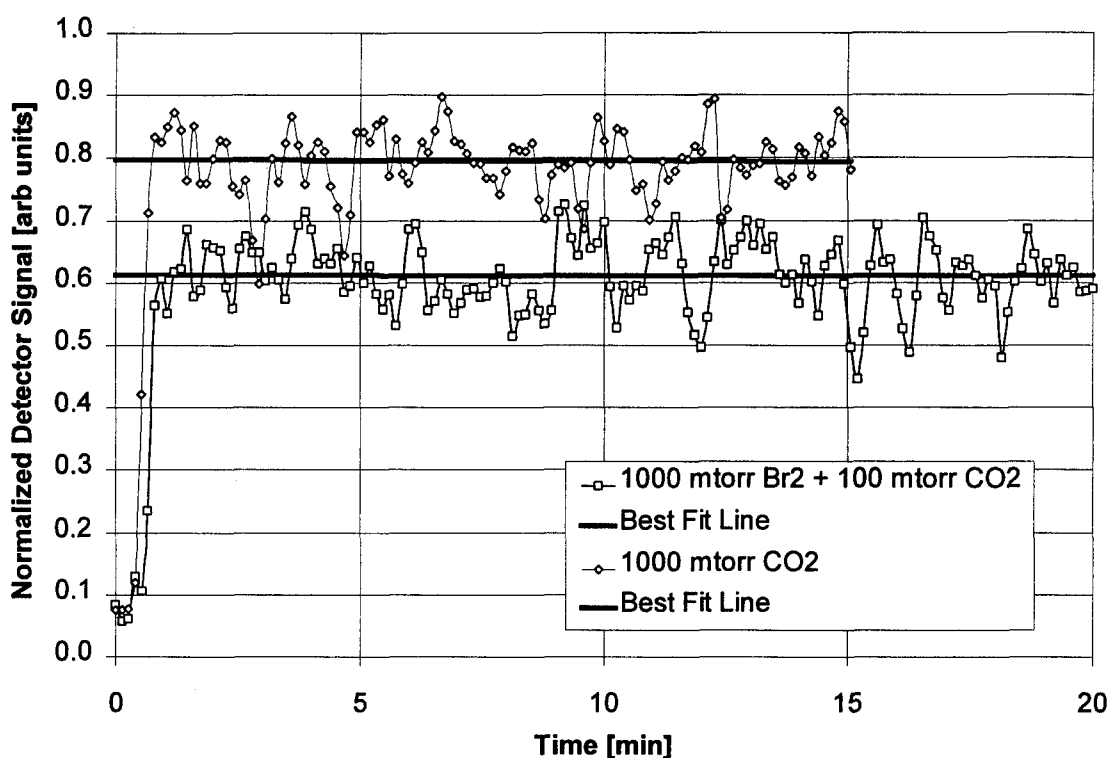


Figure 4-16.  $2.71\ \mu\text{m}$  emission intensity vs. time for 1000 mtorr  $\text{Br}_2$  and 1000/100 mtorr  $\text{Br}_2/\text{CO}_2$  mix. Best-fit straight lines depicted are level to within standard error. Note the reduced signal due to quenching by  $\text{CO}_2$ .

### 5. $\text{CO}_2$ Loss

With  $\text{Br}_2$  and  $\text{Br}^*$  loss seemingly eliminated as candidate decay mechanisms, attention is now turned to  $\text{CO}_2$ . As Figure 4-6 shows, the peak  $\text{CO}_2^\dagger$  emission occurs for a mixture of approximately 100 mtorr  $\text{CO}_2$  with 1000 mtorr  $\text{Br}_2$ , the standard used in this work. Thus, a decrease in  $\text{CO}_2^\dagger$  emission could signify either an increase or a decrease in  $\text{CO}_2$  pressure, where such a change could occur for any of the reasons mentioned earlier for  $\text{Br}_2$  (save recombination). From Figure 4-6 it is clear that  $\text{CO}_2$  pressure would have to decrease by about 50 mtorr or increase by about 1.2 torr in order to effect a 50 %



reduction in emission intensity. In either case, this pressure change would be easily detectable, and is not observed. Further evidence that  $\text{CO}_2$  concentration is essentially constant is given in Figure 4-16, where no change is observed over time in the rate of  $\text{Br}^*$  quenching by  $\text{CO}_2$ .

#### 6. $\text{CO}_2^\dagger$ Quenching

It has been established up to this point that no significant change in  $\text{Br}_2$  concentration,  $\text{Br}^*$  production,  $\text{CO}_2$  concentration, or  $\text{CO}_2^\dagger$  production (via  $\text{Br}^*$  quenching) is observed. The only remaining mechanism for the time-decay of  $4.3\ \mu\text{m}$  emissions seems to be the quenching of  $\text{CO}_2^\dagger$  by some species other than  $\text{CO}_2$ . This unknown species would have to fit the description proposed earlier for a possible quencher of  $\text{Br}^*$ . Since no reaction is expected between  $\text{Br}_2$  and  $\text{CO}_2$  <sup>(21)</sup>, the most likely progenitor of such a species would be a contaminant in the system. It is hypothesized that this contaminant changes via an interaction with 488 nm light, and possibly one of the lasing gases, into a species which strongly quenches  $\text{CO}_2^\dagger$  but not  $\text{Br}^*$ . This reaction is not reversible under the conditions which normally obtain in the cell, necessitating a purge and refill after sustained photolysis to restore fluorescent emission intensity. While this scenario appears somewhat unlikely, it is the only one among those considered which fits current observations. Due to time limitations, no further attempt was made to isolate this suspected contaminant nor characterize its interaction with the  $\text{Br}_2/\text{CO}_2$  system.

#### E. Chopping Frequency Dependence

As the goal of this work was to collect data relative to the construction of a continuously-pumped (ie CW) photolytic laser device, it was desired to know how side-fluorescence observations might differ under modulated pumping, as employed throughout this research. This understanding is necessary if results are to be related to the CW case. To this end, a simple experiment was conducted to measure emission intensity

as a function of chopping frequency. The results of this test were surprising, and may have bearing on the construction of a CW device. Two possible explanations for the results are considered, but due to time constraints verification via detailed modeling or further experimentation was not attempted.

Due to the very short time scales for quenching of  $\text{Br}^*$  and  $\text{CO}_2^\dagger$ , equilibrium concentrations are expected to be reached within microseconds, assuming  $\text{Br}_2$  and  $\text{CO}_2(000)$  concentrations remain essentially constant. Thus a chopping rate of 200 Hz, with a half-period of 2.5 milliseconds, should be equivalent to continuous pumping as far as these kinetic processes are concerned. That is, the only effect of chopping at relatively low frequencies should be to reduce the average fluorescent intensity by 50 %, corresponding to the 50 % duty cycle of the chopped pump beam. Varying the chopping frequency up to several thousand hertz should have no effect on the fluorescence, since equilibrium should still be achieved during each pumping cycle. As Figure 4-17 shows, the experimental results differed considerably from this expectation. A pronounced dependence on chopping frequency was seen for the  $4.3 \mu\text{m}$  side fluorescence, such that an increase in chopping rate from 20 Hz to 3000 Hz caused nearly a ten-fold reduction in signal strength. Figure 4-18 shows the flat frequency response of the detector/preamp/lock-in amp combination with a white light source, indicating that the signal attenuation observed in Figure 4-17 is not due to detector response.

Possible explanations for this effect begin with discarding the earlier assumption that  $\text{Br}_2$  and  $\text{CO}_2(000)$  concentrations remain more or less constant. Within the volume of the pump laser beam,  $\text{Br}_2$  is depleted by photolysis and replenished either by three-body recombination or diffusion from the surrounding *reservoir* constituted by the remaining cell volume (which is itself ultimately replenished by wall recombination). Since photolysis and diffusion/recombination are slower than quenching, equilibrium

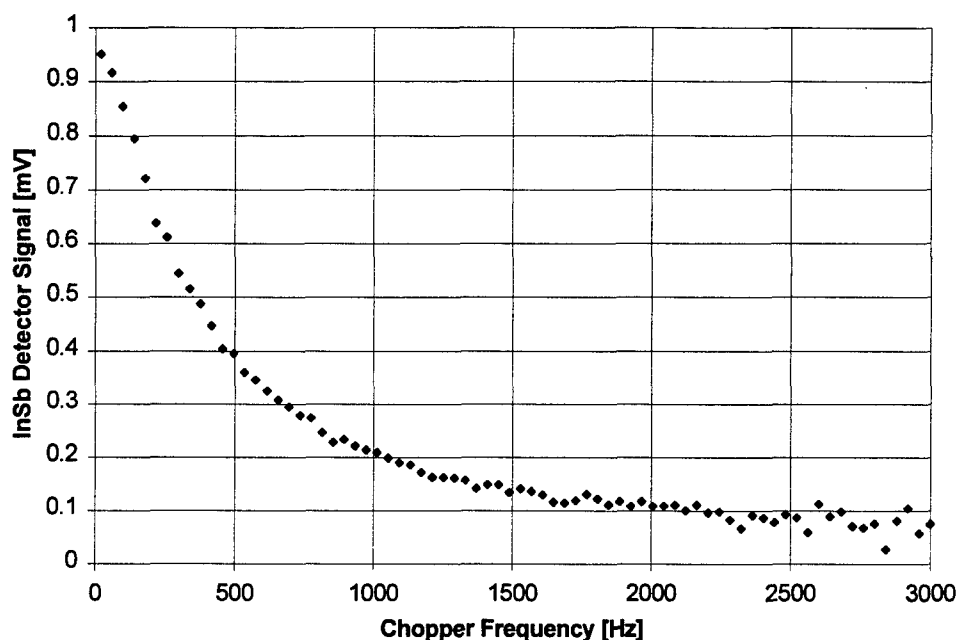


Figure 4-17. 4.3  $\mu\text{m}$  signal vs. chopping frequency for standard 1000/100 mtorr  $\text{Br}_2/\text{CO}_2$  mixture.

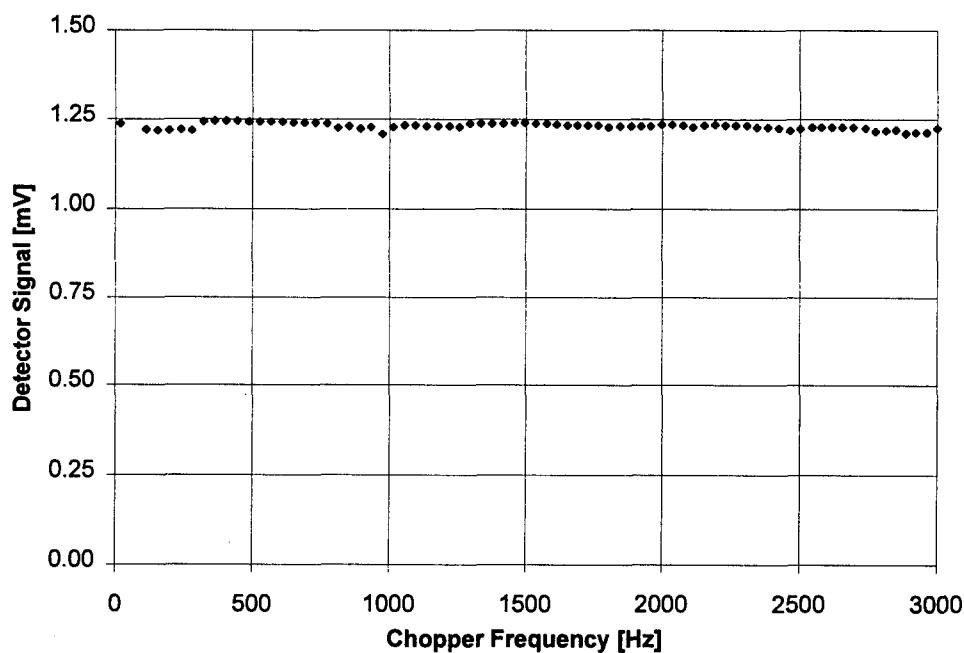


Figure 4-18. Detector signal vs. chopping frequency with 4.3  $\mu\text{m}$  filter and white light source. The slight decay in the signal is due to battery drainage in the source over the 5 min run. The same decay was seen in a run starting at 3000 Hz and decelerating to 20 Hz.

between these processes may not be achieved during the chopping cycle, even at relatively low frequencies. Without speculating on the actual mechanism, it is suggested that increasing the chopping frequency results in a lower average concentration of  $\text{Br}_2$  within the pump region, thus decreasing the production of  $\text{Br}^*$ . This hypothesis could be tested by observing  $2.71\text{ }\mu\text{m}$  emission intensity as a function of chopping frequency, an experiment not performed in this work.

Another possibility is that  $\text{CO}_2(000)$  is being depleted within the pump beam region. It has been shown that ground state  $\text{CO}_2$  rapidly quenches both  $\text{Br}^*$  and  $\text{CO}_2^\dagger$ , ultimately resulting in the production of  $\text{CO}_2(100)$  and  $\text{CO}_2(001)$ , among other vibrationally excited states. If these lower vibrational states are not rapidly quenched, they may contribute to a *bottlenecking* effect within the pump region (for example,  $\text{CO}_2(001)$  has a radiative lifetime of 5.6 sec).<sup>(11)</sup> If this is the case, increasing the chopping frequency may exacerbate the effect by reducing the *recovery* time between pump cycles. Again, no precise mechanism for such a relationship is offered.

## *V. Conclusions and Recommendations*

### *A. 488 nm Absorption*

The result obtained for the absorption cross section of  $\text{Br}_2$  at 488 nm was accurate, agreeing with the previously reported value to within experimental error. This suggests Beer's Law could in principle have been employed to provide an accurate  $\text{Br}_2$  concentration metric, although this attempt was unsuccessful in practice due to apparent equipment limitations. Transmitted laser intensity was used in previous AFIT work <sup>(28)</sup> to measure  $\sigma_{488}$ , but not to measure  $\text{Br}_2$  concentration. Because the  $\text{Ar}^+$  laser used did not have an intensity control (it had only a current control), its power output may not have been stable enough for the transmittance measurement. While using the normalized intensity  $I_t/I_i$  was supposed to compensate for laser output drift, this apparently didn't work. It is suspected that slight nonlinearity in the response of the Si detectors caused the measured intensity ratio to drift with laser power fluctuations.

If 488 nm transmittance is to be used to monitor  $[\text{Br}_2]$  in future work, it is recommended that a laser with an intensity control (ie an output feedback loop) be employed. Further, both Si detectors should have the same neutral density filters installed (an option not available in this experiment), and these should be selected to ensure linear response. Finally, the Si detectors should each measure scatter from the same type of surface, which could be achieved by placing the chopper before the first turning prism and aiming the detectors at the prism faces (see Figure 3-1).

If adequate stability cannot be achieved via these modifications, another alternative is to use a white light source as employed by Johnson. Using a high intensity halogen lamp and 409 nm filters, Johnson reported a  $[\text{Br}_2]$  measurement sensitivity of 3 mtorr with his dedicated absorption diagnostic system. <sup>(11)</sup>

### *B. CO<sub>2</sub> Quenching of Br\**

The most significant finding of this experiment was the validation of the form of Equation (2-24) for the steady-state Br\* concentration as a function of CO<sub>2</sub> pressure. This result, also demonstrated in previous AFIT work <sup>(11, 28)</sup>, indicates that the underlying Br\* production and loss processes have been adequately described, and helps narrow down the search for the unknown mechanisms affecting steady-state CO<sub>2</sub><sup>†</sup> concentration, as discussed in the next section.

The measurement of a fairly rapid collision-free quenching rate ( $k_0$ ) was also significant in that it illustrated the dependence of certain kinetic processes on device construction. The fact that the  $k_0$  measured for this apparatus was an order of magnitude larger than that reported in earlier work <sup>(11)</sup> is reasonable considering the differences in cell geometry and the form of Equation (2-15).

The precision of the  $k_0$  value obtained by fitting Equation (4-4) to the experimental data was limited by the low SNR of the 2.71  $\mu\text{m}$  signal. The SNR, and thus the fit, could be improved somewhat by using a lens system to collect and focus the fluorescent emissions onto the detector element, a technique employed successfully in previous AFIT work. <sup>(11, 14, 28)</sup> A higher SNR would also facilitate use of the linear fit technique described by Equation (2-25), which might further enhance precision. The  $k_0$  value could be refined by taking measurements over the course of several days, as Johnson did, which would also provide a measure of the stability of the system.

### *C. CO<sub>2</sub> Quenching of CO<sub>2</sub><sup>†</sup>*

The data collected in this experiment defined curves of the same shape described by Tate in his Br\*-CO<sub>2</sub> quenching experiment, confirming Johnson's explanation of Tate's results, ie that Tate had observed CO<sub>2</sub><sup>†</sup> rather than Br\* emissions. <sup>(11, 28)</sup> This fact explains why Tate's attempt to model his results was unsuccessful. Even with this knowledge, however, it was still not possible to successfully model the experimental

results, leading to the conclusion that additional  $\text{CO}_2^+$  production channels (other than  $\text{E} \rightarrow \text{V}$  transfer from  $\text{Br}^*$ ) must be sought. This conclusion is based in part on the recognition that the  $\text{Br}^*$  production/loss processes have been adequately identified, as pointed out in the previous section, leaving  $\text{CO}_2^+$  production processes as the likely source of the discrepancy. Further evidence that modifications to the kinetic model for  $\text{CO}_2^+$  production are needed exists in the difficulty encountered by Perram and Johnson in modeling the output pulse shapes seen in Johnson's  $\text{CO}_2$  laser as a function of  $\text{CO}_2$  pressure. (13, 19)

A related finding of this study was that the concentration of  $\text{CO}_2^+$  in the system apparently depends on the *ratio* of  $\text{CO}_2$  and  $\text{Br}_2$  pressures, rather than simply the  $\text{CO}_2$  pressure alone. While this result is intuitively satisfying, it had not been explicitly recognized by previous workers. Pastel et al and Johnson each reported 4.3  $\mu\text{m}$  laser pulse energy as a function of  $\text{CO}_2$  pressure, noting that output decreased due to  $\text{V} \rightarrow \text{V}$  relaxation above a certain pressure. The steady-state data from the present work suggest an optimum  $\text{Br}_2:\text{CO}_2$  ratio of approximately 10:1, determined by the emission peaks in Figure 4-7. This finding is consistent with the laser operating range of 1:1-20:1 ratios reported by Pastel (corresponding approximately to the half-maximum points in Figure 4-7), and the maximum pulse energy at a 6:1 ratio reported by Johnson. (11, 18) This consistency also indicates that, lacking a complete theoretical model, the empirical data from steady-state experiments may be useful for predicting laser device performance.

The revised kinetic model of Equations (4-7) to (4-10) represents only a hypothetical example, and a demonstration of a possible approach to improving the current model. Before a new  $[\text{CO}_2^+]$  model may be formulated, a detailed search of the literature for likely  $\text{V} \rightarrow \text{V}$  (or other) production channels, reaction rates, and state lifetimes must be accomplished. Due to the number of previous studies of  $\text{E} \rightarrow \text{V}$  transfer kinetics and  $\text{CO}_2$  lasers, sufficient information may already exist to construct a model

which completely describes the current experimental results. If this is not the case, further experiments, such as using different IR bandpass filters to monitor the steady-state populations of other CO<sub>2</sub> vibrational levels, may be necessary.

Another possibility is that the steady flow of CO<sub>2</sub> employed in this experiment, coupled with the slight mixing delay depicted in Figure 4-11, acts to distort the shape of the [CO<sub>2</sub><sup>†</sup>] vs. [CO<sub>2</sub>] graph. If this is so, collecting data for several discrete CO<sub>2</sub> pressures, particularly in the region of the emission peak, may lead to a curve shape that yields more readily to mathematical modeling. In any case, the non-zero limiting behavior for higher CO<sub>2</sub> pressures will have to be accounted for in any revised model.

#### *D. Steady-State Signal Decay*

Despite several attempts, the source of the steady-state signal decay could not be conclusively isolated. Several explanations were apparently ruled out, including mixing, loss of Br<sub>2</sub>, quenching of Br\*, and loss of CO<sub>2</sub>. This leaves only loss of CO<sub>2</sub><sup>†</sup>, due either to increased quenching or decreased production over time. While the precise mechanism is not known, this effect seems to depend on photolysis, and may involve a reaction with some contaminant to produce a CO<sub>2</sub><sup>†</sup>-quenching species, while maintaining total cell pressure. As noted in Chapter I, Peterson, Wittig, and Leone reported a similar decay in the output power of their laser apparatus with continued use of a single gas fill, attributing this to the leakage of Br\*-quenching contaminants into the system. <sup>(21)</sup> However, this explanation is not consistent with the current observation that the Br\* signal suffers no temporal decay. While Peterson et al concluded that the recombination of Br<sub>2</sub> and nonreactive nature of CO<sub>2</sub> should allow for closed-cell operation, the implication of the current findings is that, unless some avoidable contaminant is identified, a gas flow, or at least regular cell replenishment, may be necessary for sustained operation. It should be



noted that even if a gas flow is required, it would be at nothing near the rate employed in chemical lasers, based on the slow rate of signal decay observed.

Because of its possible implications for the fielding of practical  $E \rightarrow V$  laser devices, further efforts to explain and ultimately control the signal decay are recommended. To begin with, a significant potential source of contaminants may be eliminated by following the bromine sample purification procedure described by Johnson. <sup>(11)</sup> This process, incorporating several additional steps beyond those outlined in Chapter III, leads to a more complete removal of  $CO_2$ ,  $H_2O$ , and other atmospheric constituents from the  $Br_2$ . Next, all components of the apparatus should be thoroughly cleaned before assembly, and the system should be routinely and thoroughly purged before use (ie every night). This will necessitate the reseasoning of the cell before each day's work, but will avoid the problem of a steady buildup of adsorbed contaminants over time.

In addition to the above procedures, several experiments are suggested to further characterize and/or isolate the decay mechanism. Monitoring the decay rate as a function of pump laser power will help clarify the connection between photolysis and decay. Studying the effects of adding  $CO_2$  after some period of photolysis will indicate whether signal decay occurs in the absence of  $CO_2$ , and whether adding  $CO_2$  to the system will restore lost signal. Finally, using a mass spectrometer to directly identify the reaction cell constituents before and after photolysis will determine whether significant levels of contaminants are present, and whether photolysis-initiated chemical changes take place.

#### *E. Chopping Frequency Dependence*

The dependence of emission intensity on pump source chopping frequency was not expected, based on *back-of-the-envelope*-style estimates of the time to steady-state equilibrium between production and quenching processes. However, this effect, which

was also noted (but not published) by Johnson <sup>(13)</sup>, clearly does occur, and is in fact quite dramatic. Since the time-scale for quenching processes is much shorter than the period for even a 3000 Hz chopping rate, other, slower processes such as diffusion and recombination must be involved, and these processes may be still slower than previously believed. What is evident is that the equilibrium concentration of  $\text{CO}_2^+$  is dependent on the chopping rate of the photolysis source. How this might impact the construction of a CW laser is not clear, since it is not known whether the limit of very slow or very fast chopping rates is most analogous to CW operation. In either case, this finding indicates a difference in the response of chopped and unchopped systems is expected, and this difference must be characterized in greater detail if the performance of one system is to be related to the performance of the other.

Further experiments are suggested to address the preceding concerns. To begin with, as mentioned in Chapter IV, the 2.71  $\mu\text{m}$  emission should be monitored as a function of chopping frequency to determine whether a reduction in  $\text{Br}^*$  concentration is at the root of the observed  $\text{CO}_2^+$  signal attenuation. Monitoring the 488 nm transmittance would also indicate whether the  $\text{Br}_2$  concentration in the pump region (and thus  $\text{Br}^*$  production) depends on chopping frequency, which might imply a diffusion/recombination-related effect. If the signal attenuation is related to diffusion, adding a buffer gas to slow the diffusion rate should exaggerate this effect.

Time-resolved fluorescence techniques could be employed to directly observe the rise and decay of fluorescent intensity during the chopping cycle. This would show whether the signal attenuation is driven by the system's behavior during the laser on-time, off-time, or both, which would help answer the question of whether faster or slower chopping rates are most like continuous pumping. IR bandpass filters could be used to monitor the populations of different vibrational levels of  $\text{CO}_2$ , indicating whether a shift in these populations with chopping frequency contributes to bottlenecking at some level,

as considered in Chapter IV. Depending on the relationship between chopped and continuous pumping, this could imply that CW lasing is not possible, or might only be possible with a slowly chopped pump source.

Finally, an attempt should be made to model the attenuation effect based on currently understood kinetics. If  $\text{Br}^*$  loss is found by experiment to be the source of the attenuation, construction of an analytic or numerical model should be possible by taking into account known production, quenching, axial diffusion, and recombination processes. If  $\text{CO}_2^+$  loss is the source of the effect, construction of such a model may depend on (or assist) the identification of suspected  $\text{V} \rightarrow \text{V}$  production channels.

#### *F. Other Recommendations*

As indicated in the preceding discussion, the question of how the chopped system compares to a continuously-pumped system is central to extending the findings of this work to the development of practical laser devices. It would therefore be beneficial to repeat some of the experiments under continuous photolysis, chopping only the side-fluorescence signal. This would require modification of the apparatus and greater awareness of background noise sources, as explained in Chapter III, but would have the advantage of most accurately representing a CW laser system. Some of the questions raised above, such as the chopping frequency limit which approximates CW operation, and the steady-state populations of various  $\text{CO}_2$  vibrational levels, could thus be directly addressed.

The remaining obvious question, which can only be definitively answered by direct experimentation, is "will it lase?" As mentioned earlier, time constraints did not allow reconfiguring the apparatus and proceeding with this line of investigation. It is therefore recommended that attempts to observe CW lasing, testing the effects of various gas mixtures, total cell pressures, and continuous/chopped pump source, be undertaken.

It is also suggested that a simple modification may improve the efficiency of the laser apparatus. Since only the region of overlap between the lasing axis (defined by the cavity mirrors) and the pump beam acts as a gain medium, the gas cell does not need to be much longer than this region. Any additional length through which the pump beam must travel only serves to attenuate the beam, due to absorption by molecular bromine. If the extent of the overlap region is calculated, and the gas cell shortened accordingly, this will allow the use of higher bromine and carbon dioxide pressures (since it is the ratio between the two which determines the steady-state  $\text{CO}_2^+$  population) without undue absorption losses, increasing the power and efficiency of the device.

#### *G. Summary*

Several kinetic effects which may be relevant to the construction of E→V lasers, and in particular CW devices, have been investigated in this research. The non-collisional deactivation rate,  $k_0$ , is device-dependent, and may represent a significant counter-productive loss rate of electronically excited bromine. For maximum operating efficiency, the geometry of a laser device should be chosen so as to minimize this term as much as is practicable. A better kinetic model for the steady-state concentration of  $\text{CO}_2(101)$  is needed, since suspected unknown production channels for this vibrational state will surely affect the performance of both pulsed and CW laser devices. Lacking a theoretical model, empirical studies of  $[\text{CO}_2^+]$  pressure-dependence may be useful (or ultimately best) for finding the optimum parameters for CW operation. The steady-state decay of 4.3  $\mu\text{m}$  signal observed under photolysis may prohibit the use of sealed-off gas cells in  $\text{Br}_2$ - $\text{CO}_2$  E→V laser systems, if it is determined that this decay is an inherent rather than inadvertent limitation. The chopping frequency dependence of fluorescent emissions may indicate  $\text{Br}_2$  recombination and diffusion processes are slower than

previously thought, possibly limiting the cell pressures and/or pump rates which can be employed in bromine-based  $E \rightarrow V$  laser systems.

Further experiments have been proposed, many of which were planned but not executed due to time limitations, and some of which occurred purely as afterthoughts in the process of analyzing results. Most-notably, the discrete-pressure  $\text{CO}_2^+$  quenching, mass spectrometry,  $\text{Br}^*$  emission versus chopping frequency, and time-resolved fluorescence studies hold promise for a wealth of interesting future results. The potentially most exciting experiment, demonstrating a CW  $E \rightarrow V$  laser, will be attempted in the near future. Whether or not this attempt is successful, the results of this experiment will undoubtedly pave the way for still more rewarding follow-on work.

### Bibliography

1. Anderson, Elmer E. *Modern Physics and Quantum Mechanics*. Philadelphia: W.B. Saunders Company, 1971.
2. Banwell, C. N. *Fundamentals of Molecular Spectroscopy (2nd ed)*. London: McGRAW-HILL Book Company (UK) Limited, 1972.
3. Boriev, I. A. and others. "Determination of the Emission Cross Section for the  $^2P_{1/2} - ^2P_{3/2}$  Transition of the Bromine Atom," *Optical Spectroscopy (USSR)*, 54: 233-237 (March 1983).
4. Donovan, R. J. and D. Husain. "Chemistry of Electronically Excited Atoms," *Chemical Reviews*, 70: 509-516 (1970).
5. *Excel*. Version 5.0a, MS-DOS/Windows, disk. Computer software. Microsoft Corporation, Redmond WA, 1985-1993.
6. Finzi, J. and Bradley Moore. "Relaxation of  $CO_2(10^01)$ ,  $CO_2(02^01)$ , and  $N_2O(10^01)$  vibrational levels by near-resonant  $V \rightarrow V$  energy transfer," *Journal of Chemical Physics*, 63: 2285-2288 (September 1975).
7. Hariri, A.B., Peterson and Wittig. "Electronic-Vibrational Energy Transfer from  $Br(4^2P_{1/2})$  to HCN, and Deactivation of  $HCN(001)^*$ ," *Journal of Chemical Physics*, 65: 1872-1875 (September, 1976).
8. Hariri, A.B. and C. Wittig. "Electronic to Vibrational Energy Transfer from  $Br(4^2P_{1/2})$  to  $CO_2$ , COS, and  $CS_2$ ," *Journal of Chemical Physics*, 67: 4454-4462 (November 1977).
9. Haugen, H. K., E. Weitz, and S. R. Leone. "Accurate Quantum Yields by Laser Gain versus Absorption Spectroscopy: Investigation of  $Br/Br^*$  Channels in Photofragmentation of  $Br_2$  and  $IBr$ ," *Journal of Chemical Physics*, 83: 3402-3412 (October 1985).
10. *IR Spectroscopy Tutor and Reference*. Version 1.0, MS-DOS/Windows, disk. Computer Software. Perkin-Elmer Corporation, 1992-1993.
11. Johnson, Ray O. *Excited Atomic Bromine Energy Transfer and Quenching Mechanisms*. PhD Dissertation, AFIT/DS/ENP/93-05. School of Engineering, Air Force Institute of Technology (AU), Wright-Patterson AFB OH, August 1993.

12. Johnson, Ray O. and others. "Atomic Bromine-Nitric Oxide Electronic-to-Vibrational Energy Transfer Laser," *Proceedings of the International Conference on LASERS '93*, STS Press, McLean VA, 1994.
13. Johnson, Ray O. Research Scientist, Wright Laboratories (AFMC), Wright-Patterson AFB OH. Personal Interviews. July-September 1995.
14. Katapski, Steven M. *Electronic-To-Vibrational ( $E \rightarrow V$ ) Energy Transfer From  $Br^*$  to  $CO_2$  & ( $E \rightarrow V$ ) Laser Feasibility Studies*. Masters Thesis, AFIT/GEP/ENP/92D-07. School of Engineering, Air Force Institute of Technology (AU), Wright-Patterson AFB OH, October 1992.
15. Leone, S. R. and F. J. Wodarczyk. "Laser-Excited Electronic-to-Vibrational Energy Transfer from  $Br(4^2P_{1/2})$  to HCl and HBr," *Journal of Chemical Physics*, 60: 314 (January 1974).
16. Mulliken, R. S. "The Interpretation of Band Spectra, Part III," *Reviews of Modern Physics*, 4: 1-88 (January 1932).
17. Okabe, H. *Photochemistry of Small Molecules*. New York: John Wiley and Sons, 1978.
18. Pastel, Robert L. and others. "Efficient  $Br^*$  Laser Pumped by Frequency-Doubled Nd:YAG and Electronic-to-Vibrational Transfer Pumped  $CO_2$  and HCN Lasers," *Chemical Physics Letters*, 183: 565-569 (September 1991).
19. Perram, Glenn P. Professor, Air Force Institute of Technology (AU), Wright-Patterson AFB OH. Notes and personal interviews. January-September 1995.
20. Petersen, Alan B., Curt Wittig, and Stephen R. Leone. "Infrared Molecular Lasers Pumped by Electronic-Vibrational Energy Transfer from  $Br(4^2P_{1/2})$ :  $CO_2$ ,  $N_2O$ , HCN, and  $C_2H_2$ ," *Applied Physics Letters*, 27: 305-306 (September 1975).
21. Petersen, Alan B., Curt Wittig, and Stephen R. Leone. "Electronic-to-Vibrational Pumped  $CO_2$  Laser Operating at 4.3, 10.6, and 17.1  $\mu m$ ," *Journal of Applied Physics*, 47: 1051-1054 (March 1976).
22. Sedlacek, A. J., R. E. Weston, and G. W. Flynn. " $Br^*$  and  $CO_2$  revisited: An investigation of E-V energy transfer with time-resolved diode laser spectroscopy," *Journal of Chemical Physics*, 93: 2816-2818 (August 1990).
23. Seery, D. J. and D. Britton. "The Continuous Absorption Spectra of Chlorine, Bromine, Bromine Chloride, Iodine Chloride, and Iodine Bromide," *Journal of Physical Chemistry*, 68: 2263-2266 (August 1964).

24. Struve, Walter S. *Fundamentals of Molecular Spectroscopy*. New York: John Wiley and Sons, 1989.
25. Summers, Donald B. *Chemistry Handbook (2nd ed)*. Boston: Willard Grant Press, 1975.
26. Svanberg, Sune. *Atomic and Molecular Spectroscopy*. Berlin: Springer-Verlag, 1991.
27. *TableCurve2D*. Version 3.0 (32-bit), MS-DOS/Windows, disk. Computer Software. Jandel Scientific, San Rafael CA, 1989-1995.
28. Tate, Ralph F. *Steady-State Production and Quenching of Br( $^2P_{1/2}$ )*. MS Thesis, AFIT/GE/ENP/91D-01. School of Engineering, Air Force Institute of Technology (AU), Wright-Patterson AFB OH, October 1991.
29. Verdeyen, Joseph T. *Laser Electronics (3rd ed)*. New Jersey: Prentice-Hall, Inc., 1991.
30. Wodarczyk, F. J. and P. B. Sackett. "Electronic-to-Vibrational Energy Transfer from Br( $4^2P_{1/2}$ ) to HF," *Chemical Physics*, 12: 65-70 (1976).



Vita

Captain Stephen J. Karis [REDACTED] [REDACTED]

[REDACTED]. He grew up in San Francisco, CA, where he attended J. Eugene McAteer and Lick-Wilmerding High Schools. In July 1985, he received an Associate in Science in Electrical Engineering from City College of San Francisco, where he was class valedictorian. He graduated from San Francisco State University in May 1988 with a Bachelor of Arts in Astrophysics, Magna Cum Laude, and as an AFROTC Distinguished Graduate. He was awarded a (delayed) regular Air Force commission in June 1988, and worked as a software analyst for WordTech Systems in Orinda, CA until entering active duty in April 1989. He then attended Euro-Nato Joint Jet Pilot Training (ENJJPT) at Sheppard AFB, TX, followed by Lead-In Fighter Training (LIFT) at Holloman AFB, NM, and F-16 Replacement Training Unit (RTU) at MacDill AFB, FL. His first operational assignment was to Misawa AB, Japan from November 1991 to April 1994, where he served as a fighter pilot with the 14th Fighter Squadron (Fightin' Samurai), and Wing Life Support Officer with the 432nd Operations Support Squadron. He accepted an assignment to the Graduate Applied Physics program, School of Engineering, Air Force Institute of Technology in May 1994, with a follow-on assignment to Phillips Laboratory, Kirtland AFB, NM in January 1996.

[REDACTED] [REDACTED] way  
[REDACTED] [REDACTED]

REPORT DOCUMENTATION PAGE			Form Approved OMB No. 0704-0188	
Public reporting burden for this collection of information is estimated to average 1 hour per response, including the time for reviewing instructions, searching existing data sources, gathering and maintaining the data needed, and completing and reviewing the collection of information. Send comments regarding this burden estimate or any other aspect of this collection of information, including suggestions for reducing this burden, to Washington Headquarters Services, Directorate for Information Operations and Reports, 1215 Jefferson Davis Highway, Suite 1204, Arlington, VA 22202-4302, and to the Office of Management and Budget, Paperwork Reduction Project (0704-0188), Washington, DC 20503.				
1. AGENCY USE ONLY (Leave blank)		2. REPORT DATE 27 November 1995		3. REPORT TYPE AND DATES COVERED Masters Thesis
4. TITLE AND SUBTITLE Steady-State Kinetics of $\text{Br}(^2\text{P}_{1/2}) \rightarrow \text{CO}_2(101)$ Electronic-to-Vibrational Energy Transfer Laser System			5. FUNDING NUMBERS	
6. AUTHOR(S) Captain Stephen J. Karis				
7. PERFORMING ORGANIZATION NAME(S) AND ADDRESS(ES) AFIT/ENP 2950 P Street Wright-Patterson AFB, OH 45433-7765 Advisor: Major Glen Perram			8. PERFORMING ORGANIZATION REPORT NUMBER AFIT/GAP/ENP/95-11	
9. SPONSORING / MONITORING AGENCY NAME(S) AND ADDRESS(ES) PL/LID 3550 Aberdeen Ave SE Kirtland AFB, NM 87117-6008 POC: E. A. Dorko and G. D. Hager			10. SPONSORING / MONITORING AGENCY REPORT NUMBER	
11. SUPPLEMENTARY NOTES				
12a. DISTRIBUTION / AVAILABILITY STATEMENT  Approved for public release; distribution unlimited			12b. DISTRIBUTION CODE	
13. ABSTRACT (Maximum 200 words)  Steady-state photolysis experiments were conducted to gain information relevant to the construction of a continuous-wave electronic-to-vibrational pumped infrared laser. An $\text{Ar}^+$ laser ( $\lambda = 488 \text{ nm}$ ) was used to produce the electronically excited state $\text{Br}(^2\text{P}_{1/2})$ ( $\text{Br}^*$ ) via photolysis of molecular bromine. Energy was then transferred to the near-resonant vibrational state $\text{CO}_2(101)$ ( $\text{CO}_2^\dagger$ ) via the collisional quenching of $\text{Br}^*$ by $\text{CO}_2$ . The dependence of the $2.71 \mu\text{m}$ $\text{Br}^*$ and $4.3 \mu\text{m}$ $\text{CO}_2^\dagger$ emissions on $\text{CO}_2$ pressure was measured, as well as the dependence of the $4.3 \mu\text{m}$ emission on pump laser chopping frequency. Unexpected results were obtained in both cases, indicating more detailed modeling of kinetic processes is called for. Additionally, an unexplained long-term decay in the $4.3 \mu\text{m}$ signal was observed, which may have bearing on the construction of closed-system laser devices. Recommendations are made for further research.				
14. SUBJECT TERMS  photolysis of $\text{Br}_2$ , E-V transfer, gas laser kinetics, $\text{Br}^*:\text{CO}_2$ laser			15. NUMBER OF PAGES 105	
			16. PRICE CODE	
17. SECURITY CLASSIFICATION OF REPORT Unclassified	18. SECURITY CLASSIFICATION OF THIS PAGE Unclassified	19. SECURITY CLASSIFICATION OF ABSTRACT Unclassified	20. LIMITATION OF ABSTRACT UL	

## GENERAL INSTRUCTIONS FOR COMPLETING SF 298

The Report Documentation Page (RDP) is used in announcing and cataloging reports. It is important that this information be consistent with the rest of the report, particularly the cover and title page. Instructions for filling in each block of the form follow. It is important to *stay within the lines* to meet *optical scanning requirements*.

**Block 1. Agency Use Only (Leave blank).**

**Block 2. Report Date.** Full publication date including day, month, and year, if available (e.g. 1 Jan 88). Must cite at least the year.

**Block 3. Type of Report and Dates Covered.** State whether report is interim, final, etc. If applicable, enter inclusive report dates (e.g. 10 Jun 87 - 30 Jun 88).

**Block 4. Title and Subtitle.** A title is taken from the part of the report that provides the most meaningful and complete information. When a report is prepared in more than one volume, repeat the primary title, add volume number, and include subtitle for the specific volume. On classified documents enter the title classification in parentheses.

**Block 5. Funding Numbers.** To include contract and grant numbers; may include program element number(s), project number(s), task number(s), and work unit number(s). Use the following labels:

<b>C</b> - Contract	<b>PR</b> - Project
<b>G</b> - Grant	<b>TA</b> - Task
<b>PE</b> - Program Element	<b>WU</b> - Work Unit Accession No.

**Block 6. Author(s).** Name(s) of person(s) responsible for writing the report, performing the research, or credited with the content of the report. If editor or compiler, this should follow the name(s).

**Block 7. Performing Organization Name(s) and Address(es).** Self-explanatory.

**Block 8. Performing Organization Report Number.** Enter the unique alphanumeric report number(s) assigned by the organization performing the report.

**Block 9. Sponsoring/Monitoring Agency Name(s) and Address(es).** Self-explanatory.

**Block 10. Sponsoring/Monitoring Agency Report Number.** (If known)

**Block 11. Supplementary Notes.** Enter information not included elsewhere such as: Prepared in cooperation with...; Trans. of...; To be published in.... When a report is revised, include a statement whether the new report supersedes or supplements the older report.

**Block 12a. Distribution/Availability Statement.** Denotes public availability or limitations. Cite any availability to the public. Enter additional limitations or special markings in all capitals (e.g. NOFORN, REL, ITAR).

**DOD** - See DoDD 5230.24, "Distribution Statements on Technical Documents."

**DOE** - See authorities.

**NASA** - See Handbook NHB 2200.2.

**NTIS** - Leave blank.

**Block 12b. Distribution Code.**

**DOD** - Leave blank.

**DOE** - Enter DOE distribution categories from the Standard Distribution for Unclassified Scientific and Technical Reports.

**NASA** - Leave blank.

**NTIS** - Leave blank.

**Block 13. Abstract.** Include a brief (*Maximum 200 words*) factual summary of the most significant information contained in the report.

**Block 14. Subject Terms.** Keywords or phrases identifying major subjects in the report.

**Block 15. Number of Pages.** Enter the total number of pages.

**Block 16. Price Code.** Enter appropriate price code (*NTIS only*).

**Blocks 17. - 19. Security Classifications.** Self-explanatory. Enter U.S. Security Classification in accordance with U.S. Security Regulations (i.e., UNCLASSIFIED). If form contains classified information, stamp classification on the top and bottom of the page.

**Block 20. Limitation of Abstract.** This block must be completed to assign a limitation to the abstract. Enter either UL (unlimited) or SAR (same as report). An entry in this block is necessary if the abstract is to be limited. If blank, the abstract is assumed to be unlimited.